DOCTORAL THESIS

Laser-induced electron interferences from atoms and molecules

Author:
Aurelien SANCHEZ

Supervisor:
Pr. Dr. Jens BIEGERT

A thesis submitted in partial fulfillment of the requirements for the degree of Doctor of Philosophy

in the

UPC-Universitat Politecnica de Catalunya
ICFO-Institut de Ciences Fotoniques
Attoscience and Ultrafast Optics

June 2, 2022

Abstract

Since discovering wave-particle duality, science has changed our perception of light and matter, especially at the subatomic level. Thanks to such discoveries, we have been able to develop and expand our scientific knowledge over the past two centuries, crossing those limits. For instance, let us take the famous double-slit experiment from T. Young (1801). This experiment has been extended after the twentieth-century quantum revolution, revealing electron and neutron diffraction used nowadays to measure the nuclei separation from complex structures. Similarly, the experiment of Michelson and Morley (1887), which follows T. Young foundations, got a fair success in astronomy, enabling high-resolution imaging of stars in the universe. In this thesis, we use light to generate electrons and produce interferences similar to the double-slit experiment, which is analyzed further to study the atomic properties.

On the dynamics of an atom, that is, attoscience, we use ultrafast laser pulses to trigger motions on a femtoseconds time-scale. Together with the use of strong intense laser fields in the Mid-IR regime, the electron is ionized with zero-kinetic energy and subsequently accelerated by the laser ponderomotive energy.

Strong field dynamics offer rich structures that are encoded in the photoelectron momentum distribution. Since we use two-color combined laser fields, we can gate and control those dynamics further down on the sub-cycle scale. More precisely, we show that with the help of a Reaction Microscope, we can extract both electron information and nuclear dynamics within extraordinary sub-cycle temporal resolution.

Finally, the strong-field recollision model is investigated with molecules through the previously developed laser-induced electron diffraction (LIED) method. We show that backscattered electron interferences, issued from strong field at low impact parameters, embedded a particular molecular orientation that can be reproduced when the molecule is considered aligned with the laser field polarization. Those findings seem to encode a more profound property about wave diffraction in molecules until recently unexplored due to the imposed conditions given in conventional electron diffraction (CED).

Resumen

Desde que se descubrió la dualidad onda-partícula, la ciencia ha cambiado nuestra percepción de la luz y la materia, especialmente a nivel subatómico. Gracias a tales descubrimientos, hemos podido desarrollar y expandir nuestro conocimiento durante los últimos dos siglos, llegando ahora a estos infinitos límites de la ciencia. Por ejemplo, tomemos el famoso experimento de la doble rendija de T. Young (1801). Este experimento se ha ampliado después de la revolución cuántica del siglo XX, revelando la difracción de electrones y neutrones utilizada hoy en día para medir la separación de núcleos de estructuras complejas. De manera similar, el experimento de Michelson y Morley (1887), que sigue los fundamentos de T. Young, obtuvo un éxito considerable en astronomía, lo que permitió obtener imágenes de alta resolución de las estrellas del universo. En esta tesis, utilizamos la luz para generar electrones y producir interferencias de manera similar al experimento de doble rendija, que se analiza más a fondo para estudiar las propiedades atómicas.

En la dinámica de un átomo, es decir, la attociencia, utilizamos pulsos de láser ultrarrápidos para desencadenar movimientos en una escala de tiempo de femtosegundos. Junto con el uso de campos láser intensos y fuertes en el régimen Mid-IR, OPCPA, el electrón se ioniza con energía cinética cero y, posteriormente, se acelera con la energía ponderomotriz del láser.

La dinámica de campo fuerte ofrece estructuras ricas que están codificadas en la distribución de momento de fotoelectrones. Dado que usamos campos láser combinados de dos colores, podemos controlar esas dinámicas con precisiones de subciclo. Más precisamente, mostramos con la ayuda de un microscopio de reacción que podemos extraer tanto información de orbitales de electrones como dinámica nuclear dentro de una extraordinaria resolución temporal de subciclo.

Finalmente, el modelo de recolisión de campo fuerte se investiga con moléculas, a través del método de difracción de electrones inducido por láser (LIED) desarrollado previamente. Mostramos que las interferencias de electrones retrodispersados, emitidas por un campo fuerte con parámetros de bajo impacto, incorporan una orientación molecular particular que se puede reproducir cuando la molécula se considera alineada con respecto a la polarización del campo láser. Esos hallazgos parecen codificar una propiedad más profunda sobre la difracción de ondas en moléculas hasta entonces inexplorada debido a las condiciones impuestas en la difracción de electrones convencional (CED).

Résumé

Depuis la découverte de la dualité onde-corpuscule, la science a changé notre façon de percevoir la lumière et la matière, notamment à l´échelle subatomique. C'est grâce à de telles découvertes que nous avons pu développer et élargir nos connaissances au cours des deux derniers siècles, atteignant desormais ces infimes limites de la science. Prenons par exemple la célèbre expérience de la double fente de T. Young (1801). Cette expérience a été étendue après la révolution quantique du XXe siècle, révélant la diffraction d´électrons et de neutrons utilisés aujourd'hui pour mesurer la séparation des noyaux formant des structures complexes. De même, l'expérience de Michelson et Morley (1887), qui fait suite aux fondations de T. Young, a connu un succès certain en astronomie, permettant l'imagerie à haute résolution des étoiles dans l'univers. Dans cette thèse, nous utilisons de la lumière pour générer des électrons, et ainsi produire des interférences similaires à l´expérience des fentes, qui sont par la suite analyser pour en connaître les propriétés atomiques.

Sur la dynamique d'un atome, c'est-à-dire, attoscience, nous utilisons des impulsions laser ultra-rapides pour déclencher des mouvements sur une échelle de temps de la femtoseconde. Avec l'utilisation de champs laser intenses et puissants dans le régime Mid-IR, OPCPA, l'électron est ionisé avec une énergie cinétique nulle et ensuite accéléré par l'énergie pondéromotrice du laser.

La dynamique des champs forts offre des structures riches qui sont encodées dans la distribution de quantité de mouvement des photoélectrons. Puisque nous utilisons des champs laser combinés à deux couleurs, nous pouvons contrôler ces dynamiques sur une échelle plus courte que la période du laser. Plus précisément, nous montrons à l'aide d'un microscope à réaction que nous pouvons extraire à la fois des informations sur les orbitales électroniques et la dynamique nucléaire avec une extraordinaire résolution temporelle.

Enfin, le modèle de récollision en champ fort est étudié avec des molécules, grâce à la méthode de diffraction d'électrons induite par laser (LIED) précédemment développée. Nous montrons que les interférences électroniques rétrodiffusées, issues d'un champ fort avec faible paramètre d´impact, intègrent une orientation moléculaire particulière qui peut être reproduite lorsque la molécule est considérée alignée par rapport à la polarisation du champ électrique. Ces découvertes semblent encoder une propriété plus profonde de la diffraction d´ondes sur molécules jusqu'à alors inexplorée en raison des conditions imposées par la diffraction électronique conventionnelle (CED).

Acknowledgements

I would like to thank all people that contributed to the work presented in this thesis. This work would have never been possible without the trust from my advisor, the opportunity to join his team and work together for the past six years. I am grateful for the experience I got working in the laboratory, the good atmosphere and exchanges I received from my teammates and for the different collaborations I had the chance to be part of. For this, I would like to especially thank Jens biegert, my advisor.

An important part of my PhD, and probably of my career, was to participate to the Marie Sklodowska-Curie Innovative Training Network—High Intensity Coherent Nonlinear Optics (Hicono) funded by the European Union's Horizon 2020 research and innovation programme. It offered me high-quality conferences, lectures and workshops. I will certainly keep good memories and contacts from those special events. I would particularly like to thank Pr. Dr. Thomas Halfmann who was in charge of supervising this network.

Also, through Hicono network I was able to participate to one three-months period secondment in another Institute or Corporate. Thanks to this opportunity offered by Pr. Dr. Dudovich, I conducted my secondment at the Weizmann Institute of Science (Israel). Among all the stress you get while passing airport security check, I had a particularly warm and pleasant stay under Nirit Dudovich´s group, which was totally worth it. Especially, I would like to thank Gidi Alon for his good-humoured attitude and professionalism in his work in the lab, Barry Bruner for coordinating my venue and showing me the lab, and the rest of the team for interesting discussions and interactive social Thursdays: Ayelet, Shaked, Michael, Oren, Gal, Omer (thanks for the wedding invitation!).

I would also like to thank : Arne Senftleben, Su-Ju Wang, Jose Ramón Martinez Saavedra and Martin Ritcher for our fruitful collaboration. Special thanks to Vasily Tulsky for interesting discussions, live-analysis and so much patience we had to put into the preparation of our manuscript.

I also want to give my thanks to Pr. Dr. Moshammer and Pr. Dr. Thomas Pfeiffer who managed my stay at MPIK Heidelberg. Special thanks to Andreas Fischer, Philipp Cörlins, Frans Schotsch, Farshad Shobeiry for showing me their experimental HHG/Reaction Microscope setup and allowing me to participate to one of the measurements.

I would also like to thank my colleagues from ICFO : Benjamin, Xinyao, Ugaitz, Tobias, Blanca, Kasra, Lenard, Nicolas, Themis, Stefano, Adam, Mauricio, Barbara, Matthias, Iker, Hung-Wei, Ying-Hao, Daniel, Jie and Katharina for the nice

work environment.

Thank you Andrew Maxwell and Sven Augustin for your helpful input .

At last but not least, I would like to thank my parents, family and my girl-friend for their continuous support throughout all these years of my PhD studies in Barcelona.

Publications

Publications with immediate connection to this work

A. Sanchez, K. Amini, S.-J. Wang, T. Steinle, B. Blanca, J. Danek, A.-T. Le, X. Liu, R. Moshammer, T. Pfeifer, M. Ritcher, J. Ullrich, S. Gräfe, C. D. Lin, and J. Biegert. Molecular structure retrieval directly from laboratory-frame photoelectron spectra in laser-induced electron diffraction. *Nat Commun*, 12(1520), 2021.

A. Sanchez, V. A. Tulsky, K. Amini, B. D. Bruner, G. Alon, M. Krüger, X. Liu, T. Steinle, D. Bauer, N. Dudovich, and J. Biegert. Emergence and control of quantum trajectories in strong-field imaging. *Phys. Rev. Lett.*, ..(....), 2022 (submitted on May).

Other publications

K. Amini, M. Sclafani, T. Steinle, A.-T. Le, A. Sanchez, C. Müller, J. Steinmetzer, L. Yue, J.-R. Martínez Saavedra, M. Hemmer, M. Lewenstein, R. Moshammer, T. Pfeifer, M. G. Pullen, J. Ullrich, B. Wolter, R. Moszynski, F. J. García de Abajo, C. D. Lin, S. Gräfe, and J. Biegert. Imaging the renner–teller effect using laser-induced electron diffraction. *Proceedings of the National Academy of Sciences*, 116(17):8173–8177, 2019.

B. Belsa, K. Amini, X. Liu, A. Sanchez, T. Steinle, J. Steinmetzer, A.-T. Le, R. Moshammer, T. Pfeifer, J. Ullrich, R. Moszynski, C.-D. Lin, S. Gräfe, and J. Biegert. Laser-induced electron diffraction of the ultrafast umbrella motion in ammonia. *Structural Dynamics*, 8(1):014301, 2021.

X. Liu, K. Amini, A. Sanchez, B. Belsa, T. Steinle, and J. Biegert. Machine learning for laser-induced electron diffraction imaging of molecular structures. *Communications Chemistry*, 154(4), 2021.

X. Liu, K. Amini, T. Steinle, A. Sanchez, M. Shaikh, B. Belsa, J. Steinmetzer, A.-T. Le, R. Moshammer, T. Pfeifer, J. Ullrich, R. Moszynski, C. D. Lin, S. Gräfe, and J. Biegert. Imaging an isolated water molecule using a single electron wave packet. *The Journal of Chemical Physics*, 151(2):024306, 2019.

Contents

List of Figures

Physical Constants

In this thesis, we will refer to the Hartree atomic units (a.u.), unless otherwise stated. It is a convenient system for atomic physics, in which the four following physical constants are unity:

$$\hbar = e = m_e = a_0 = 1 \tag{1}$$

The speed of light is therefore equal to $c = 137$ a.u.

Physical quantity	atomic units (a.u.)	SI units
mass	m_e	$9.109\,38 \times 10^{-31}\,\mathrm{kg}$
charge	e	$1.602\,18 \times 10^{-19}\,\mathrm{C}$
length	a_0	$5.291\,77 \times 10^{-11}\,\mathrm{m}$
energy	E_h	$4.359\,74 \times 10^{-18}\,\mathrm{J}$
reduced Planck constant	$\hbar$	$1.054\,57 \times 10^{-34}\,\mathrm{J\,s}$
electric field	$V_0 = e/(4\pi\,\epsilon_0\,a_0^2)$	$5.142\,21 \times 10^{11}\,\mathrm{V\,m^{-1}}$
laser intensity	$0.5\,\epsilon_0\,c\,V_0^2$	$3.509\,45 \times 10^{16}\,\mathrm{W\,cm^{-2}}$
time	$\hbar/E_h$	$2.418\,88 \times 10^{-17}\,\mathrm{s}$
velocity	$a_0\,E_h/\hbar$	$2.187\,69 \times 10^{6}\,\mathrm{m\,s^{-1}}$
momentum	$\hbar/a_0$	$1.992\,85 \times 10^{-24}\,\mathrm{kg\,m\,s^{-1}}$

TABLE 1: atomic to SI units conversion

To my family

Chapter 1

Introduction

Light and electrons have both the properties of particle-wave duality in which they can be described as elementary particles (point-like) or electro-magnetic waves. For example, the elementary particle of light is called a photon and it is quantized by its energy with $E = \frac{h\omega}{2\pi} = \frac{hc}{\lambda}$, where ω is the angular frequency of the electro-magnetic wave, λ its wavelength, c the speed of light and h the Plank's constant. Every single source of light has its specific spectrum defined by the amplitude (number of photons with the same energy per time unit) and its bandwith (the quantity of energy covered by the spectrum). In turn, every object behaves in a different way when shinning light on them. Naturally, the light can scatter off (diffusion), get absorbed (heating) or simply be transparent to the medium. When the photon is absorbed, its energy is converted to the system and leads to internal dynamics. At low energies, in the terahertz regime, the wavelength is sufficiently long to excite collective modes via resonance. On the contrary, when the photon is scattered, it carries on a momentum $p = \frac{h}{\lambda}$ which contains information about the structure. If λ, also called deBroglie wavelength, is larger than the target size, the information is lost. The above statement is well known from the Heisenberg uncertainty principle [1].

Beside spatial resolution, the temporal resolution is another criteria that needs to be simultaneously met for imaging fundamental processes. In nature, processes are either triggered by chemical, biological or physical phenomena that arise at different timescale as illustrated in Fig. 1.1. Large time scales are usually referred as planetary motions, for example our calendar based on the earth period around the sun which is approximately 1 year. Total eclipse for a particular geographical region happens approximately every two centuries. Galaxy rotations happen at a much larger timescale, hence the probability of collisions is very low in respect of human life. Going towards fast motions, the organic compounds of life such as DNA (or RNA), are assembled/disassembled within microseconds (10^{-6} s) [2]. Fastest electronic devices can operate at nanoscale (10^{-9} s), that is approximately the speed at which microprocessors trade data in computers. Molecular dynamics have a range of between 10^{-12} to 10^{-15} s. Below that range, electrons move inside atoms within hundreds attoseconds (as 10^{-18} s).

An important application for imaging tiny objects with light in dense materials is X-ray imaging [3, 4]. X-rays are high-energy electromagnetic radiations ranging from 10 pm to 10 nm wavelength. The size of an atom is about $r \approx 1$ Å $\equiv 100$ pm, which renders the technique capable of capturing atomic

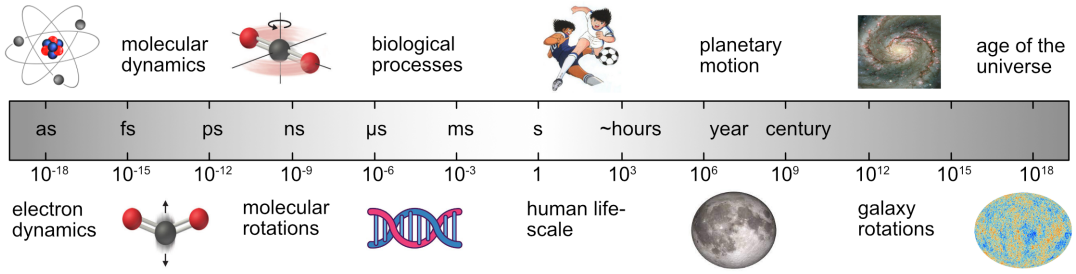

FIGURE 1.1: **Timescale of different processes that governs the astronomy, biology, chemistry and physics.**

motions. However, for the method to be successful, the distance size to be measured needs a coherent illumination [5]. If multiple waves hit the sample, they have to carry the same frequency and the same phase in order to interfere constructively at the camera/detector. Thus, it is extremely challenging to reduce the wavepacket duration and maintain both the spatial and temporal coherence. A better coherence can be achieved with electrons since the atomic incoherent electron scattering is $4/a^2q^4$ times the atomic incoherent X-ray scattering where a is the Bohr radius and q the momentum transfer [6]. Electrons are accelerated in cyclotrons to reach high kinetic energy and reduce deBroglie wavelength. While the method of ultrafast electron diffraction gives a complete scheme to study reactive intermediates, the technique is limited to a temporal resolution of 150 fs or longer and enough brightness for approaching single shot atomic resolution conditions [7]. Therefore, current developments aim to reduce space charge [8] or use relativistic electron bunches [9]. Obviously, versatile laboratory-scale tabletop methods that provide the combined spatial and temporal resolutions would signify a breakthrough. Nowadays, such applications exist in strong-fields physics thanks to the continuous development of ultrashort laser pulses, involving the generation of coherent X-rays, known as High-Harmonics-Generation (HHG) [10, 11, 12], attoseconds wavepacket interferometry [13, 14, 15], and Laser-Induced Electron Diffraction (LIED) [16, 17, 18, 19, 20].

Strong-Field (SF) physics uses ultrashort pulses with intense and low-frequency fields. The quasi-static field is strong enough to alter the coulomb field barrier. As a result, the combined laser together with the coulomb field creates a potential barrier in which the initially bound electron may tunnel [21, 22]. As the electric fields couples all bound states to the continuum it is generally no longer possible to speak about discrete or intermediate states. In this thesis, a laser field at a central wavelength of about 3.2 μm and peak intensity of nearly $I_0 \approx 10^{14}\ W.cm^{-2}$ is shown to lead to an energy of interaction (ponderomotive energy $U_p = \frac{E_0^2}{4w_0^2}$) of 10^2 eV. For the electron to live in the presence of the field, it means that it must have interacted with at least 247 photons. This is approximately 5 to 10 times the binding energy of valence electrons. Therefore, it is clear that the notion of perturbation is meaningless and once ionized, the electron behaves free as if the atom is not present. SF environment can be described by means of semi-classical theories and at the same time meet all criteria of what modern science responds

to: discreteness, coherence and diffraction (see Fig.1.2).

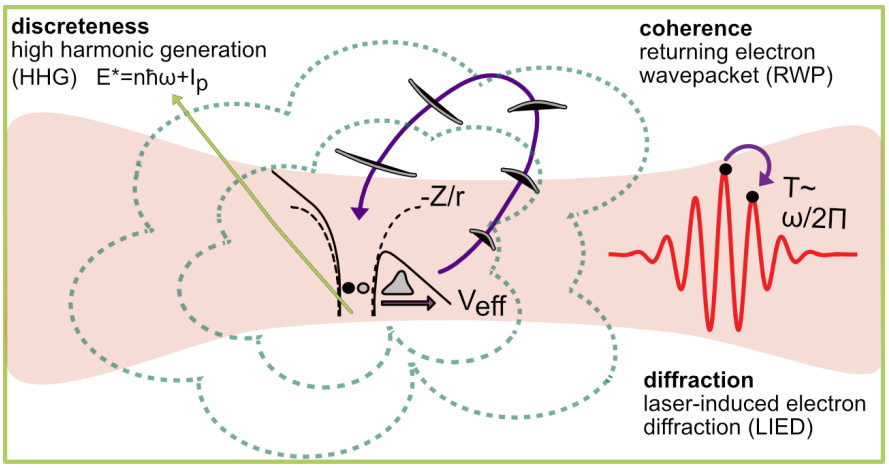

FIGURE 1.2: **Strong fields physics.** Strong-fields ionization and recollision described within the so-called 3-step model [23, 24, 25]. 1. Tunneling ionization of a bound wavepacket electron. 2. The electron wavepacket is accelerated in the presence of the fields. The longer the electron stays in the continuum, the greater is the wavepacket extent and the so-called deBrogle wavelength. 3. The electron can either recombine with its parent ion leading to discrete odd harmonics, or scatter off the structure leaving a diffraction pattern that can be recorded with a 3D momentum detector. The full process is coherent since the electron encodes its initial configuration in its wavefunction. The time needed for the electron to come back is proportional to the laser period.

The strength of Strong-fields is conditioned by the ponderomotive energy which scales quadratically with the laser wavelength $U_p \approx I\lambda^2$. As a result of the thinning of the Coulomb barrier, the electron tunnels out and gets accelerated into the continuum with an average kinetic energy that corresponds to the ponderomotive energy. Once the electron is driven back to the target, it can either recombines with its parent ion and emits a coherent light of frequency proportional to the electron kinetic energy, inelastically scatters and kicks out a second electron, or elastically scatters leaving an imprit of the target structure. The two last conditions described above strongly depend on the laser peak intensity whether the electron is likely to be scattered elasticaly or inelasatically. For the first time, it was discovered by l'Huiller et al. [26] a "knee structure" in the dication yields of Krypton. One year later, they concluded [27] that the doubly charged ions were directly produced from the atomic ground state in the low to moderate intensity regime while the yields dependency in the high intensity regime was following a gaussian fit, revealing a sequential ionization from the intermediate singly charged ion state. Similar results were found [28, 29, 30, 31] revealing a clear transition from non-sequential (NS) to sequential double ionization (SDI) as function of the peak intensity. In this thesis, the laser parameters are essentially performed in the sequential regime from moderate to high-intensity regime, where the electrons are more likely to scatter off the target elastically.

On the other hand, using long-wavelength laser fields comes at a cost. Driving the wavepacket on longer timescales spreads out the electron density which results in lower scattering efficiency scaling as λ^{-4} [32, 33]. To solve this problem, a 160 kHz high-repetition rate OPCPA was built at ICFO [34, 35]. Operating together with a 10 kHz Reaction Microscope detection capabilities [36, 37], it allows data acquisition to turn on coincidence techniques in order to sample each electrons signal with its parent ion channel, accordingly. Figure 1.3 summarizes different strong fields regimes as function of the laser peak intensity I_0 and the laser wavelenght λ_0. When the binding energy I_p or the laser frequency ω_0 is considerably higher than the ponderomotive energy U_p, lowest-order perturbation theory can be applied. With the increase of the laser intensity, non-pertubative effects such as Above-Treshold-Ionization (ATI) take place when $U_p > \omega_0$. This regime is called multiphoton ionization (MPI). When U_p is larger than the binding energy I_p and the laser frequency w_0, the ionization dynamics take place in a small fraction of the laser period. That is the quasi-static regime and the main ionization mechanism is tunneling. By increasing the intensity further, the energy shift caused by the effective potential can be superior than the binding energy I_p of the valence electron. This phenomenon is named "Over the Barrier Ionization" (OBI) where the electron can escape classically. At these moderate intensities we generally assume the magnetic component of the laser fields set to zero $B = \nabla A(t) = 0$ [38]. Such treatments refer to the "dipole approximation" [39]. Non-dipole effects start to be considered when the amplitude in the propagation direction of the beam is of the order of one atomic unit $\beta \approx \frac{U_p}{2\omega c} = 1$ [40]. The radiation pressure limits arise when twice the kinetic energy in the propogation direction exceeds 1 a.u. [41]. At very high intensities, the electron is considered relativistic when twice the ponderomotive energy is approaching its rest mass energy.

In this thesis, a 3.2 µm wavelength OPCPA laser source is used to probe ultrafast dynamics at reasonably intense fields I=$10^{14}\, W.\mathrm{cm}^{-2}$ (see green star in Fig. 1.3) with the well established LIED method [17, 18, 19, 20, 42, 43, 44]. First, we introduce the necessary theoretical knowledge in Chap. 2 and show our experimental methodology in Chap. 3, which has led to the mid-IR LIED results shown in [20, 38, 43, 44]. Then, our experimental results are sorted and presented in three chapters—the first, Chap. 4, is dedicated to an introduction towards strong field holography, which is a complementary method to LIED that allows extracting information on the target structure orbitals. Notably, we illustrate this chapter by presenting deep Mid-IR (MIR) fan-like interferences and an application using a two-color combined laser field. Then, later in Chap. 5, we use that same two-color MIR fields to influence the yield of the backscattered electrons used in LIED. Since the photoelectron momentum distribution in strong fields very much depends on the keldysh parameter $\gamma = 2\sqrt{\frac{I_p}{U_p}}$, we compare the MIR measurement with another two-color near-IR (NIR) fields measurement. The results are presented together with TDSE calculations, providing a better understanding of the underlying mechanisms. In particular, we show that this variant two-color

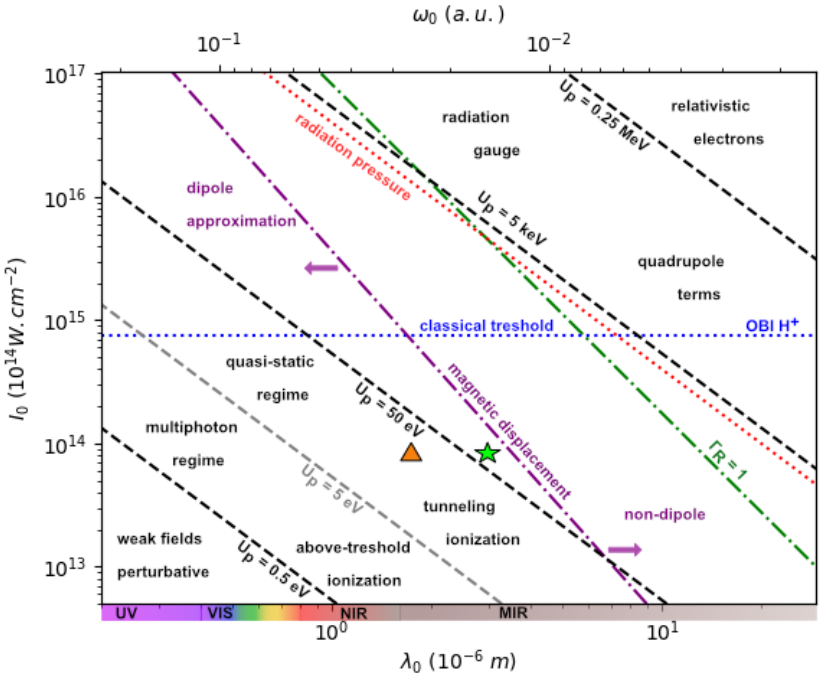

FIGURE 1.3: **Wavelength and intensity dependency of the different strong-fields regimes**. When the laser ponderomotive energy U_p is about the same order as the binding energy of the valence electrons non-perturbative effects such as above-treshold ionization (ATI) start to occur. At longer wavelengths, the responsible mechanism of ionization is tunneling. The limit of the dipole approximation is shown by the purple dash-dotted line. The green star indicates the laser wavelength and peak intensity used in this thesis. The orange triangle is the second harmonic generation of the green star marker. At longer wavelengths, there is a risk the electron wavepacket completely misses the target when $\Gamma_R = \frac{\sqrt{U_p^3 I_p}}{3c^2\omega} = 1$ [40]. Dotted red and blue lines are the radiation pressure and OBI limits respectively. See text for more details

LIED reduces the number of returning trajectories to exactly one within an extensive momentum range, where the sub-femtoseconds temporal resolution of this method can be restored. Finally, we dedicate Chap. 6 to backscattered LIED electrons from molecules, notably with the development of a novel method ZCP (Zero-Crossing Points), resulting in a faster and more accurate algorithm to extract molecular structure. Then, LIED diffraction cross sections are compared to the well-known, established IAM model used in gas-phase electron diffraction. We show that the molecular interferences can be fitted with three different methods, all converging to the same results. Surprisingly, we found the backscattered interferences embedded a specific orientation dependency, therefore responsible for the high accuracy observed in LIED. In the end, we summarize our findings in Chap. 7.

Chapter 2

Strong-field ionization and recollision

As explained in the introduction, strong-field (SF) phenomena are non-perturbative effects that can be described with rather simple tools. Indeed, theoretical foundations of strong-field physics in atoms are based on models that have been known for a long time.

For example, the time-dependent Schrödinger equation (TDSE) in the single active electron (SAE) approximation has been so far, the most successful to describe the experimental observations [45, 46, 47, 48, 49, 50, 51]. However, TDSE calculations in strong-fields are often time-consuming due to the large wavelength-scaling photoelectron excursion. In that sense, a time-dependent surface flux method was suggested in [52] to keep the numerical grid relatively small. Yet, TDSE cannot be treated or disentangled easily in the way the reader wants.

Another popular tool to describe strong-fields processes can be derived analytically with the so-called Gordon-Volkov solution. The theory approach by Keldysh [53], and later contributions by Faisal [54] and Reiss [55], known as Keldysh-Faisal-Reiss (KFR) theory lead to the "strong-field approximation" (SFA). It was later developed by Lewenstein [25] for the applications in high-harmonic-generation. A semi-classical treatment applying the saddle point approximation on the KFR-theory leads to the quantum orbit theory [56, 57].

2.1 Schrodinger formalism

We start with a quantum description of one electron in the presence of an electrostatic fields. The dynamics of a wave function is governed by the time-dependent shrödinger equation (TDSE)

$$i\frac{\partial}{\partial t}\Psi(r,t) = \mathcal{H}\Psi(r,t) \tag{2.1}$$

where $\mathcal{H}$ defines the Hamiltonian operator.

We use the electric dipole approximation to render our problem gauge invariant

$$\mathcal{H} = \mathcal{T} + V_0(r) + V_{ext}(r,t) \tag{2.2}$$

where $\mathcal{T} = \frac{p^2}{2m}$ is the kinetic operator, V_0 is the coulomb potential (or electrostatic potential) and V_{ext} is the potential energy defining the interaction between the electron and the external fields.

In the absence of a magnetic field, we can take the vector potential down to zero, that is the dipole approximation $V_{ext}(r,t) \rightarrow V_{ext}(t)$. There are now two particular solutions of potentials V_{ext} which gives the field $E = -\nabla\Phi - \partial_t A$.

Either we use the length gauge,

$$\Phi_{LG}(r,t) = -r.E(t) \tag{2.3}$$

$$A_{LG}(r,t) = 0 \tag{2.4}$$

or the velocity gauge

$$\Phi_{VG}(r,t) = 0 \tag{2.5}$$

$$A_{VG}(r,t) = -\int_0^t E(t')dt' \tag{2.6}$$

Hence, the Hamiltonian in the length gauge reads

$$\mathcal{H}^{LG} = \frac{p^2}{2m} - qE(t).r + V_0(r) \tag{2.7}$$

while, in the velocity gauge it reads

$$\mathcal{H}^{VG} = \frac{(p - qA_{VG}(t))^2}{2m} + V_0(r) = \frac{p^2}{2m} - \frac{q}{m}A_{VG}(t).p + \frac{q^2}{2m}A_{VG}^2(t) + V_0(r) \tag{2.8}$$

In the velocity gauge, a simplification can be made by dropping the last term proportional to $A_{VG}^2(t)$ out of Eq. 2.8 since it doesn't contain any physical meaning [58, 59]. It should be pointed out that another possible third frame, acceleration form, can be derived from the length gauge [60].

To find the wavefunction at some later time t, one can use the time evolution operator

$$\Psi(r,t) = U(t,t_0)\Psi(r,t_0) \tag{2.9}$$

$$i\frac{\partial}{\partial t}U(t,t_0) = \mathcal{H}U(t,t_0) \tag{2.10}$$

Given the time-dependent Hamiltonian, if it commutes at different times [61], the right hand of Eq. 2.10 reads

$$\mathcal{H}U(t_1,t_0) = e^{-i\int_{t_0}^{t_1}\mathcal{H}(t)dt} \tag{2.11}$$

2.2 Strong-Field Approximation

Let's consider a bound electron with binding energy I_p as initial state t_0. In first-order time-dependent perturbation theory, the time-dependence of the initial state and the final state only contains the time evolution according to the unperturbed Hamiltonian. Following [22], one can use a Gordon–Volkov–Hamiltonian $\mathcal{H}^{(V)}$ which is diagonal in momentum space inside the dipole approximation to govern the free motion of the electron in the laser field, therefore, reproducing Keldysh work [53].

$$\mathcal{H}^{(V)} = \frac{1}{2}(p + A(t))^2 |\Psi_p^{(V)}(t)\rangle \tag{2.12}$$

with the Gordon-Volkov state

$$|\Psi^{(V)}(t, t_i)\rangle = e^{-iS_p(t,t_i)}|p\rangle, \quad S_p(t, t_i) = \frac{1}{2}\int_{t_i}^{t} dt'(p + A(t'))^2 \tag{2.13}$$

where $|p\rangle$ are momentum eigenstates, $\langle r|p\rangle = e^{ip.r}/(2\pi)^{3/2}$

Considering the influence of the field strong as compared to the influence of the long-range Coulomb potential, the final continuum state of the electron $\Psi(t)$ can be replaced by a Gordon-Volkov solution $\Psi^{(V)}(t)$. Then, the strong-field approximation (SFA) transition amplitude reads

$$M_p^{SFA} = -i\int_{t_0}^{t} dt' \langle \Psi_p^{(V)}(t', t)|\mathcal{H}_I(t')|\Psi_0(t')\rangle, \tag{2.14}$$

where $\mathcal{H}_I(t) = p.A(t) + A^2(t)/2$ is given here in the velocity gauge.

Equation 2.14 can lead into the simple expression [55],

$$M_p^{SFA} = -iB\int_{-\infty}^{+\infty} e^{iS_p(t_i)} \tag{2.15}$$

$$S_p(t_0) = -\int_{t_i}^{+\infty} dt' \frac{(p + A(t'))^2}{2m} - \int_{-\infty}^{t_0} I_p\, dt' \tag{2.16}$$

where B is the prefactor which contains the dipole matrix element $\langle \Psi_p^{(V)}|\mathcal{H}_I(t_0)|\Psi_i\rangle$ and $S_p(t_0)$ is the quasiclassical action.

2.3 Higher-order SFA

Rescattering probability amplitude can be derived from Eq. 2.15 including a further interaction with the parent ion [56] at some intermediate time t_1 defined as the recollision time. According to [22] and [62], the probability amplitude for

rescattered electrons is given by

$$M_p^{resc}(t) = -\int_{-\infty}^{t} dt_1 \int_{-\infty}^{t_1} dt_0 \int_{-\infty}^{+\infty} dk^3 \langle \Psi_p^{(V)}(t_1)|\mathcal{H}_I(t_1)|\Psi_k^{(V)}(t_1)\rangle \times \langle \Psi_k^{(V)}(t_0)|\mathcal{H}_I(t_0)|\Psi_i(t_0)\rangle \quad (2.17)$$

For t $\rightarrow$ $+\infty$ the equation can be recast into

$$M_p^{resc} = -B^{resc} \int_{-\infty}^{+\infty} dt_1 \int_{-\infty}^{t_1} dt_0 \int_{-\infty}^{\infty} dk^3 \, e^{iS_p^{resc}(t_0,t_1,k)} \quad (2.18)$$

with the corresponding quasiclassical action

$$S_p^{resc}(t_0,t_1,k) = -\int_{t_1}^{+\infty} \frac{(p+A(t'))^2}{2m} dt' - \int_{t_0}^{t_1} \frac{(k+A(t'))^2}{2m} dt' - \int_{-\infty}^{t_0} I_p \, dt' \quad (2.19)$$

where B^{resc} is a prefactor analogous to B in Eq. 2.15. From Eq. 2.19, we can retrieve the three step model proposed by Corkum in 1993 [24]. The last integrand shows the tunneling process from an initial state to the exit barrier at some time t_0. The middle integrand is the action of a closed electron trajectory from t_0 to t_1 in the presence of the fields with an intermediate momentum k. Finally, the first integrand shows the action of an electron trajectory with drift momentum p from t_1 to infinity. Equation 2.19 has the form of a path integral [63], where the integration needs to be carried out for a range of t_0, t_1 and intermediate momentum k.

2.4 Saddle point approximation

In this section, we will take a look at the strong-field approximation solutions presented in Sec. 2.2 and Sec. 2.3 by applying the saddle point approximation [64]. The later, also referred in literature as method of steepest descent or stationary phase approximation [65], is a standard method to solve integrals of the form

$$I(\sigma) = \int_a^b f(z) e^{i\sigma\phi(z)} dz \quad (2.20)$$

Assuming a function $\phi(z)$ that rapidly oscillates for large values of $\sigma >> 1$ and f(z) a slowly changing function. One can approximate Eq. 2.20 as a sum of N saddle points between a to b where $\partial\phi(z_n)/\partial z_n = 0$.

$$I(\sigma) \approx \int_{n=1}^{N} f(z_n) \sqrt{\frac{2\pi i}{\sigma \partial^2\phi(z)/\partial z^2|_{z_n}}} e^{i\sigma\phi(z_n)} \quad (2.21)$$

The saddle point approximation can be applied to the probability amplitude to reveal an intuitive picture of semiclassical electron trajectories known as quantum orbits [57].

2.4.1 Quantum orbits

First, we start by applying the saddle point approximation to Eq. 2.15 for the direct electrons.

$$\frac{\partial S_p(t_0)}{\partial t_0} = 0 \rightarrow \frac{(p + A(t_0))^2}{2m} = -I_p \tag{2.22}$$

To conserve the electron energy, as shown in Eq. 2.22, t_0 must be a complex number. One can picture the underlying mechanism as an electron crossing a classically forbidden tunneling barrier region (see Fig. 2.1).

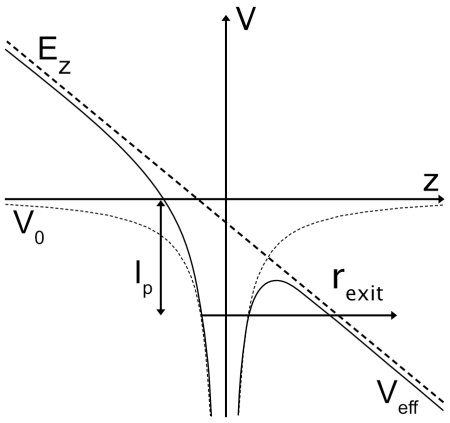

FIGURE 2.1: **Tunneling ionization.** Electron with given binding energy I_p and potential V_0, can tunnel out in the presence of a strong external field (Ez), as illustrated by the black arrow.

An estimation of the electron position at the barrier exit can be done by integrating the electron velocity along the imaginary time axis.

$$r_{exit}(t_0) = \frac{1}{m} Re[\int_{t_0}^{Re\, t_0} p + A(t')dt'] \tag{2.23}$$

At the exit, the electron velocity entering the continuum reads

$$v_{exit}(t_0) = \frac{1}{m}(p + A(Re\, t_0)) \tag{2.24}$$

The direct electron amplitude in the saddle point approximation is then given by

$$M_p^{dir} \approx -iB \sum_{n=1}^{N} \sqrt{\frac{2\pi i}{\partial^2 S_p(t)/\partial t^2|_{t_n}}} e^{iS_p(t_n)} \tag{2.25}$$

For the rescattered electrons, the same procedure can be applied. As shown in Eq. 2.19 the rescattering amplitude is given as function of three parameters, so one has to find the three corresponding saddle points

$$\frac{\partial S_p(t_0, t_1, k)^{resc}}{\partial t_0} = 0 \rightarrow \frac{(k + A(t_0))^2}{2m} = -I_p \tag{2.26}$$

$$\frac{\partial S_p(t_0,t_1,k)^{resc}}{\partial t_1} = 0 \rightarrow \frac{(k+A(t_1))^2}{2m} = \frac{(p+A(t_1))^2}{2m} \tag{2.27}$$

$$\frac{\partial S_p(t_0,t_1,k)^{resc}}{\partial k} = 0 \rightarrow \frac{1}{m}\int_{t_0}^{t_1} k + A(t')dt' = 0 \tag{2.28}$$

A particular solution of the last integral shows that k "the canonical momentum" is conserved along the close trajectory

$$k = -\frac{1}{t_1 - t_0}\int_{t_0}^{t_1} A(t')dt' \tag{2.29}$$

According to [62], the rescattering amplitude in the saddle point approximation can be given by

$$M_p^{resc} \approx -B^{resc}\sum_{n=1}^{N}\frac{(2\pi i)^{5/2}}{\sqrt{det(\Sigma|_{(t_{0,n},t_{1,n},k_n)})}}e^{iS_p(t_{0,n},t_{1,n},k_n)} \tag{2.30}$$

where $\Sigma|_{(t_{0,n},t_{1,n},k_n)}$ is the Hessian matrix of the action $S_p(t_{0,n},t_{1,n},k_n)$. The determinant of the matrix accounts for a regularization of the path integration, also known as fluctuation or stabilization factor [63]. Among them, one can find the wave-packet spreading for a free particule given as $\approx (1/\Delta t)^d$, where d is the dimension.

2.4.2 Quasi-free electron

As shown in the introduction of this section, classical trajectories emerge from the saddle point solutions. In the limit $I_p \rightarrow 0$, the saddle points approach real numbers, leading to purely classical solutions. Similarly, when the laser period is long compared to the tunneling ionization, the same agreement is met as one can see from Fig. 2.2. Both SFA via the saddle point approximation and the classical calculations overlap well in the ionization and rescattering time predictions for the first return trajectory.

There are other different methods frequently used to study and make predictions about a certain type of orbits. For example, CTMC models [66, 67, 68] are based on classical calculations and include the long-range dynamics of the electron in the continuum. Other models, such as QTMC [69], SCTS [70], maybe more sophisticated since it includes and propagates the phase of one initially bound electron subsequently driven in the fields to account for a coherent summation at the virtual detector. In Chap. 4, we will introduce and go through one of these methods that include coulomb corrections during the tunneling and propagation steps.

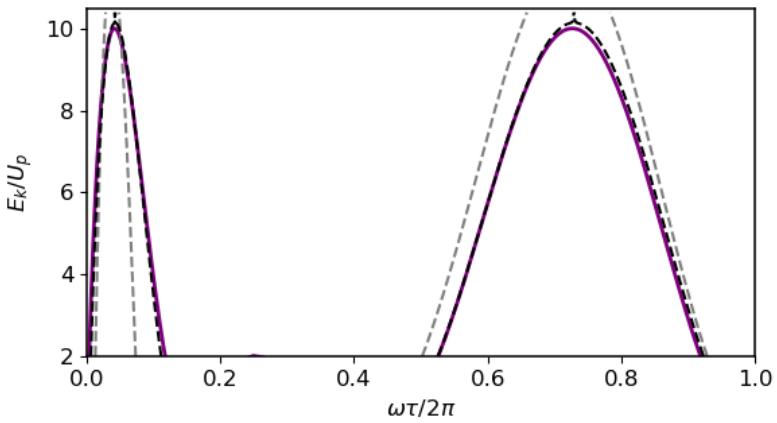

FIGURE 2.2: **SFA vs classical.**Classical and strong fields approximation predictions for two different wavelength 3200 nm (black dahsed line) and 800 nm (gray dashed line) at a fixed peak intensity of 6.0 10^{13} W.cm^{-2}. The classical calculations are the same at both wavelength (purple line). In the long-wavelength regime, when $I_p << U_p$, both calculation agree well as shown by the sharp cut-off.

2.5 Plane wave approximation

One important assumption of laser-induced electron recollision and diffraction (LIED) is based on the Born approximation or plane wave scattering. In the following subsections, we show the scattering amplitude as it is defined in the independent atomic model (IAM). Then, we present TDSE calculations that show the returning wavepacket extent at different snapshots in the laser fields.

2.5.1 First born approximation

Let´s define an incident wave $e^{ik_i.r}$ and a scattered wave $e^{ik_f.r}$, with same absolute values for the momentum k_i and k_r. We can define the momentum transfer as

$$q = k_f - k_i \tag{2.31}$$

and its magnitude

$$q = 2k\sin(\frac{\theta}{2}) \tag{2.32}$$

The scattering amplitude in the first born approximation reads

$$f^B = -\frac{1}{2\pi}\langle\Psi_f|V|\Psi_i\rangle = -\frac{1}{2\pi}\int V(r)e^{-iq.r}dr \tag{2.33}$$

and assuming V(r) a central symmetric potential

$$f^B = -\frac{2}{q}\int_0^{+\infty} rV(r)\sin(q.r)dr \tag{2.34}$$

2.5.2 Scattering by a rigid molecule

Let´s now assume a molecule made of N independent atoms modeled by a local potential $V_i(r')$ and located at r=R_i. According to [71], the total scattering amplitude is given by

$$f^B = -\frac{1}{2\pi}\int[\sum_{i=1}^{N} V_i(r-R_i)]e^{-iq.r}dr \tag{2.35}$$

$$= \sum_{i=1}^{N} e^{-iq.R_i}[-\frac{1}{2\pi}\int V_i(r-R_i)e^{-iq.(r-R_i)}dr] \tag{2.36}$$

$$= \sum_{i=1}^{N} e^{-iq.R_i}[-\frac{1}{2\pi}\int V_i(r')e^{-iq.r'}dr'] \tag{2.37}$$

$$= \sum_{i=1}^{N} f_i^B e^{-iq.R_i} \tag{2.38}$$

where f_i^B is the individual scattering amplitude for the ith atom and $e^{-iq.R_i}$ the phase factor. The latter is responsible for the interferences between different scattering centers.

2.5.3 Wavepacket extent

While the wavepacket dispersion can be seen as an obstacle in a strong field measurement in the mid-infrared (MIR) regime, it also provides better "plane-wave" conditions for the recolliding electrons resulting in a "cleaner" diffraction pattern which, in turn, can be interpreted using scattering models [42].

To illustrate this statement, we have run two TDSE simulations using the free open-source software Qprop [72] and estimated the curvature of the recolliding electrons driven by two different laser fields. Figure 2.3 **a-d** (λ=800 nm) shows the wavefunction density probability taken at different time in the laser fields as indicated by the left-lower corner inset. We used three cycles (1.5 FWHM) to have one clear peak where the tunneling ionization is triggered. After approximately three quarters of a cycle later (see Fig. 2.3 **d**), we can see Spyder fringes due to interferences between direct and forward scattering electrons [47, 73]. The same is observed in panel **e** (λ=3200 nm) but with less visibility. The snapshot in **e** is taken at the same time as in **d**. With the 788 nm laser fields, we notice a curvature of about 6Å for 15Å extension. An estimation of the total spatial extent will be 15x2$\approx$ 30Å. When driving the fields with the 3200 nm laser fields, the curvature is only 5Å for 65Å extension.

Thus, Mid-IR (MIR) strong laser fields are powerful tools for the use of ultrafast electron diffraction, delivering shot-to-shot measurement at low impact parameters b$\approx$0.

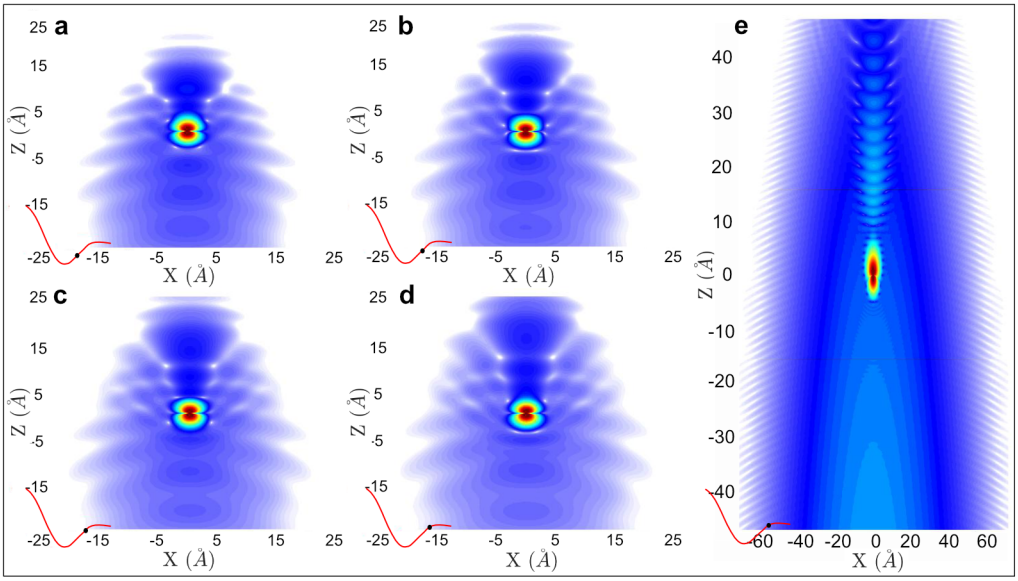

FIGURE 2.3: **TDSE numerical calculation using the free open-source software qprop. a-d**. wavefunction density probability distribution in three cycle pulse at a peak intensity of 1.0 10^{14} W.cm^{-2} and a laser wavelength of 800 nm. Snapshots taken at different time indicating by the black dot in the left-lower corner inset. **e**. Same as **d** with a laser wavelength of 3200 nm and a slightly different intensity 0.6 10^{13} W.cm^{-2}. In the MIR regime, the wavepacket curvature is only 6 Å for 130 Å extent.

Chapter 3

Experimental Methodology

The key components of our investigations is based on a unique combination of a high-repetition rate, ultrashort pulse, mid-IR optical parameteric chirped-pulse amplification (OPCPA) source with a Reaction Microscope (ReMi), an advanced multi-particle momentum imaging spectrometer. First, we present an overview on the working principle of our home-made OPCPA laser source in Sec. 3.1. Then, the ReMi detection system is introduced in Sec. 3.2 together with the data analysis steps to provide a more fundamental understanding of the experimental results presented in the next chapters.

3.1 Generation of Mid-IR ultrashort laser pulses

As discussed in the previous chapter, a few-cycle laser source in the mid-IR allows tunneling ionization and ponderomotive scaling, yet a drawback in this context is the fact that the cross sections of the ionization and recombination/rescattering processes scale unfavorably with wavelength [32, 33]. The key to overcome this downside, and reduce measurement times is to utilize laser systems that generate stably reproducible electric waveforms at repetition rates orders of magnitudes higher than most commercial systems. But with increased repetition rates the pulse energies decrease at common power scaling levels. To still maintain suitable intensities for strong-field physics of 10^{13}-10^{15} W/cm^2 our group had to pioneer sources based on optical parametric chirped-pulse amplification (OPCPA) in the mid-IR [34].

3.1.1 Passive CEP stability

OPCPAs have been designed with the intention to provide Mid-IR few cycle pulse with stable carrier-envelope phase (CEP). Until recently, typical laser sources were generated via resonant modes in cavity reaching a Titanium doped sapphire (Ti:Sa) crystal, where highly non-linear processes, known as self-amplitude and self-phase modulation, take place. However, the shortest pulses obtained this way are limited by their bandwith limit and few hours CEP-stability. When generating ultrashort laser source in the Mid-IR spectral range (above 2 µm), this problem becomes even more challenging [74].

In [75], an alternative scheme for producing passive stabilized CEP was suggested employing a non-linear optical process, difference frequency mixing (DFG),

from a two-color fibre laser. In DFG, two incident photons $\omega_1 < \omega_2$ are subtracted to generate a new frequency $\omega_3 = \omega_1 - \omega_2$ in a non-linear media as illustrated in the next subsection. We use the comercial available Femtofiber Scientific (FFS) laser system from Toptica Photonics AG which consists of an Erbium (Er) doped fiber oscillator and subsequent fiber amplifiers operating at 100-MHz repetition rate. The seed pulses of the OPCPA system consists of femtosecond pulses with center wavelengths at 1075 and 1560 nm corresponding to a difference frequency conversion of 3200 nm.

3.1.2 Optical parametric amplification

Non-linear effects in suitable materials can be used to generate coherent and intense pulses at any wavelengths. Yet we will see it has to match some properties in order to be efficient.

When exposed to an intense laser field with linear polarization, the electrons of the atoms in a non-linear media are driven back and forth. Depending on the susceptibility of the material and the laser field intensity, higher orders of the effective potential can become significant, generating new frequency components. The non-linear polarization P following the interaction of an external electric field $\mathcal{E}$ on non-linear media can be expressed as a function of the electric permittivity in free space ϵ_0, the first $\chi^{(1)}$, second $\chi^{(2)}$ and third $\chi^{(3)}$ order non-linear optical susceptibility.

$$P = \epsilon_0[\chi^{(1)}\mathcal{E}^{(1)}(t) + \chi^{(2)}\mathcal{E}^{(2)}(t) + \chi^{(3)}\mathcal{E}^{(3)}(t) + ...] \tag{3.1}$$

Therefore, new frequency components can be generated depending on the incoming frequencies, incident angles, and field strength. An essential property of frequency conversion processes is the energy conservation $\Delta\omega = 0$ and the conservation of wave vectors $\Delta k = 0$ known as phase matching [76]. Among the non-linear frequency conversion, one can find the sum- (SFG) and the difference-frequency generation (DFG) as previously mentioned in Sec. 3.1.1. Another non-linear frequency conversion is the second-harmonic generation (SHG) which uses two incident photons of the same frequency ω_0 to convert into a sum of twice greater frequency $\omega_1 = 2\omega_0$ (half the wavelength).

In the DFG process, the energy of the incident photon ω_1 has to be split into ω_2 and ω_3 to respect the energy conservation. Thus, part of the ω_1 energy is converted to the second incident photon ω_2, which serves as an amplification procedure better known as optical parametric amplification (OPA) (see Fig. 3.1). The incident beam at larger frequency ω_1 is referred to later in our setup's description as the pump, while the amplified frequency ω_2 and the resulting frequency ω_3 are called the signal and the idler, respectively.

Finally, our system uses a chirped-pulse amplification (CPA) scheme as proposed in 1985 [77] by the same authors who won the 2018^{th} Nobel prize for groundbreaking inventions in the field of laser physics. The method consists

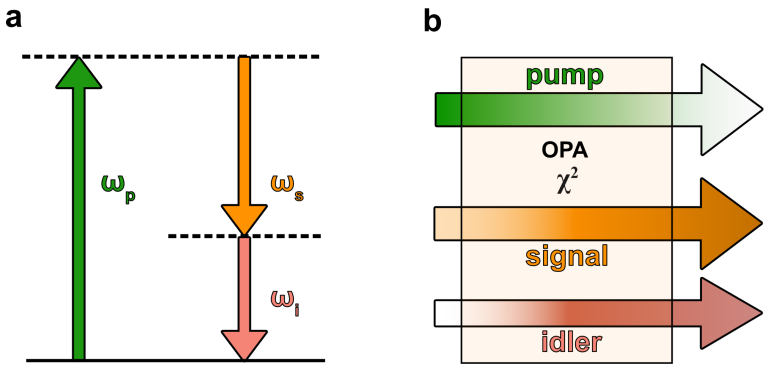

FIGURE 3.1: **Optical parametric amplifier sketch. a**. Due to energy conservation, the incident beam frequency ω_p is split into two intermediates frequencies ω_s and ω_i. **b**. The incident beam, referred as pump, allows the amplification of the second incident beam, referred as signal, during the interaction with the non-linear crystal χ^2. A third pulse, referred as idler, is generated through this process.

of stretching the pulse down to picoseconds to prevail from plasma and damages that could occur during the different amplification stages. Then, the pulse is compressed at the end of the last stage to deliver femtosecond with high energy pulse up to mJ [78, 79]. The first OPCPA were introduced in the 1990s [80, 81]. In the long-wavelength regime, OPCPA sources have been realized in the 2 µm spectral region [82] and in the mid-IR at a central wavelength of 3.2 µm [78]. Recently, Fastlite [83] a company based in Nice (France), started to manufacture those OPCPA systems.

3.1.3 Mid-IR OPCPA

Our table-top system generates CEP stable nine optical cycles duration (FWHM), which can be further compressed down to the Fourier limit (1.35 opt. cycle) with a hollow core fiber [79] delivering high average power.

A general layout is presented in Fig. 3.2. The Er-fiber delivers two outputs with 220 mW power at a central wavelength of 1550 nm with a 100 MHz repetition rate. One of them is frequency downshifted in a crystal fiber to 1075 nm. The mid-IR seed is generated in a 1-mm-thin periodically poled lithium niobate (PPLN) crystal. It is then stretched down to 3 ps for the pre-amplifier stage. The pump is from Coherent, Inc., made out of neodymium-doped vanadate ND:YVO_4 and serves as an amplifier for the signal. It provides 1.1 mJ 9 ps pulses at a 1064 nm wavelength and 160 kHz repetition rate. In the pre-amplification section, we use a chain of 3 OPAs and in the booster section 4 rendering a total of 7 OPAs. A chirp-inverter based on Martinez-type is applied before the booster amplification to have the highest compression efficiency through a sapphire bulk. Each booster stage consists of two identical crystals, PPLN for OPA4 and OPA5, and $KNBO_3$ for OPA6 and OPA7. The residual pump from

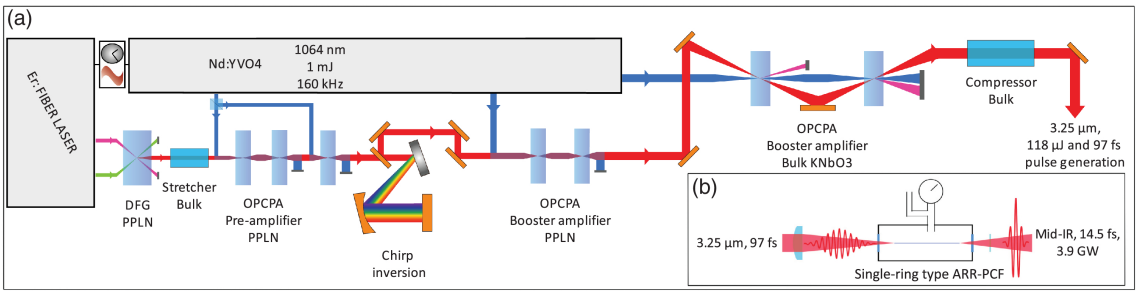

FIGURE 3.2: **Setup of the high-power, mid-IR OPCPA system. Figure and captions taken from [79]. a**. The seed is generated by a two-color fiber front-end in combination with a DFG stage. Afterwards, the mid-IR pulses are stretched and consecutively amplified in a preamplifier and two booster amplifiers. Maximum conversion efficiencies are achieved by multiple use of the pump beam and by individually tailored seed-to-pump pulse durations. The mid-IR output is compressed in a bulk stretcher and **b** the final compression to a single optical cycle is performed using an Ar-filled ARR-PCF.

OPA4 and OPA6 are recycled respectively into OPA5 and OPA7 to achieve further efficiency. The pulse energy is 77 µJ after OPA5 and 131µJ after OPA7, corresponding to an average available power of 21 W. Finally, a new designed ARR-PCF [84] fiber filled in Argon allows the pulse to be compressed further down through spectral broadening. Then, the input beam power is reduced to $\sim$ 12 W to prevent fibre damage. The final output yield 60 µJ output energy, which corresponds to a single-cycle mid-IR pulse with 9.6 W average power (see [79] for more details).

It is worth mentioning that the single-cycle pulse would undoubtedly benefit from many strong fields applications; however, we do not show it in this thesis. We use pulse duration fields of $\approx$50 fs and $\approx$100 fs in Chap. 5 and Chap. 6, respectively. The reasons behind are simply motivated by the fact that most ultrafast pulses have pulse duration between 3 to 10 opt. cyc. (FWHM), therefore, taking a pulse duration between those limits lead to more general strong fields applications. Additionally, the dispersion caused by the beam crossing our reaction microscope entrance window (CaF_2) in the single-cycle mid-IR laser fields still requires deeper investigation not presented here.

3.2 Reaction Microscope

A significant element for probing strong-field dynamics is the ability to detect the information of the initial momentum of the photoelectrons and photo-fragment ions. Ideally, this should be possible at a very high resolution, at a full 4π solid angle and in coincidence between ions and electrons. The latter allows e.g. to assign specifically selected photoelectrons to their corresponding part of the ion energy spectrum. This proves beneficial while looking at e.g. larger molecules to gain information of various possible fragmentation channels. Conventional charged particle imaging techniques such as time-of-flight (TOF) mass spectroscopy methods are able to provide excellent momentum resolution at repetition rates limited

by the clock time of the used timing electronics but only in one dimension (1D) at a small cone.

3.2.1 Working principle

A more sophisticated alternative is provided with a reaction microscope ReMi [36, 37, 85] based on cold-target recoil ion momentum spectroscopy (COLTRIMS). Here the initial momentum distribution of all charged particles is directly detected in all three dimensions (3D) with exceptionally high resolutions. The key advantage though is the possible coincidence detection where every photoelectron can be assigned to its parent ion and vice versa. This has been proven to be an essential benefit for imaging the ionization or dissociation dynamics of more complex polyatomic molecules, resulting in various reaction channels.

Our reaction microscope was built in our laboratory at ICFO in collaboration with the group of Robert Moshammer and Joachim Ullrich of the Max Planck Institut für Kernphysik (MPIK, Max Planck Institute for Nuclear Physics) in Heidelberg, now under the supervision of Thomas Pfeifer. Our experimental setup is similar to those in Heidelberg [86, 87]. We will go through the important steps of our ReMi design. In Fig. 3.3, we present an inside view of our experimental setup. For a more complete description, see also [88].

3.2.2 Supersonic cold target

An important technique to achieve high momentum resolution requires well-defined momenta of the reactive particles. At room temperature, thermal momentum in a gas-jet can be in the order of several atomic units [88]. A way to avoid such thermal effect can be achieved by cooling the gas via adiabatic expansion [89].

Our chamber has a small nozzle of diameter ∅=30 µm in which the gas goes through into a chamber with a much lower pressure $P_1 > P_0$. Eventually, the gas speed after the nozzle can exceed the speed of sound (1 Mach). The volume where the supersonic jet is formed is referred to as the zone of silence. Our entire system is based on a fourth differential pumping stage, decreasing the pressure of the gas jet progressively down to 10^{-9} mbar in the interaction chamber. Without gas load, our main chamber is maintained to ultra-high vacuum reaching 10^{-11} mbar. A sketch of the supersonic jet target is shown in Fig. 3.4. More details about the calculations and the momentum uncertainty related to the jet velocity can be found in [88].

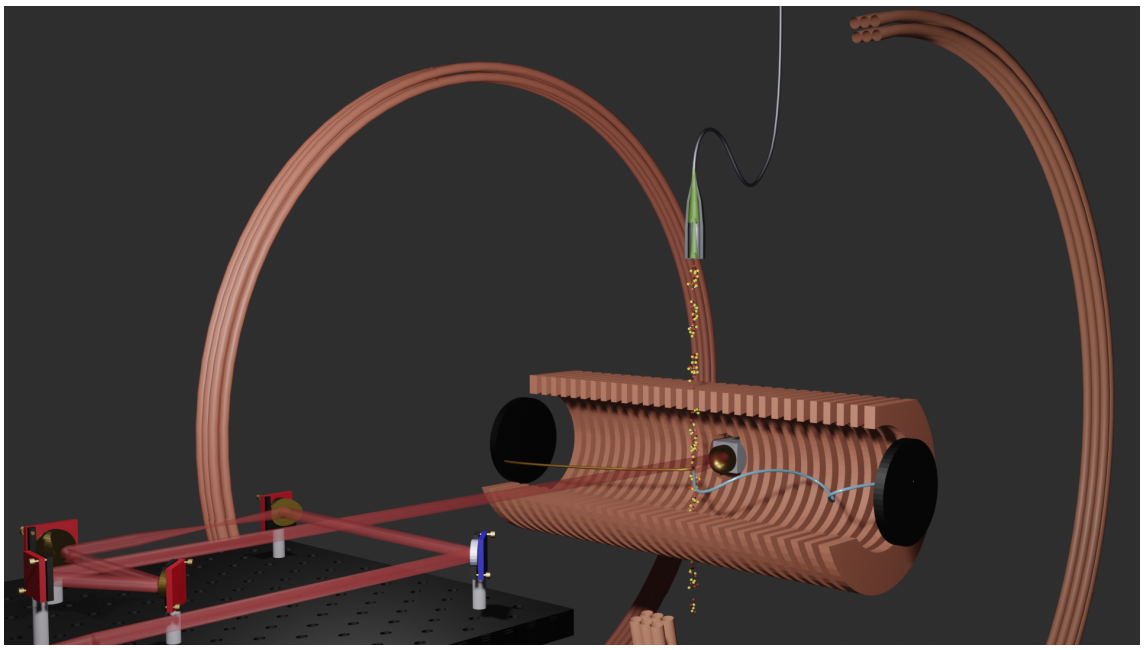

FIGURE 3.3: **Inside view of the Reaction Microscope.** We use a total of 5 mirrors (M1, M2, M3, M4 and M5) on the optical breadboard to guide the beam through the Reaction Microscope main vacuum chamber. The OPCPA 3.2 µm laser source is collimated through a pair of paraboloid mirrors (M2 and M3) having different curvature/focal points. The last three mirrors are mounted on a delay-stage to adjust the telescope length between M2 and M3. The laser beam intersects with the molecular jet (supersonically expanded, see Fig. 3.4), after focusing on a gold paraboloid mirror (M6) mounted on a XYZ-linear stage via the opposite flange. The ions and electrons are guided towards their respective charged particle detector by applying a DC voltage. A pair of Helmotz coils generate a magnetic field to confine the electrons into a cyclotron trajectory with nominal radius matching the maximal detector size ($r \approx 80$ mm).

3.2.3 Spectrometer and helmotz coils

The spectrometer consists of a stack of 34 metal electrode plates, each separated by 8 mm. A chain of 180 kΩ resistors separates the electrodes to create a homogenous electric field. At the end of the spectrometer, we use two copper wire meshes called grids to extend the electric field until the detector. This way, lensing effects are prevented thanks to the high difference potential between the spectrometer and the detector voltages. A ring between the first grid and the spectrometer ensures that the homogeneous field is not disturbed by the grounded support. In the middle of the spectrometer, a hole of 60 mm diameter allows the beam to pass through the spectrometer. A golden on-axis paraboloid mirror is mounted on an XY-stage, which lets focus tight in the gas jet reaction volume. Again, to ensure the field's homogeneity, a voltage is applied on the gold-coated surface of the mirror. A voltage divider biases all the different potentials. In total, the spectrometer length until the detector including ion and electron grids has an approximative length of 314 mm, which represents symmetric acceleration lengths of $l_a \approx 0.157$m for both ions and electrons.

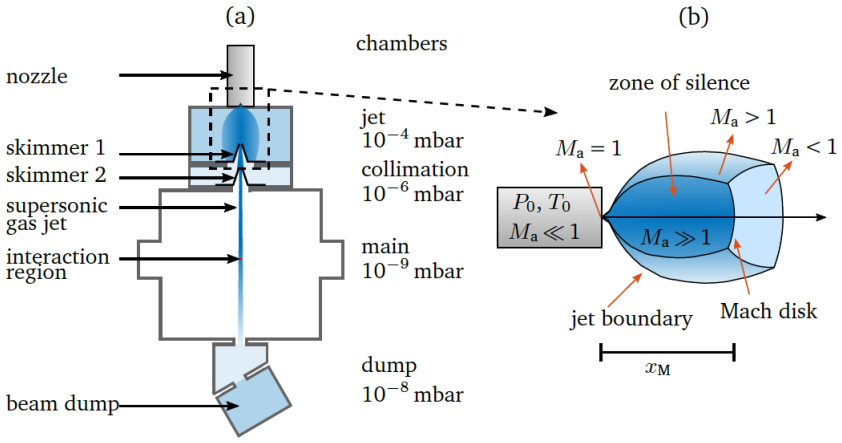

FIGURE 3.4: **Ultra-cold gas jet in high-vacuum**. Courtesy from Benjamin Wolter [88]. **a**. Free gas expansion in vacuum turning the thermal energy into kinetic energy while escaping through the nozzle. **b**. After passing through the nozzle the gas enters the zone of silence which forms a supersonic flow. Two skimmers further collimate the gas jet by removing particles with high transverse momentum.

Due to the small mass of the electrons, it is not enough to apply a voltage to guide them towards the detector. Therefore, we apply a homogeneous magnetic field to contain their trajectory in a nominal radius given by their initial momenta and the strength of the magnetic field $\mathcal{B}$. The magnetic field is generated by a pair of Helmholtz coils with a radius $R_{coils} = 700$ mm consisting in $n_{coils} = 24$ copper windings. Depending on the current I we apply in the copper coils, the strength $\mathcal{B}$ is given by

$$\mathcal{B} = (\frac{4}{5})^{3/2} \frac{\mu_0 n_{coils} I}{R_{coils}} \tag{3.2}$$

where μ_0 is the vacuum permeability. Since the current we usually plug can exceed 100 Amps, we cool down the copper coils with water flowing in order to prevent any possible damage.

The idea behind the design of the spectrometer is to keep the acceleration length of the ion relatively small such that heavy fragments or molecular breakup dissociation carrying high momenta can be recorded in the detector within a moderately high voltage of 300V. For the electrons, it is possible to add a drift length where the voltage is constant, increasing the momentum capability resolution [86, 90]. However, we decided not to add it to collect most of the scattered electrons before they have time to realize one cyclotron revolution. We will mention this later in Sec. 3.3. Finally, a high momentum resolution in the transverse direction can be achieved by rotating the laser fields polarization parallel to the detectors [20, 44, 91].

3.2.4 Position sensitive detectors

Our particle detector is made of two stacked time-sensitive multi-channel plates (MCPs) together with a position-sensitive delay-line anode. The signal serves

as timing information compared to a trigger being the detected laser pulse on a photodiode (PD). When a charged particle hits the detector, it releases electrons from the channel surface. Those electrons are accelerating by a high-voltage ($\approx$ 1 kV) to the back of the plate producing secondary electrons. In order to achieve a better amplification, the two MCPs are tilted by an angle of $\approx 8^{\circ}$ in a chevron geometry. A geometrical ratio between the channels and the inter-space gives a hit efficiency of about $\approx$50%.

$$ToF = t_{MCP} - t_{trigger} + t_0 \tag{3.3}$$

where t_0 are some global offset.

The position read-out of the signal is measured with two perpendicularly delay line anodes made of parallel wires. The time-difference detected in both ends of the delay line allows us to retrieve the position (X,Y)

$$X = v_{\perp}[(t_{x1} - t_{MCP}) - ((t_{x2} - t_{MCP})] = v_{\perp}(t_{x1} - t_{x2}) \tag{3.4}$$
$$Y = v_{\perp}[(t_{y1} - t_{MCP}) - ((t_{y2} - t_{MCP})] = v_{\perp}(t_{y1} - t_{y2}) \tag{3.5}$$

with $v_{\perp}$ the propagation speed of the electric signals in the copper wire. The sum of the associated time signals $t_{x/y,sum} = t_{x1/y1} + t_{x2/y2}$ is constant and can be used as a filter of good event in the analysis.

3.2.5 Data acquisition

The arrival times of the signals are measured using constant fraction discriminators (CFDs). The signal that hits the delay line can be seen as a centroid of the electron cloud hitting several windings of the delay line at once. The CFDs measure the central time of each signal independently of its amplitude and produce standardised NIM-signals that can be read with a time-to-digital converter. The TDC is controlled by a VME bus system that transfers the data to a PC via a MBS stream server. In total we use ten signals ($t_{x1}, t_{x2}, t_{y1}, t_{y2}, t_{MCP}$) times two for both ion and electron MCP plus a 11^{th} signal for the laser trigger which initiates the TDC read-out. The TDC has a minimum time resolution of 25 ps and a maximum readout of 52 µs. Upon a second trigger, the TDC stores all detected signal data that was previously recorded for the time window t_w set by the user. Due to the 160 kHz laser repetition rate we chose to trigger on the ion signal. Nevertheless, it is possible to switch and adjust the trigger on the electrons in the case we want to avoid coincidence filtering.

3.3 Data analysis

To facilitate the analysis from the several millions TDC events, the data processing can be done offline through an automated procedure built for reaction microscopes (see [90]). The codes use the GSI online/offline object-oriented framework go4 [92] which provides a graphical user interface and extends the ROOT C++ classes developed at CERN.

3.3.1 Go4Py

Thanks to the library PyRoot and the pythonic macros developed by Sven Augustin on newer Go4 releases, it was possible to manipulate the data contained in the TRoot histograms through Python. By checking on the option autosave on Go4 software, we create a copy of the TRoot histogram, which is refreshed within a certain delay. Since the histograms are usually pretty heavy in memory, it is definetely recommended to use an acceptable delay of 100 seconds on a regular desktop computer. Then, in the scope of my thesis, I developed a GUI through the wxPython library as presented in Fig. 3.5. With that, we have been able to give a quick and deeper analysis while conserving the Generic C++ codes initially developed by Arne Senftleben [90] during his thesis.

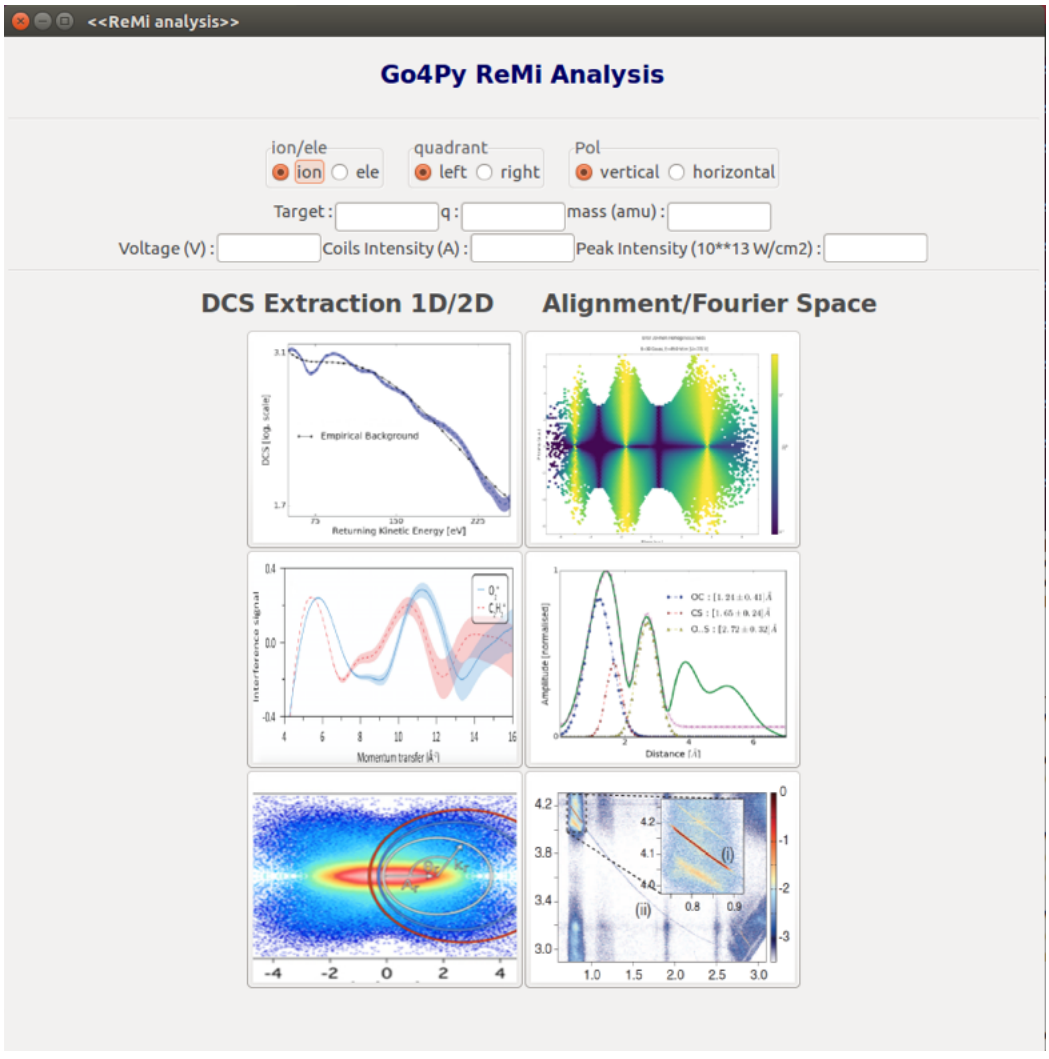

FIGURE 3.5: **Go4Py GUI.** A complementary analysis is done online, adding more flexibility on the programming language, as it is the case for that Graphical User Interface developed in Python.

3.3.2 Momentum reconstruction

As mentioned earlier, the reaction microscope is a 3D momentum imaging detector. It records the position (X,Y) on the detector, which translates into (Px,Py) momentum, plus the time-of-flight information ToF, which provides the additional momentum Pz along with the spectrometer.

$$P = \begin{pmatrix} Px \\ Py \\ Pz \end{pmatrix} \approx \begin{pmatrix} \frac{m}{ToF} X \\ \frac{m}{ToF} Y \\ a.ToF^2 + b.ToF \end{pmatrix} \tag{3.6}$$

Since both the static electric $\mathcal{E}$ and magnetic $\mathcal{B}$ fields are aligned ($\vec{\mathcal{E}} || \vec{\mathcal{B}}$) along the spectrometer axis $\vec{e_z}$, the longitudinal (Pz) and transvere momentum ($P_\perp = \sqrt{Px^2 + Py^2}$) have a simple analytical form given by the Lorentz force

$$m\ddot{\vec{r}} = q(\vec{\mathcal{E}} + \dot{\vec{r}} \times \vec{\mathcal{B}}) = q \left[\begin{pmatrix} 0 \\ 0 \\ \mathcal{E}_z \end{pmatrix} + \begin{pmatrix} \dot{x} \\ \dot{y} \\ \dot{z} \end{pmatrix} \times \begin{pmatrix} 0 \\ 0 \\ \mathcal{B}_z \end{pmatrix} \right] \tag{3.7}$$

where m is the mass and q the charge of the particle.

Integrating Eq. 3.7 along the third component $\vec{e_z}$, we obtain the acceleration length z=l_a for a given field strength $\mathcal{E}_z = \Delta U / l_a$,

$$l_a = \frac{q\Delta U}{2ml_a} ToF^2 + \frac{P_\parallel}{m} ToF \tag{3.8}$$

where ΔU is the potential difference between the intersection volume and $P_\parallel$ the initial longitudinal momentum of the charged particle. It should be taken into account that the supersonic jet is formed at the center of the chamber due to the overlap of the two skimmers. Since the beam waist of the laser after focusing on the paraboloid mirror is small $\omega_0 \approx 7\,\mu m$ compared to the jet diameter $\varnothing \approx 1.4$ mm [88], Eq. 3.8 has no offset z_0 such that the acceleration length l_a is defined by the distance from the centre of the chamber until the MCP detector. From Eq. 3.8, an analytic solution for the longitudinal momentum is given by

$$P_\parallel = \frac{-q\Delta U}{2l_a} ToF + \frac{ml_a}{ToF} \tag{3.9}$$

Due to the cyclotron motion of the electrons, the trajectory in the (X,Y) plane is confined into a radius R_c which depends on the initial transverse momentum $P_\perp$ and the cyclotron frequency ω_c

$$\omega_c = \frac{|q|\mathcal{B}_z}{m} \tag{3.10}$$

$$R_c = \frac{P_\perp}{|q|\mathcal{B}_z} = \frac{P_\perp}{\omega_c m} \tag{3.11}$$

The position (X,Y) that can be defined as a distance r from the center of the detector follows

$$r = 2R_c|\sin(\alpha/2)| \tag{3.12}$$
$$\alpha = \omega_c ToF \tag{3.13}$$

An illustration of the electron trajectory on the (X,Y) plane is shown in Fig. 3.6.

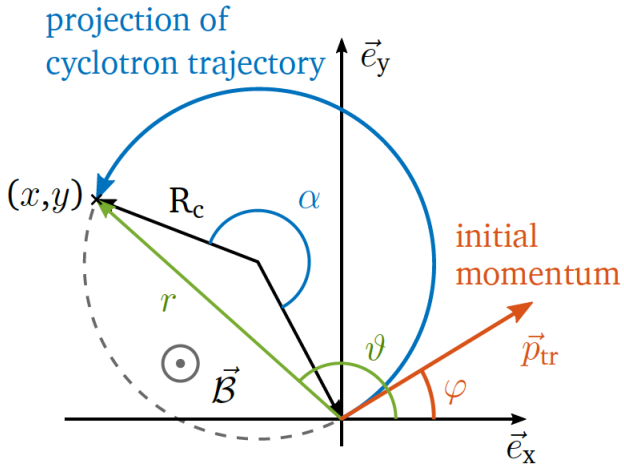

FIGURE 3.6: **Electron motion in the (X,Y) plane.** Courtesy from Benjamin Wolter [88]. Projection of the electron cyclotron trajectory onto the xy - plane of the MCP detector. The coordinate (x,y)= $|\vec{r}|$ and angle ϑ allows to reconstruct the electron initial momentum $\vec{p_{tr}}$ and angle φ, knowing the electron cyclotron frequency and its recorded ToF.

Finally, the electron transverse momentum reads

$$P_\perp = \frac{\omega_c m r}{2|\sin(\omega_c ToF)|} \tag{3.14}$$

It is possible to extract the components X and Y of the transverse momentum by calculating the emission angle.

$$\varphi = \vartheta - \frac{mod|\omega_c t|\,(2\pi)}{2} \tag{3.15}$$
$$Px = P_\perp \cos(\varphi) \tag{3.16}$$
$$Py = P_\perp \sin(\varphi) \tag{3.17}$$

However, due to the cylindrical symmetry set by our linear laser field polarization we often reduce our data analysis to 2D ($P_\parallel$,$P_\perp$).

3.3.3 Momentum conservation

An essential step is based on particle coincidence and, most importantly, momentum conservation to ensure that each detected particle truly comes from the same

event. While it sounds right to say so in the case a 100% efficiency detector would exist, practically, this task is challenging and requires long time acquisition.

Let´s illustrate an example of how it works. In Fig. 3.7 **a** we show the time-of-flight (ToF) of the electrons (Y-axis) vs the ToF of the ions (X-axis) recorded from a measurement we did on OCS molecules. Assuming two particles scatter elastically with each others, the two particles go in opposite direction given by the momentum conservation $P_{ion} + P_{ele} = 0$ which also implies that $P_{\parallel,ion} + P_{\parallel,ele} = 0$. If this condition is met, one can observe a correlation in the Tof of the electrons vs ions as indicated by the dashed lines in Fig. 3.7 **a** white for OCS^{32+} and red for OCS^{34+}. The same can apply to photoionization or fragmentation as soon as all particles involved are detected. However, it always represents a small percentage of all detected events. For example, let´s assume we have one ionization event per time window, the detection efficiency scales as $\eta = 0.5^n$, where n is the number of particles to make one event. So, in order to detect an electron with its parent ion, we have 1 chance over 4 to have a "good" event and 1 over 2 to have a "false" event. Therefore, one way to recover a "partial" coincidence for a particle pair is to filter events that arise from the same laser pulse without imposing full momentum conservation. This requires an ion count rate significantly lower than the repetition rate to assure less than one SFI event per pulse. Nevertheless, in the context of molecular ionization and fragmentation, a loosened coincidence [88, 93] is applied to ensure the elimination of electron background of other channels as shown in Fig. 3.7 **b**. In Figure 3.7 **c** the 2D photoelectron distribution (PED) is shown for all-electron detected signals and in **d** when applying a momentum sum filter on Z-axis of approximately 2 a.u. At low momentum distribution, both PED look almost similar, but when looking at processes yielding low cross-sections (i.e. $P_{//}$ >4 a.u.), you might notice a difference.

3.3.4 Resolution

One always has to balance two important features: acceptance and momentum resolution. In Fig. 3.8 we present the momentum error and acceptance of the OCS experiment detailed in Sec. 5. A complete derivation of the error calculations is given in [88]. If no magnetic fields were used, the electron longitudinal momentum error would follow Fig. 3.8 **a**. However, by applying the rule of l'Hôspital ($\mathcal{B} \to 0$) one can easily verify that an electron with initial transverse momentum of 1 a.u. won't be detected on a MCP of diameter $\varnothing_{MCP} = 80$ mm.

$$\lim_{\omega_c \to 0} P_\perp = \frac{mr}{ToF} \tag{3.18}$$

$$ToF = 30 \cdot 10^{-9} s, \quad m = 9.11 \cdot 10^{-31} kg, \quad P_\perp = 1.99 \cdot 10^{-24} kg.m.s^{-1} \tag{3.19}$$

$$r \approx 66\, mm > \frac{\varnothing_{MCP}}{2} \tag{3.20}$$

Very often, the beam's pointing after focussing on the paraboloid mirror and hitting the jet is not perfectly perpendicular with regard to the spectrometer axis.

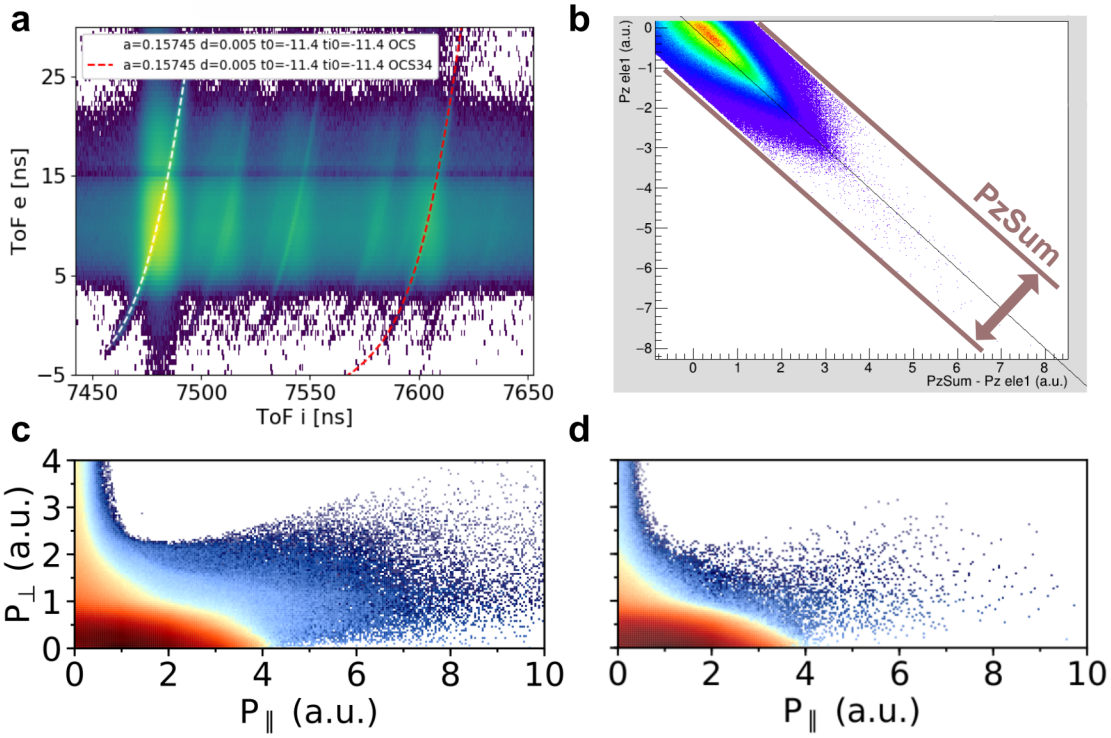

FIGURE 3.7: **Momentum conservation a**. Electron time-of-flight (ToF) vs ion ToF, also called as PePiCo. Correlated events are displayed by the white (OCS^{32+}) and red (OCS^{32+}) dashed lines. Strong horizontal and vertical signal exhibit uncorrelated "false" signal. **b**. Momentum-momentum correlation narrowed down by the momentum sum PzSum=$P_{z,ion}$+$P_{z,ele}$ width fixed to 2 a.u. **c**. Photoelectron distribution from all detected electron signal and **d** from electron signal with the momentum sum filter applied in **b**.

Therefore, a rotation of 3 or 4 degrees is applied to our software analysis to correct for the tilt of the laser polarization to the spectrometer axis. Since our detectors allow a 3D momentum reconstruction, the correction is straightforward. For the reasons indicated above, we always apply a magnetic field together with an electric field for the electron detection even if the investigation focuses on a small solid angle (e.g. recording backscattered electrons).

Due to the electron cyclotron motion, when the electron time of flight is an integer of the cyclotron period, it is impossible to reconstruct the transverse momentum $P_\perp$ as indicated in Fig. 3.8 **b** by the yellow vertical lines (nodes), also visible in Fig. 3.8 **c-d** (see the tail around $P_\parallel$=0 a.u.). As mentioned in Sec. 3.2.3, for the spectrometer design, we chose a short acceleration length for the electrons to travel until their corresponding MCP. It results in a shorter time-of-flight, allowing us to shift the first cyclotron node towards the negative longitudinal momenta within a moderately low voltage of $\approx$ 300 V. The positive electron longitudinal momenta are left with a good resolution as shown in Fig. 3.8 **b**.

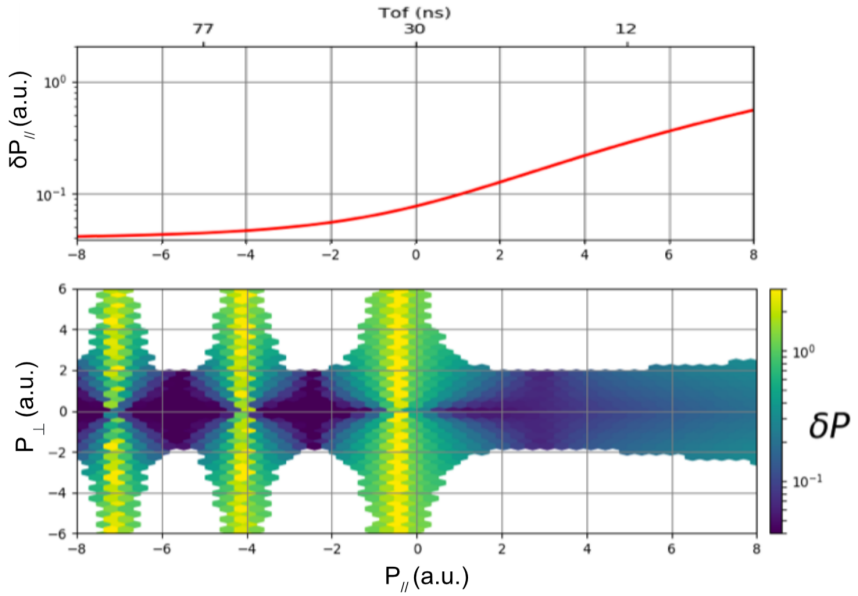

FIGURE 3.8: **Acceptance and momentum errors a**. Longitudinal momentum errors for an electric field strength $\mathcal{E} = 19.1\, V.cm^{-1}$ $P_\perp = 0$ a.u. **b**. Acceptance and resolution $\delta P(\delta P_\parallel, \delta P_\perp)$ of a 2D simulated electron total momentum distribution for an electric field strength $\mathcal{E} = 19.1\, V.cm^{-1}$ and a magnetic field strength $\mathcal{B} = 10.4\, G$. Cyclotron nodes appear in yellow (see color scale in density plot δP).

Chapter 4

Strong-fields holography

In the strong field approximation (SFA) the coulomb interaction between the ion parent and the electron is ignored, as previously mentioned in Chap. 2. When adding a coulomb potential, long-range effects such as coulomb focusing [94] are turned on. Consequently, the electrons returning closer and slower to the core are accelerated and deviate from their initial trajectory. Recent observations [66, 95, 96] show the importance of including the coulomb field in order to numerically reproduce the different "bunches" present in the low energy spectrum [97, 98, 99]. Similarly, intra-cycle interferences which paved the way for strong-fields holography [47, 100, 101, 102, 103] were correctly adjusted with the introduction of novel methods such as CCSFA [104], TCSFA [46, 105], ARM [106, 107], CQSFA [108, 109, 110, 111], QTMC [69] and SCTS [70].

Strong-fields holography techniques are powerful means to extract temporal information about the tunneling and subsequent rescattering information [47, 73, 111, 112, 113]. The latter can be found in the high kinetic energy spectrum (undergoing hard scattering) and will be covered in detail in Chap. 5 and Chap. 6. Meanwhile, we dedicate the following chapter to photoelectron interferences in the low-energy spectrum. Most importantly, we show how the interference signal can be used to probe information about the target structure without necessarily undergoing scattering with the parent ion.

4.1 Introduction to photoelectron tunneling dynamics

In strong field, electrons that rescatter against the atomic shell are drift away from the core, within an additional momentum kick given by the vector potential at the rescattering time $A_{sc} = A(t_{sc})$. Considering linearly polarized laser fields, the final photoelectron momentum p_f, given here in cylindrical coordinates $p_f(p_z, p_x)$, reads:

$$p_f = \sqrt{p_{z,f}^2 + p_{x,f}^2} \tag{4.1}$$

$$p_{z,f} = -k_{sc}\,\cos(\theta_{sc}) + A_{sc} \tag{4.2}$$

$$p_{x,f} = k_{sc}\,\sin(\theta_{sc}) \tag{4.3}$$

where θ_{sc} and k_{sc} are the rescattered angle and momentum, respectively.

For small angles θ_{sc}, the final momentum does not exceed the typical drift momentum $A_0 = \sqrt{4U_p}$, where U_p is the average energy of a free electron in the laser fields. Thus, the forward scattered electrons are confined in the low energy spectrum ($E_k < 2U_p$), together with photoelectrons that do not revisit the core and are usually referred to as "direct" electrons.

4.1.1 Coulomb quantum orbit strong-field approximation

In order to describe the electrons in the continuum, we involve the most advanced theory in terms of semi-classical treatment: Coulomb quantum orbit strong-field approximation (CQSFA [108, 109, 110, 111]). According to it, there are four types of orbits that can lead to the same final momentum p_f, and potentially interfere with each other. We illustrate all of them in Fig. 4.1 (a). Those trajectories are categorized on four "orbits" depending on their tunnel exit z_0 (see Eq. 2.23) and initial transverse momentum $p_{x,0}$ with regard to their final parallel and transverse momentum, $p_{z,f}$ and $p_{x,f}$ respectively. For the direct electrons, orbit (1) and (2), the initial and final transverse momentum have the same sign $p_{x,0}.p_{x,f} > 0$. In (2), the tunnel exit z_0 and the electron's final momentum $p_{z,f}$ have opposite direction $z_0.p_{z,f} < 0$. For the rescattered electron trajectories, orbits (3) and (4), they start with a small initial transverse momentum and consequently revisit the core with distances of closest approach r_c inferior to the tunnel barrier, even sometimes closed to the Bohr radius ($r_b = 1$). The amplitude probabilities from all trajectories, unless orbit (4), are shown in Fig. 4.1 **b**. Orbit (4) is the backscattered electrons and has low probabilities along the longitudinal momentum axis compared to the other orbits, within the investigated kinetic energy range $0 < E_k < 2U_p$ [108]. For that reason, we show calculations for orbit (1), (2), and (3) only.

According to the CQSFA [108, 109, 114] model[1], the action is computed along a two-pronged contour.

$$S = S_{tun} + S_{prop} \tag{4.4}$$

The first part of the contour describes the tunneling ionization and is taken parallel to the imaginary-time axis, going from $t_s = t_r + i\,t_i$ to t_r. During the tunneling process, the momentum p_0 is kept constant and follows the SFA action, plus an additional integral which includes the coulomb-correction during the first contour:

$$S_{tun}(\mathbf{p}, \mathbf{r}, t_s, t_r) \quad = \quad i\,t_i\,I_p - \frac{1}{2}\int_{t_s}^{t_r} (\mathbf{p_0} + \mathbf{A}(\tau))^2 d\tau - \int_{t_s - i\,\epsilon, \epsilon > 0}^{t_r} V(\mathbf{r_0}(\tau)) d\tau \tag{4.5}$$

[1] There is a choice of employing the length gauge for matching better results with TDSE, see [115] for more details

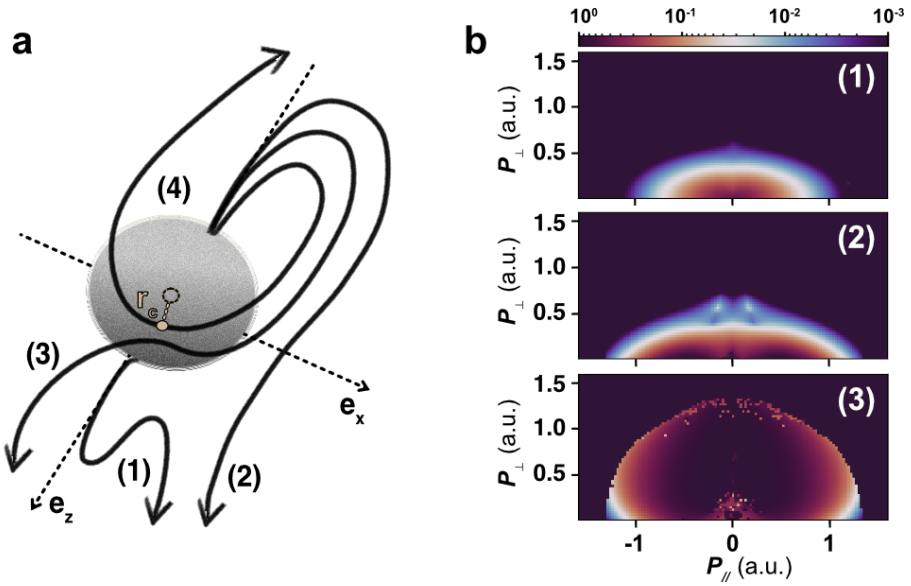

FIGURE 4.1: **Different orbits involved in CQSFA a**. For a given initial longitudinal momentum $p_{z,0}$, there are four trajectories as defined as in CQSFA [108, 109, 114] depending on the initial transverse momentum $p_{x,0}$. Trajectories (3) and (4) appear when a coulomb field is taken into account. Those trajectories revisit the core with distances of closest approach r_c (see beige dot) inferior to the tunnel exit radius (see grey sphere), which are in turn deviated from the center. **b**. Two-dimensional probability amplitudes as a function of the final longitudinal and transverse momentum $P_{\parallel}$ and $P_{\perp}$, respectively, for the trajectories (1) up to (3) (see labels in top-right corner of the figures). The calculations were done for Hydrogen atom ($I_p = 0.5$) in linearly polarized fields at an intensity of $I = 2 \cdot 10^{-14}$ W.cm^{-2} with frequency of $\omega = 0.057$ near the ionization-treshold [114]. The prefactors were not included.

Because the last term in the action is divergent at the lower boundary, a regularization procedure may follow [104, 114]. The second part describes the propagation in the continuum starting from t_r and follows:

$$S_{prop}(\mathbf{p}, \mathbf{r}, t, t_r) = t_r\, I_p - \frac{1}{2}\int_{t_r}^{t} (\mathbf{p}(\tau) + \mathbf{A}(\tau))^2 d\tau - 2\int_{t_r}^{t} V(\mathbf{r}(\tau)) d\tau \quad (4.6)$$

Note that Eq. 4.6 is a simplification due to the stationary condition,

$$\frac{(\mathbf{p}(\mathbf{t_s}) + \mathbf{A}(\mathbf{t_s}))}{2} + V(\mathbf{r}(\mathbf{t_s})) = -I_p \quad (4.7)$$

and the following saddle points:

$$\dot{\mathbf{p}} = -\nabla_r V(\mathbf{r}(\tau)) \quad (4.8)$$

$$\dot{\mathbf{r}} = \mathbf{p}(\tau) + \mathbf{A}(\tau) \quad (4.9)$$

with V(r) of the form -C/r, where C is an effective coupling $0 \leqslant C \leqslant 1$. In the case of the Hydrogen atom, C is set to 1 ($C = \sqrt{2\,I_p} = 1$).

Following [108, 109, 114], the coulomb-corrected transition amplitude reads:

$$M(\mathbf{p_f}) = -i \lim_{t\to+\infty} \sum_s \left\{ \det \left[\frac{\partial \mathbf{p_s}(t)}{\partial \mathbf{r_s}(\mathbf{t_s})} \right] \right\}^{-1/2} \mathcal{C}\left(\mathbf{t_s}\right) e^{iS(\mathbf{p_s},\mathbf{r_s},t,\mathbf{t_s})} \tag{4.10}$$

where $\mathbf{p_s}$, $\mathbf{t_s}$ and $\mathbf{r_s}$ are the saddle points. $\frac{\partial \mathbf{p_s}(t)}{\partial \mathbf{r_s}(t_s)}$ is the stability factor and can be obtained numerically considering a Legendre transformation as $\frac{\partial \mathbf{p_s}(t)}{\partial \mathbf{p_s}(t_s)}$[108, 111, 114, 116]. Special attention should be paid to the Maslov phase [63] which brings an additional phase-offset in the action when calculations are carried out in reduced-dimensionality [111, 116]. Finally, applying the saddle point approximation leads to a divergence in the calculations of the transition elements $\langle \mathbf{p} + A(t_s))|\mathcal{H}_I(t_s)|\Psi_0\rangle$ contained inside the prefactor $\mathcal{C}(t_s)$. For that reason, analytical solutions were suggested in [57] and [117].

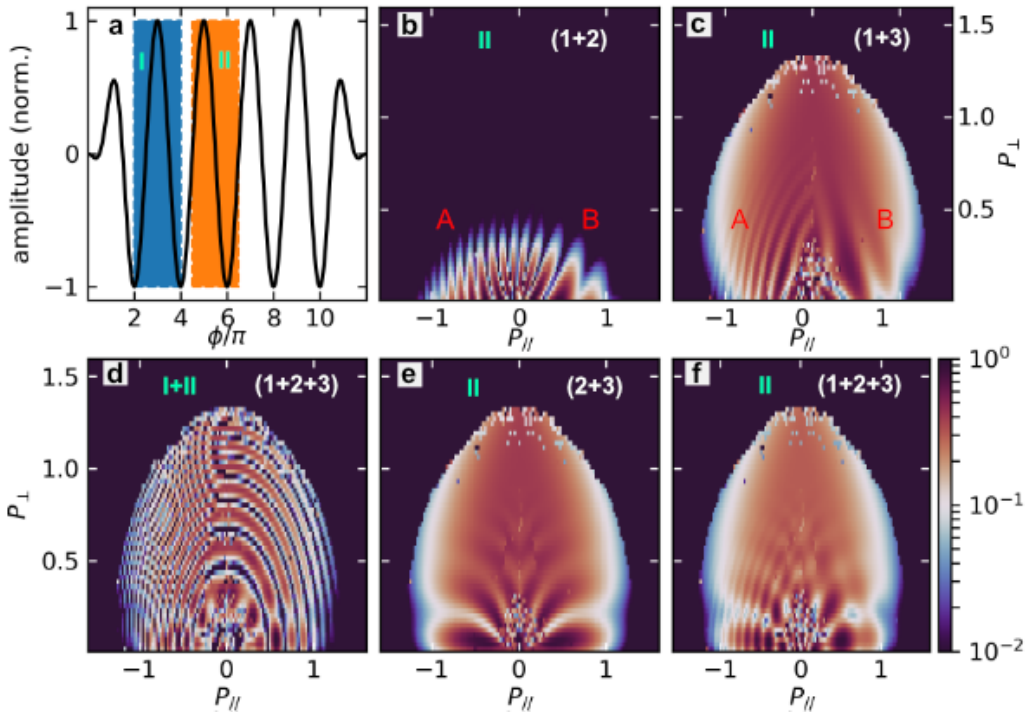

FIGURE 4.2: **Near-treshold interference pattern a**. Flat-top laser pulse with same laser parameters as in Fig. 4.1. The calculations were run for the two temporal windows highlighted by the blue and orange shaded area, labeled "I" and "II", respectively. **b**. Amplitude probabilities involving two direct photoelectrons (1) and (2) for the temporal window indicated by "II". There are two possible type of interferences if the two electrons are born within a time-delay of $\tau_{1,2} < \pi/\omega$ or $\pi/\omega < \tau_{1,2} < 2\pi/\omega$, labeled as A or B. **c**. Same as **b** but with trajectories involving orbits (1) and (3). **d**. Interference patterns from the three types of orbits (1+2+3) accumulated over the two temporal windows, "I" and "II". **e**. Same as **b** but with trajectories involving orbits (2) and (3). **f**. Same as **b** but with trajectories involving orbits (1), (2), and (3). The prefactors were not included.

In this thesis, all calculations are shown for a pulse width of 6 opt. cycles, unless mentioned elsewhere. However, since this section is dedicated to bringing a more general introduction about strong-fields holography rather than reproducing the exact experimental conditions, the calculations were done for only two opt. cyc. out of 6, as indicated in Fig. 4.2 **a** by the blue and orange shaded areas labeled as "I" and "II", respectively. Different names were attributed in the literature to the interference pattern we show in Fig. 4.2. Among them are the fanlike structure (see Fig. 4.2 **b**), the fish-bone-like structure (see Fig. 4.2 **c**) and the spider-leg structure (see Fig. 4.2 **e**). Additionally, we chose to show the interference pattern along the symmetric window "II" to reveal interferences between two photoelectrons born within time $\tau < \pi/\omega$ and $\pi/\omega < \tau < 2\pi/\omega$, labeled in Fig. 4.2 **b-c** as A and B, respectively. In Fig. 4.2 **f**, we show the interference pattern from the sum of the three types of orbit. Finally, when the complex amplitudes are summed within two consecutive opt. cycles, for example, "I" and "II" from Fig. 4.2 **a**, intercycle interferences occur as shown in Fig. 4.2 **d** by those rings.

4.1.2 Coulomb-corrected interference in the Mid-IR

We now modify the field parameters to show below-treshold ionization CQSFA calculations using our experimental laser frequency $\omega = 0.01425$ and laser peak intensity $I_0 \approx 8.0 \cdot 10^{13}\,\mathrm{W.cm^{-2}}$. Below, we show in Fig. 4.3 the photoelectron angular distribution (PAD) for the same (1), (2), and (3) orbits as presented in Fig. 4.1. For the upper panels of Fig. 4.3 **a-c** we do not include the prefactor and normalize the amplitude signal from the maximum yield found in panel **a**, while in the lower panels of Fig. 4.3 **d-f** we include the prefactor and normalize the amplitude signal from the maximum yield found in panel **d**. Then, in order to validate a trajectory with the semi-classical calculations, the final retrieved momentum at the upper boundary must have positive kinetic energy, $E_k + 1/r > 0$, following Kepler's laws [70, 118, 119]. Additionally, we should notice that the calculations were not computed starting from the edge of the pulse but for sometime later when the envelope of the fields remains constant (see the blue-dashed area in Fig. 4.2 **a**). Hence, for that two reasons, the probabilities at low momentum $P_f < 0.05$ were canceled in panels Fig. 4.3 **d-f**. Finally, it is possible to transform those calculations realized in cylindrical coordinates to 3D coordinates, accounting for the Jacobian presented in [116]. However, since we did transform our experimental PAD into cylindrical coordinates already during the data processing, as shown in Sec. 3.3, we will not apply any further transformation.

For orbit (3) (see Fig. 4.3 **f**), it leads to some irregularities in the calculation of the amplitude near $P_{\parallel} \approx 0$. This is due to the fact that there are multiple solutions, including higher-order returns. The same applies to the calculation of the determinant in Eq. 4.10. Those irregularities can be solved using a higher initial momentum in the solver and/or using higher precision in the determinant calculation. Additionally, one may compute the whole complex trajectories as shown

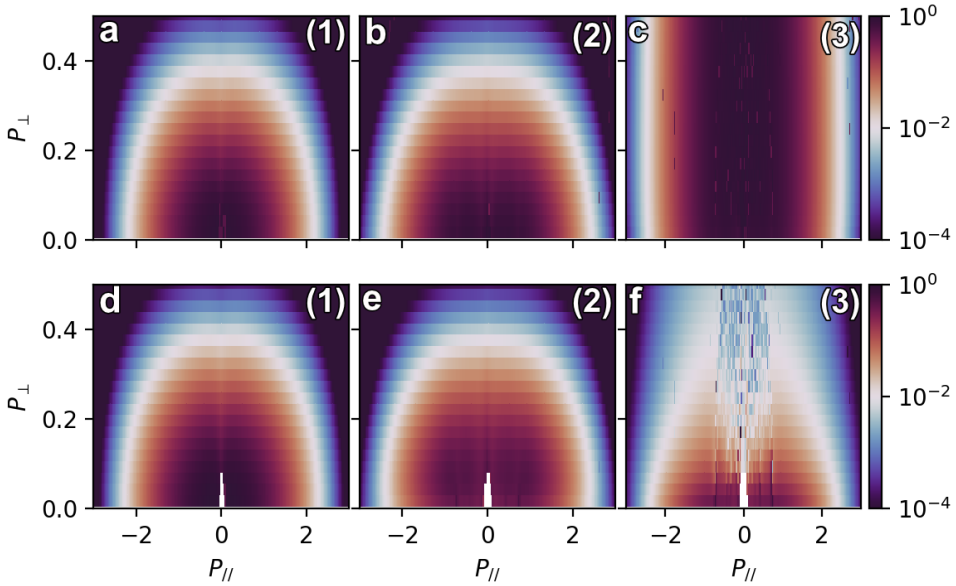

FIGURE 4.3: **Probability amplitude for orbits (1), (2) and (3). a-c**. Same calculations as shown in Fig. 4.1 but with different laser frequency $\omega = 0.01425$ and peak intensity $I_0 = \approx 8.0 \cdot 10^{13}\,\mathrm{W.cm^{-2}}$. The probability amplitudes are shown without including the prefactor and are normalized to respect to panel **a** (orbit (1)). **d-f**. Same as **a-c**, but with including the prefactor and normalized with respect to panel **d**.

in [110] and treat each branch cut individually to avoid dealing with such problems.

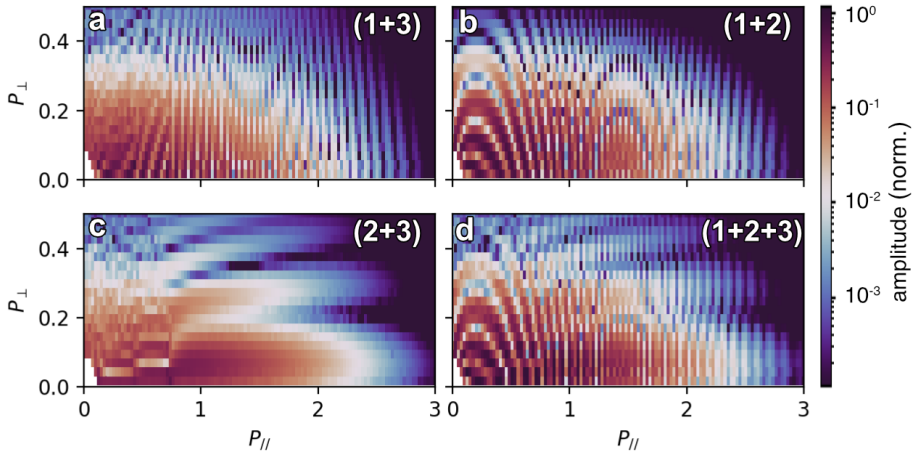

FIGURE 4.4: **Below-treshold interference pattern. a-c**. Two electron interference patterns in the Mid-IR regime. The orbits are shown in white color text in the upper-right figures. The spacing in momentum between two consecutive fringes becomes smaller as a result of a longer time-delay between two adjacent half cycles. **d**. Interference pattern from the sum of the three orbits. **a-d**. The amplitude probabilities were normalized with respect to panel **d**.

Finally, for the calculation of the action under the tunnel barrier, we use the

convenient parametrization mentioned in [114] (see supplementary materials), which allows us to enhance the visibility in the interference pattern as shown in Fig. 4.4. From the three different type of interference shown in Fig. 4.4 **a-c**, the fan structure **b** and the spider **c** seem to be the dominant ones that survive when adding together the three orbits as shown in Fig. 4.4 **d**. The spider structure has horizontal stripes and shows a dependency along the transverse momentum axis mainly, while the fan structure has vertical fringes and shows a dependency along the longitudinal momentum axis.

Since the fan-like structure is made from two electrons born from opposite sides of the target, it allows a direct measurement of the initial orbital parity. For example, the fan-like interference carries an additional π phase shift if the orbital parity is odd. That is what we are going to show experimentally in the next section. Note that both theoretical and experimental results were shown already in [120] at a laser wavelength of $\lambda_0 = 788\,\text{nm}$. Since the spacing of the fringes is smaller at our experimental wavelength ($\lambda_0 = 3200\,\text{nm}$), and the average momentum drift A_0 larger thus, we obtain a larger dynamical range for probing those tunneling ionization dynamics.

4.2 Extracting orbital parity

As presented in the previous section, the CQSFA can provide a complete analysis of the different interference patterns seen in the experiments. We saw that the interferences involving forward scattered electrons contribute less in the long-wavelength regime, leaving the direct electron interferences (fan-like) as the primary probe along the longitudinal momentum axis ($P_\perp \approx 0$).

Perhaps, in this section, we will leave the CQSFA model and opt for TDSE calculations instead, using the Qprop software [59, 72]. Indeed, depending on the level of computing resources, it can be a long and tedious task to perform semi-classical calculations for a pulse length comparable to the experimental conditions ($\tau_{exp} > 6$ opt. cyc.). Moreover, the advantage of using the TDSE relies on the fact we can set any pulse shape and potential we want, with user-functions well referred[2], but most importantly, the method is fast due to the tSurff method [52]. Recently, Tulsky and al. suggested a method to cut the TDSE in different time-slices at the Surff boundary allowing a direct "time-resolved" TDSE calculation [121].

4.2.1 Fan-like structure in the Mid-IR

In order to make calculations faster, it is often used a flat-top pulse to approximate a longer $\sin^2$ envelope pulse. In principle, a factor of two can be gained

[2] https://www.qtmps.physik.uni-rostock.de/forschung/qprop/qprop/

by shortening the pulse to the full-width-half-maximum (FWHM) of the $\sin^2$ envelope fields. Thus, in Fig. 4.5 we computed TDSE calculations from two different input pulses, top-hat (see Fig. 4.5 **a**) and $\sin^2$ (see Fig. 4.5 **d**) envelopes, linearly polarized at a central wavelength of $\omega = 0.01425$ and a peak intensity of $I_\omega = 6 \cdot 10^{13}\,\mathrm{W.cm^{-2}}$ within a pulse duration of 10 opt. cyc ($\approx$ 5 FWHM). We chose an initial $2p$ state with ionization energy $I_p = 15.8$ eV corresponding to Ar (argon) in a pseudo potential:

$$U_{\mathrm{Ar}}(r) = -\frac{1 + 17e^{-cr}}{r},\ r < R_{\mathrm{co}} \tag{4.11}$$

linearly ramped down to zero between $R_{\mathrm{co}} = 50$ and $2R_{co}$. The spatial grid and the time-step during propagation were set to $dr = 0.1$ and $dt = 0.025$, respectively.

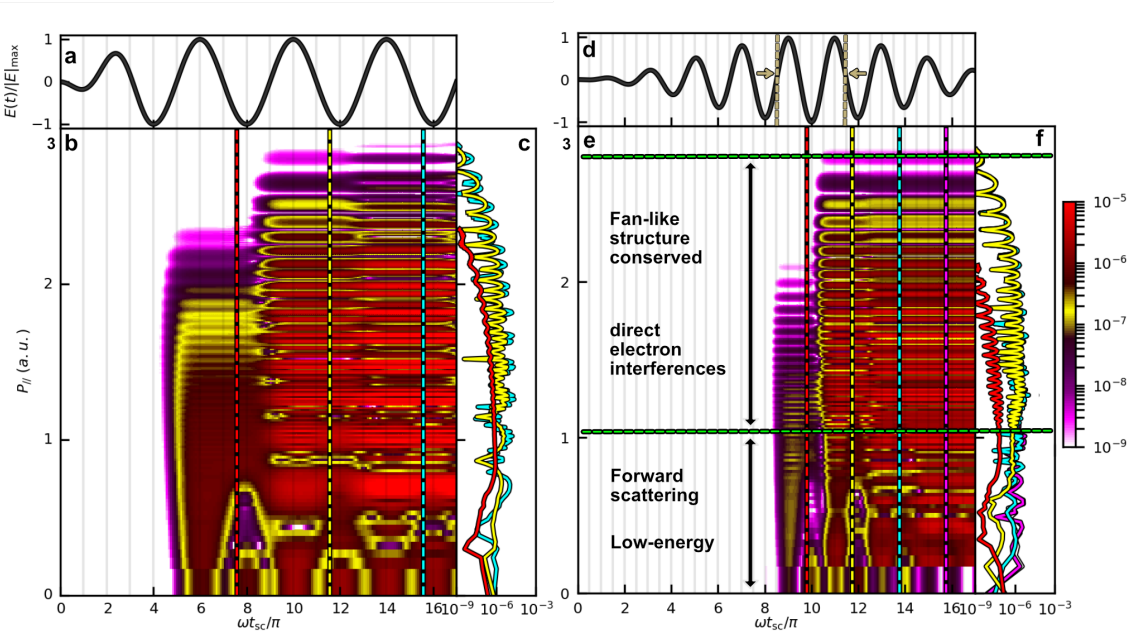

FIGURE 4.5: **Argon "time-of-flight" TDSE calculations using Qprop [121] a**. Flat-top pulse with a laser frequency of $\omega = 0.01425$ and a laser peak intensity of $I_0 \approx 6.0 \cdot 10^{13}\,\mathrm{W.cm^{-2}}$. The calculations were computed until the end of the pulse $\tau_{laser} = 10$ opt. cyc., but shown here for the four first opt. cyc. **b**. Integrated differential yield for the laser fields shown in **a**, as function of the longitudinal photoelectron momentum distribution ($P_\perp = 0$) and the rescattered phase $\omega t_{sc}/\pi$ (or birth phase for direct electrons). See text for more details. **c**. 1D slices for the integrated yield taken at different rescattered phase $\omega t_{sc}/\pi$ as indicated by the dashed-lines in **b**. **d-f**. Same as in **a-c** but for a $\sin^2$ envelope fields and a pulse duration of 10 opt. cyc.

Fig. 4.5 **b** and Fig. 4.5 **e** were performed with the recent "time-of-flight" analysis introduced in [121]. That same analysis will be shown later in more detail in Chap. 5 which was developed initially by Vasili Tulsky in collaboration with Prof. Dieter Bauer from the Rostock University. Shortly, a time differential yield describing the electrons arriving at the surface with a certain time t_0 can be obtained by applying a gaussian window to the time-dependent surface flux

method (tSURFF) [52].

$$\partial_t \tilde{a}_k(t_0) = \int_0^T e^{-\frac{(t'-t_0)^2}{2t_w^2}} \partial_t a_k(t') \frac{dt'}{\sqrt{2\pi t_w^2}} \tag{4.12}$$

In all calculations presented here, and later in chap. 5, we use the same width filter $\omega t_w = 0.2\pi$. Hence, the TDSE-yield can be sorted as shown in Fig. 4.5 by integrating Eq. 4.12 from 0 until an upper limit which can be defined as the registration time t_0

$$\Delta Y(k,T) = \left| \int_0^{t_0} \int_0^T e^{-\frac{(t'-t_0)^2}{2t_w^2}} \partial_t a_k(t') \frac{dt'}{\sqrt{2\pi t_w^2}} dt_0' \right|^2 \tag{4.13}$$

Finally, one can propagate the trajectory back in time until it reaches the origin for a certain time that we will label scattering time t_{sc}.

$$R_{surff} = \int_{t_{sc}}^{t_0} A(t')dt' + k(t_0 - t_{sc}) \tag{4.14}$$

It should be noticed that the last equation represents a crude approximation for direct electrons that are slowly escaping from the target and which would lead to a certain time offset in the estimation of t_{sc}. However, it might be true for a certain region of the photoelectron momentum distribution, but in any case it will affect our interpretation here since we want to show the integrated yields from well apart separated time ($\approx$ 1 opt. cyc.).

Looking at Fig. 4.5, we can identify the fan-like interferences responsible for the visible oscillations in the integrated yield. In the case of the flat-top pulses (see Fig. 4.5 **a**), the intercycle interferences add up both constructively and destructively from one cycle to another. Consequently, the signal keeps growing with an additional phase as well as the spacing between the fringes becomes smaller and smaller. This is shown for example, by the cyan and yellow lines in Fig. 4.5 **c** which is the integrated yield taken at a different time as illustrated by the dashed lines in Fig. 4.5 **b**. In the opposite, for a $\sin^2$ envelope (see Fig. 4.5 **d**), the yield mainly sum up from those times indicated by the red and yellow lines in Fig. 4.5 **f**. As we can see, the integrated yield taken at times corresponding to the cyan and purple dashed lines in Fig. 4.5 **e**, have the same offset as the yellow line in Fig. 4.5 **f** for the area delimited by the green horizontal dashed lines. Within this momentum range, the fan-like interferences are generated by nearly two opt. cyc. as indicated by the beige arrows in Fig. 4.5 **d**. This is a great finding since the fan-like structure is not further split into n-th multiple fringes corresponding as n-many optical cycles. By analyzing the photoelectron momentum distribution this way, as shown in Fig. 4.5, one may find a fairly approximated flat-top pulse, reproducing the yields in the investigated energy range. Here, it would be $\approx$ 2 opt. cyc. (ramping time not included) for the investigation of direct electrons. Finally, it should be pointed out that within the same method, one could remove the intercycle interferences (if the integration in Eq. 4.13 is done by

taking the modulus of Eq. 4.12, see [121] for more details), therefore showing a time-resolved TDSE subcycle interferences.

Next, we turn our investigation to show the effect on the fan interferences as we change the binding energy I_p in the ground state. For this, we used a shorter pulse width corresponding to τ_{laser} =6 opt. cyc $\sin^2$ envelope fields. Then, we computed TDSE calculations for different atomic properties as listed in table 4.1. We chose an initial 2p orbital for Ar, Kr, and Ne. The screening potential (see Eq. 4.11) is set such that the target energy in its ground state corresponds to the orbital ionization potential I_p. For the hyrdogen atom, the potential follows $1/r$, and the initial wavefunction is 1s.

Atomic properties			
Target atoms	I_p (eV)	Orbital	Parity
H	13.6	1s	even
Kr	14.0	2p	odd
Ar	15.8	2p	odd
Ne	21.6	2p	odd

TABLE 4.1: List of the atomic properties used in the TDSE calculations presented in Fig. 4.6

The photoelectron momentum distribution is shown in Fig. 4.6 **a** for all 4 targets. The interference signal is extracted by fitting a linear regression as shown by the black dashed lines in Fig. 4.6 **a**. The modulation $I_s = I_{total}/I_{fit} - 1$ is plotted in Fig. 4.6 **b**. The period Δp grows linearly with the longitudinal momentum $P_{\parallel}$. The interference from two electrons having similar ionization amplitude ($Im[\Delta S_{1,2}] \to 0$) is given by the difference in the real part of the action ($Re\,[\Delta S_{1,2}]$),

$$I(P_{\parallel}) \propto \left|e^{iS_1} + e^{iS_2}\right|^2 \tag{4.15}$$

$$\propto \left|e^{iS_1} \cdot (1 + e^{i(S_2 - S_1)})\right|^2 \tag{4.16}$$

$$\propto e^{-2Im[S_1]} \left|1 + e^{i\Delta S_{1,2}}\right|^2 \tag{4.17}$$

$$\propto \lim_{Im[\Delta S_{1,2}] \to 0} \cos^2(Re[\Delta S_{1,2}]/2) \tag{4.18}$$

which verifies [122].

Therefore, we can express the fan-like interference fringes as an interferogram of the form:

$$I(P_{\parallel}) \propto \cos^2(\Phi(P_{\parallel})/2) \tag{4.19}$$

$$\propto \cos^2(\frac{P_{\parallel}\pi}{x_1} + n\frac{\pi}{2}) \tag{4.20}$$

where x_1 is the parameter to fit and $n = 0, 1$ depending on the orbital parity even ($n = 0$) or odd ($n = 1$). In Fig. 4.6 **c-f**, we show the oscillated signal with their corresponding fit taken at different photoelectron momentum range $P_{\parallel}$ for Kr (panel **c**), H (panel **d**), Ne (panel **e**) and Ar (panel **f**). Finally, we report the phase $\Phi(P_{\parallel})$ as shown in Fig. 4.6 **g**, where a phase offset was applied to all 4 results to show $\Phi(P_{\parallel})$ in the $[0-1]\pi$ range. It results that Kr and H phases are always shifted by π, while Ar and Ne phases sometimes overlap with H phase. This was shown in Fig. 4.6 **a** already (see $P_{\parallel} > 2$). Thus, the fan structure seems to be influenced by the binding energy. Surprisingly, in the long-wavelength regime, the ionization potential I_p is small compared to the ponderomotive energy U_p. However, we show here that the binding forces (conditioned by the ground state energy) clearly influence the fan structure.

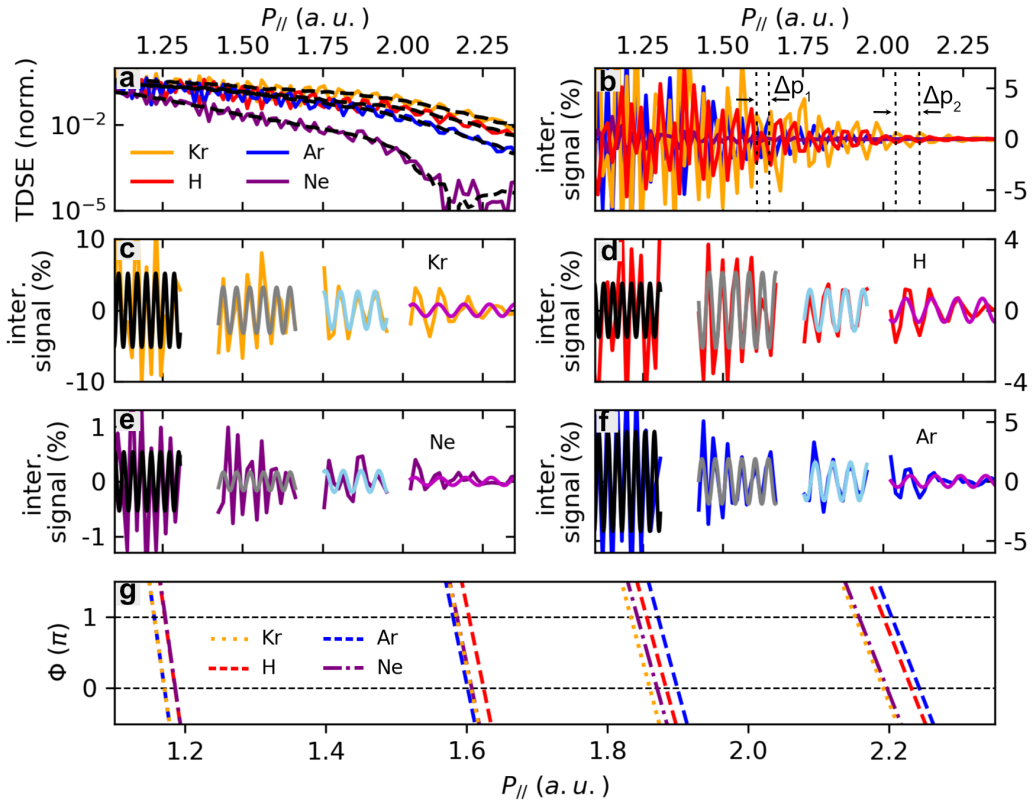

FIGURE 4.6: **TDSE calculations for Kr, Ar, H and Ne. a**. TDSE longitudinal momentum distribution $P_{\parallel}$ ($P_{\perp} = 0$) for the different atoms listed in tab. 4.1. The laser pulse duration is $\tau_{laser} = 6$ opt. cyc., while the laser peak intensity and laser frequency are kept the same as in Fig. 4.5. **b**. Interference signal extracted with a linear regression fit from panel **a**. The spacing between fringes is larger at higher $P_{\parallel}$ values. **c-f**. Interference signal fit for different momentum range intervals. **g**. Phase offset ϕ/π obtained from Eq. 4.19. An additional offset was used to show ϕ/π in the $[0-2]\pi$ interval.

Hence, the target potential must be taken into account in the calculations, even in the long-wavelength regime where the classical trajectory calculations overlap

well with the SFA predictions (see Fig. 2.2 in Chap.2). Nevertheless, when the two targets have similar binding energy I_p, they display a clear π phase-shift in their interference signal, as it will be shown next for Ar ($I_p \approx 15.8$ eV) and N_2 ($I_p \approx 15.6$ eV), or Ar and H_2 ($I_p \approx 15.4$ eV) as it will be introduced in the later section using a combined two-color laser field.

4.2.2 Ar vs N_2 experimental results

The longer the wavelength, the longer it spans the time between two adjacents half-cycle of the laser fields. Consequently, the two photoelectrons that interfere are born within a longer time-delay, resulting in a smaller spacing in momentum between successive fringes. Using our Mid-IR laser wavelength $\lambda_0 = 3.2\,\mu$m, we can probe those interferences over a large number of periods, narrowing further down the resolution on the initial phase offset given by the ground state orbital parity. Indeed, combining Mid-IR laser fields and our Reaction-Microscope detection capability, we can obtain meV resolution [38, 66]. In Fig. 4.7, we show the 2D photoelectron momentum distribution obtained at very low electric and magnetic extraction field [38, 66, 123]. As indicated by the black dashed-line at $P_{\parallel} = 1.1$ in Fig. 4.7 **a-b**, the spectra shows a local minimum for Ar (see panel **a**), while it shows a maximum for N_2 (see panel **b**). We apply those same linear regression fits than the ones showed in Fig. 4.6 **a** for Fig. 4.7 panels **a** and **b** within the intermediate photoelectron momentum range [0.9-1.5] a.u. The results are shown in Fig. 4.7 **c** for Ar (gray) and N_2 (blue), together with the experimental longitudinal momentum errors. The oscillations are clearly shifted by a π-phase as illustrated by the two fits corresponding to even (black) and odd (golden) parity.

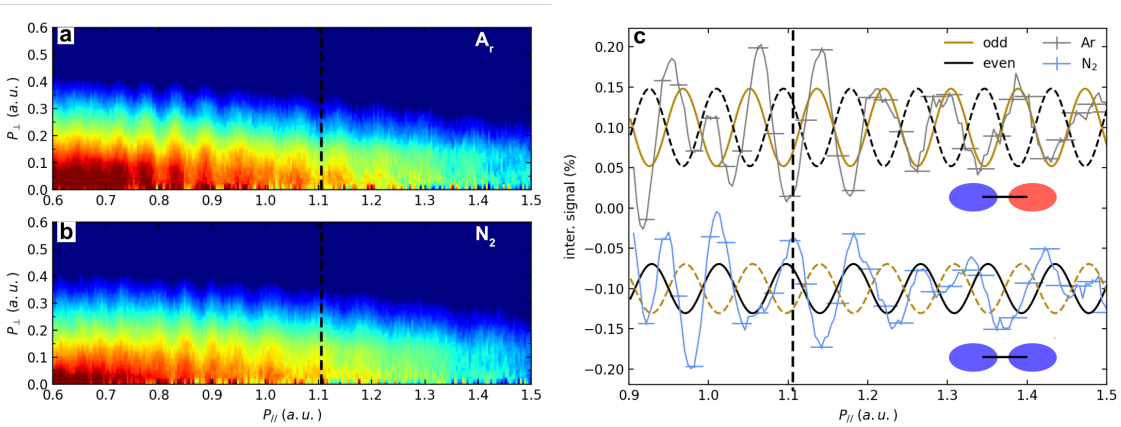

FIGURE 4.7: **Ar and N_2 fan-like interference.** **a-b**. Experimental two-dimensional photoelectron momentum distribution, longitudinal $P_{\parallel}$ and transverse $P_{\perp}$ with respect to the laser polarization axis. The visible fringes are shifted by π between Ar (**a**) and N_2 (**b**) as indicated by the black dashed line. **c**. slice cut through $P\perp \approx 0$ for Ar (gray) and N_2 (blue). The horizontal errors are given by the longitudinal detected momentum error measured with an extracted voltage and magnetic field of 18.8V and 4.4G respectively [38, 123]. The oscillations fit well even(odd) orbital parity for Ar(N_2).

It is worth mentioning the possibility to reconstruct the birth time between the two electrons as demonstrated in [73, 122] with the help of semi-classical calculations. We could make it possible employing the same analysis as presented in Sec. 4.1. However, that goes behind the scope of this thesis as it requires additional time to match both experimental and theoretical calculations. Instead, we come up in the next section with an experimental methodology to subtract the fan-like interference in a two-color laser field.

4.3 Application on two-color holography

In this section, we show those same fan-like interferences as in Sec. 4.2 but with a collinear two-color laser fields application similar to [122]. Now, the electric fields $E_{\omega/2\omega}$ and vector potential $A_{\omega/2\omega}$ vary as we change the phase-delay $\phi_{\omega/2\omega}$ between the fundamental and the second harmonic fields, whose frequency is twice greater ($\omega_{harm.} = 2\omega_0$).

$$E_{\omega/2\omega} = -E_0 \left[\cos(\omega t) + \sqrt{\frac{I_{2\omega}}{I_\omega}} \cos(2\omega t + \phi_{\omega/2\omega}) \right] \tag{4.21}$$

$$A_{\omega/2\omega} = q \int E_{\omega/2\omega}\, dt = \frac{-q.E_0}{\omega} \left[\sin(\omega t) + \frac{1}{2}\sqrt{\frac{I_{2\omega}}{I_\omega}} \sin(2\omega t + \phi_{\omega/2\omega}) \right] \tag{4.22}$$

where q is the electric charge, and $\frac{I_{2\omega}}{I_\omega}$ the intensity ratio between the two fields.

4.3.1 Experimental calibration

As a result of the change in $\phi_{\omega/2\omega}$, it enhances the ionization probability in different areas of the two-dimensional photoelectron momentum distribution (PMD) as shown in Fig. 4.8 **a-b**. Applying a FFT on the 2D PMD and extracting the phase information (see Fig. 4.8 **c-d**) allows one to accurately retrieve the momentum with zero kinetic energy ($P_{\parallel} = 0$, $P_{\perp} = 0$) and calibrate further the PMD within meV precision. Here, we would like to emphasize the distinction between the relative phase $\phi_{\omega/2\omega}$ and the retrieving phase ϕ (FFT), which is also referred to in the literature as the phase of the phase [15]. Then, we should stress that the discontinuity we see in the PMD around $P_{\parallel} = -1.0$ is due to the cyclotron node (see Sec.3.3) and will not affect the signal for the investigation of intermediate momentum values $|P_{\parallel}| > 1.5$.

4.3.2 Development of an empirical method for the extraction of the fan-like interference

Since varying $\phi_{\omega/2\omega}$ makes the combined two-color fields asymmetric with respect to orbit (1) and (2) ionization windows, we first have to figure out what are the effects of $A_{\omega/2\omega}$ on the fan-like structure as a function of the relative phase

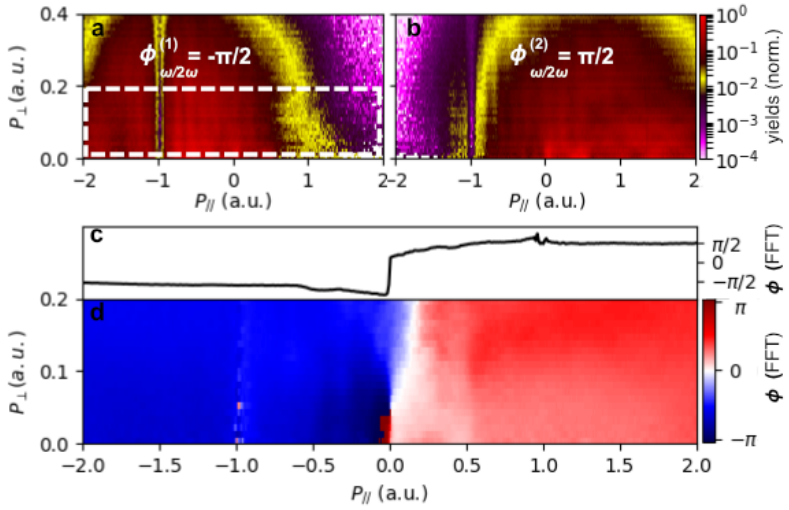

FIGURE 4.8: **Phase information from Ar PMD in two-color fields a**. Photoelectron momentum distribution (PMD) for a combined two-color fields at a relative phase $\phi_{\omega/2\omega} = -\pi/2$ following those laser parameters: $I_\omega = 6.0\,10^{13}$ W.cm^{-2}, $\sqrt{\frac{I_{2\omega}}{I_\omega}}$=0.13, $\omega = 0.01425$, $\tau_{pulse} = 10$ opt. cyc.. **b**. Same as in **a** but at a phase-delay $\phi_{\omega/2\omega} = \pi/2$. Both PMD were normalized showing a dynamical range of 4 orders. **c**-**d**. Phase retrieval information from the white-dashed square area as indicated in **a**. A one dimensional cut through $P_\perp = 0$ is shown in **c**. An abrupt change in the sign of the retrieving phase ϕ (FFT) is found for $P_\parallel = 0$.

$\phi_{\omega/2\omega}$. To that end, we compute CQSFA fan-like interference for one given optical cycle in two-color combined fields. The results are shown in Fig. 4.9 **a**, where the interference signal between orbits (1) and (2) are given as function of $\phi_{\omega/2\omega}$. The interference signal in Fig. 4.9 **b-c** is shown as "red" for positive and "blue" for negative values after being subtracted by the linear regression fit as indicated by the black dashed lines in Fig. 4.9 **a**.

At first glance, the oscillations are all shifted from one to another phase-delay ϕ/π (see Fig. 4.9 **b**). Interestingly, it is possible to adjust those interference and eventually match the same zero-crossing between all phases (see Fig. 4.9 **c**) for a given longitudinal momentum range by shifting $P_\parallel$ in a similar way as the vector potential $A_{\omega/2\omega}$ dependency. Taking our reference signal to $\phi_{\omega/2\omega} = 0.0$, where the fields are found symmetric for solutions (1) and (2), we can process Fig. 4.9 **b** and find a match between all interference signal once adding the following $\omega/2\omega$ dependency to $P_\parallel$:

$$P^1_{//} = P^0_{//} + x_0 \frac{E_0}{2\omega}\sqrt{\frac{I_{2\omega}}{I_\omega}}\sin(\phi_{\omega/2\omega}) \tag{4.23}$$

where x_0 is the factor to fit and was found equal to $x_0 = 0.39$.

4.3.3 Two-color fan-like strutcure in Ar and H_2

We now turn to the experiment and apply that same methodology to repeat the fan-like structure extraction for each phase as N independent measurements,

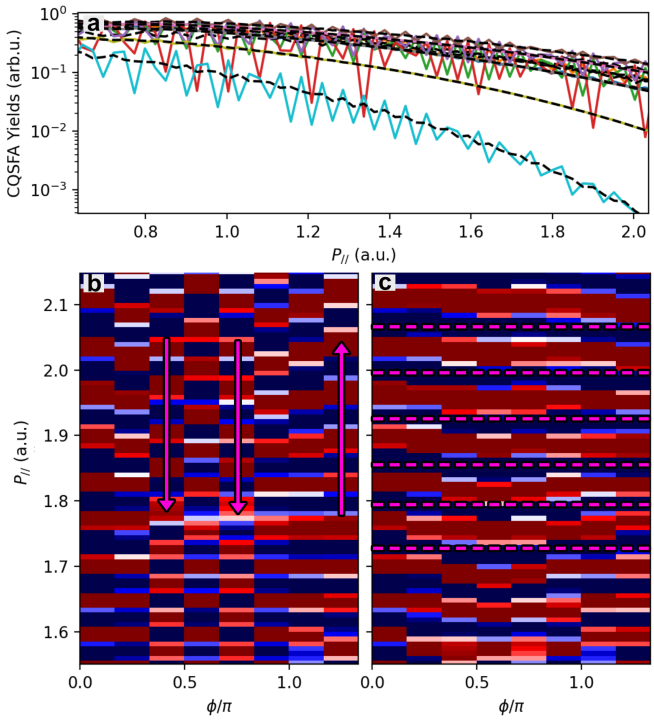

FIGURE 4.9: **Fan-like interference calculations in a collinear two-color fields a**. CQSFA calculations for Hydrogen atom computed for 1 opt. cyc. and with laser field parameters matching the experiment (see Fig. 4.8). The probability amplitudes were computed for 8 different phases $\phi_{\omega/2\omega} = [0.0 - 1.33]\pi$. **b**. The oscillated signal from panel **a** was extracted with a linear regression fit as indicated by the balck dashed line. Once subtracted, the interference is normalized and shown as ´red´ for ´positive´ and ´blue´for ´negative´ values. Then, the oscillations are fit using the reference signal $\phi_{\omega/2\omega} = 0$ and Eq. 4.23. Since Eq. 4.23 follows same dependency as $A_{\omega/2\omega}$, the interference signal is shifted downwards for phases $\phi = [0 - 1]\pi$ and upwards for $\phi = [1 - 2]\pi$ during the transformation as shown by the magenta arrows. **c**. After processing **b**, the interference signal from all phases can be recovered to match the reference phase $\phi/\pi = 0$ as indicated by the magenta dashed lines highlighting the minima.

where N is the number of scans we realized $\phi_{\omega/2\omega} = \phi_{0,\omega/2\omega} + Nd\phi_{\omega/2\omega}$. The experimental results are shown in Fig. 4.10 for Ar (see panel **a**) and H_2 (see panel **b**). We realized the H_2 measurement afterward and performed a scan with a three-time greater resolution in the phase-delay $\phi_{\omega/2\omega}$. We will dedicate the last part of this section to it. From Fig. 4.8, we have been able to calibrate both $\phi_{\omega/2\omega}$ and $P_{||}$. Within this calibration, we still see an asymmetry in both PMD. We can explain the asymmetry to come from the following reasons. The first can be explained in terms of detected momentum resolution as it can be significantly different for the negative and positive longitudinal detected momentum as shown in Fig. 3.8. Then, the second factor may arise from the global CEP phase of the laser fields ϕ_{CEP} which can still play a role for a 10 opt. cyc. pulse duration as displayed in Fig. 4.5 **d**. For the first reason mentioned above, we chose to study the interference signal coming from the negative detected photoelectron longitudinal momentum where the resolution is better.

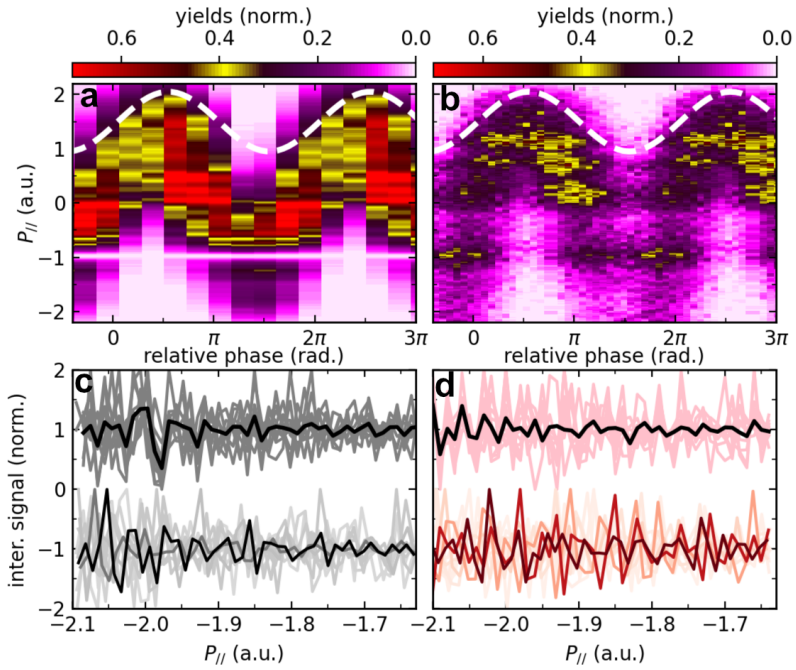

FIGURE 4.10: **Empirical method for extracting the fan-like interference in a collinear two-color fields. a-b**. Measured photoelectron spectra along the laser polarization direction for Ar and H_2, respectively, as a function of the relative phase $\phi_{\omega/2\omega}$. The white-dashed lines follow the $\omega/2\omega$ dependency. **c-d**. Raw (top) and processed signal (bottom) taken from panels **a** and **b**, respectively, at phases $\phi_{\omega/2\omega} \in [0-2]\pi$. Dark colors reflect lowest residuals with regard to the averaged signal.

The unprocessed interference signal is shown in the top part of Fig. 4.10 **c** for Ar and **d** for H_2. Each modulated signal is normalized to its maximum contrast in order to enhance their differences. After applying the same transformation as illustrated in Fig. 4.9 **b-c**, we obtain the interference signal as shown in bottom part of Fig. 4.10 **c-d**, where dark colors indicate lowest residuals with regard to the averaged signal. Then, each individual signal is fit with Eq. 4.19 as shown in Fig. 4.11 **a** for one particular phase. The zero-crossing (or roots) from all interference signal are displayed in Fig. 4.11 **b** as a probability density. Ar (gray) and H_2 (red) interference exhibit a π phase shift as shown in Fig. 4.11 **a**, where minima from the gray line overlap with maxima from the red line. Consequently, the position of the zero-crossing for Ar coincide with those shown for H_2 as displayed in Fig. 4.11 **b**. For a better visualization, we shifted Ar results by an arbitrary offset. Finally, we chose the resolution to match half of the detected longitudinal momentum error (bin size = $\Delta P_{\parallel}/2$). Considering above criteria and the N independent measurements, we can reconstruct Ar and H_2 interference signal as shown in the top inset of Fig. 4.11 **b**.

Additionally, we should mention that the spacing in momentum over one period in Fig. 4.11 **a** is about $p_0 \approx 0.041$, while it was about twice that value for a single-color field as shown in Fig. 4.7. We confirm those same findings from our

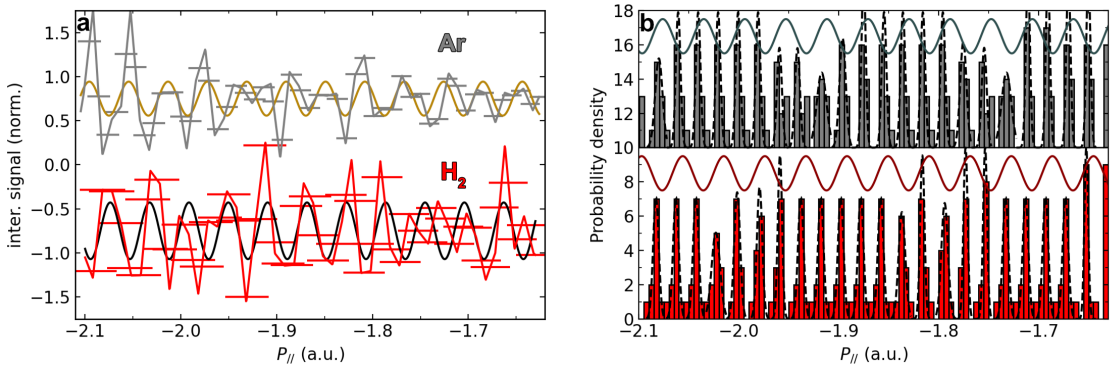

FIGURE 4.11: **Fan-like interference reconstruction for Ar and H_2. a**. Ar (gray) and H_2 (red) fan-like interference taken at one arbitrary phase $\phi_{\omega/2\omega}$ together shown with their fits, corresponding to odd (golden) and even (black) parity, respectively. **b**. Zero-crossing histograms for the N several $\phi_{\omega/2\omega}$ input data taken in the $[0-2]\pi$ interval range. Then, we apply a gaussian fit to extract the position of the zero-crossings in the longitudinal momentum range interval $P_{\parallel} \in [-2.1, -1.65]$ which allows us to reconstruct the fan-like structure of Ar as shown in the top (Ar), bottom (H_2) insets.

TDSE calculations as shown in Fig. 4.6 and Fig. 4.5, which displayed a similar spacing of $p_0 \sim 0.04$. In the single-color field measurement, the peak intensity was slightly lower $I_0 = \approx 4.0 \cdot 10^{13}$ W.cm^{-2} in [38, 123], but most importantly, the pulse duration was about $\tau_{pulse} = 6-7$ FWHM opt. cyc. which is 1-2 FHWM opt. cyc. longer than the two-color experiment presented above. Thus, we believe that the oscillations shown in Fig. 4.7 reflect the behavior of an envelope of subdivided fringes, which would explain why the period is found twice larger than Fig. 4.11 **a**.

4.3.4 Towards higher $\phi_{\omega/2\omega}$ resolution?

In that final part, we study the effects on the number of points we used for $\phi_{\omega/2\omega}$ and, most importantly, its resolution $d\phi_{\omega/2\omega}$. Previously, we chose $N = 10$ phases over one optical cycle. Now, we want to use twice the amount of input data and see the effects on the reconstructed signal. In Fig. 4.12 **a**, we show the same histogram as in Fig. 4.11 **b** for $N = 10$ (red) plus the novel analysis for $N = 20$ (purple). In the end, we report a difference of only $d\theta = 0.05\pi$ in the reconstructed signal as shown in Fig. 4.12 **b** showing the robustness of the empirical method introduced above.

Thus, we extended the results presented on Sec. 4.2 with the application of a collinear combined two-color field. Since we modulate the ionization yields as a function of $\phi_{\omega/2\omega}$, it influences the visibility of the fan interference in a given intermediate momentum range. By taking approximately 10 points over one opt. cyc., we found that it is enough for having converging results within a precision of $d\theta = 0.05\pi$, as indicated by Fig. 4.12 **b**. Moreover, we developed an empirical model which implies non *a priori* knowledge, removing the additional complexity

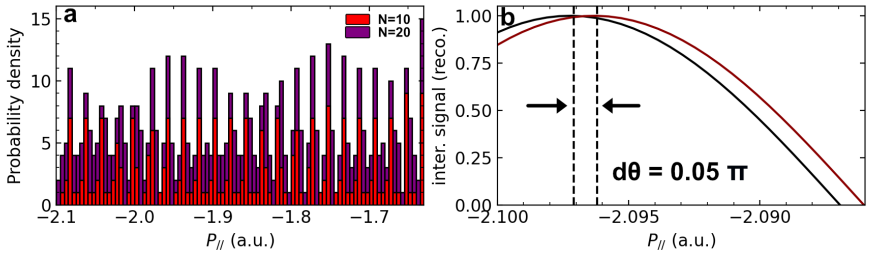

FIGURE 4.12: **Testing the convergence of the experimental methodology. a**. Probability density histograms for the zero-crossing points extracted with N=10 (red) and N=20 (purple) input phases $\phi_{\omega/2\omega} \in [0-2]\pi$. **b**. Reconstructed fan-like structure for N=10 (red) and N=20 (black). A difference of only $d\theta = 0.05\pi$ is found between the two curves.

on the actual value of the vector potential $A_{\omega/2\omega}$. Indeed, the measured uncertainties one could obtain with the present method are only based on the detected momentum error.

$$\epsilon = dP_{\parallel} + dA_{\omega/2\omega} \tag{4.24}$$

$$\epsilon = dP_{\parallel} + d(\frac{A_0}{2}\frac{I_\omega}{I_{2\omega}}\sin(\phi_{\omega/2\omega})) \tag{4.25}$$

$$\epsilon = dP_{\parallel} + \cancel{d(\frac{A_0}{2}\frac{I_\omega}{I_{2\omega}})\sin(\phi_{\omega/2\omega})} + \cancel{\frac{A_0}{2}\frac{I_\omega}{I_{2\omega}}\cos(\phi_{\omega/2\omega})d\phi_{\omega/2\omega}} \tag{4.26}$$

4.4 Outlook

In this chapter, we have presented an application on strong field holography applied to two-color laser fields. Using "direct" electrons born from opposite sides of the target, we have been able to reconstruct the phase of their interference signal, revealing information on the target orbital. Using long-wavelengths ($\lambda_0 = 3200\,\text{nm}$) together with the Reaction Microscope (ReMi), we show those interferences over 7-10 periods in the low intermediate longitudinal momentum range $1.0 < P_{\parallel} < 2.0$. Experimentally, we show that it is possible to extract the phase difference between two targets having the same binding energy within a precision of ≈ 100 mrad. However, without additional calculations or target calibration, we cannot conclude on the orbital parity since the fan-like interference patterns closely relate to the ionization potential I_p, as shown in Sec. 4.2.

Since crossing between different excited states sometimes involves a few eV, the method presented in this chapter could be used to probe orbital parity in complex systems, notably with the help of an additional pump to populate excited states. Then, it would be interesting to combine both multiphoton and tunneling regimes similar to [124] to characterize the ionization potential of the target system and its fan structure. Eventually, other types of interferences involving

scattering electrons such as carpets interference [125] may reveal complementary information about non-symmetric coulomb potentials or enantio-sensitive isomers [126].

Chapter 5

LIED Temporal dynamics

While Laser-Induced Electron Diffraction (LIED) has been successful in observing ultrafast dynamics within a fraction of a laser period [19, 44, 91, 127, 128], the attoseconds temporal dynamics of the method itself remained questionable. Indeed, the photoelectron spectrum is determined by the coherent sum of amplitudes for all the pathways that lead to a photoelectron with a certain final momentum. The fewer pathways contribute, the simpler and the less unambiguous is the mapping between photoelectron spectrum and target structure. Previous studies [42, 129] show that the differential scattering cross-sections could be approximated as field-free if they are extracted at a given fixed energy, also known as the quantitative rescattering (QRS) model. However, it is not mentioned elsewhere that the kinetic energy would correspond to the temporal information of one single versus multiple returns.

In the previous chapter, we showed the capabilities of strong-fields holography techniques to probe tunneling dynamics. We could think of a similar method to extract information about rescattering dynamcis. However, we face a fundamental property that the two electrons must be born at timescales relatively small from one another to experimentally measure their fringes spacing in momentum (scaling as $\approx \frac{1}{\delta t}$). Additionally, intra-cycle interferences cannot help understanding better the role of multiple-order returning electrons from strong fields measurements. Instead, a pump-probe method was suggested to enhance the relative ionization pathways and thus tag their different contribution in the final 2D photoelectron momentum distributions [15]. In Fact, the first experiment in the multiphoton regime using that same method was carried out almost 30 years ago and observed a forward/backward scattering asymmetry [130]. In order to add/suppress ionization probabilities in the final momentum distribution the pump frequency can be chosen twice larger the frequency of the IR probe fields as well as the ratio intensity between the two fields shall be sufficiently small such that the combined fields do not alter the electron wavepacket dynamics once launched in the continuum [73, 131], as if it would be a perturbation of the probe only.

In this chapter, we present a similar ($\omega/2\omega$) pump-probe measurement to the one mentioned above [15, 131] to gate the dominating rescattering pathways occuring in the long-wavelength regime. First, we compare two-color MIR laser fields with another two-color NIR laser fields to contrast their different complex dynamics in Sec. 5.1. Thanks to a novel method "short time filtering" combined

with the time-dependent schrödinger equation (TDSE) [121], we are able to explain the main rescattering dynamics observed in both measurements as it will be shown in Sec. 5.2. By adjusting the relative phase delay of the ω and the 2ω components of the two-color fields, we show in Sec. 5.2.2 an applicable range for LIED in the "single recollision picture" where the temporal information can be accurately retrieved. Finally the Mid-IR (MIR) two-color initiated results are put into perspective in Sec. 5.4.

5.1 Sub-femtoseconds time-resolved photoelectron rescattering dynamics

The first experiment within the HICONO network led to the Near-IR (NIR) results presented in Sec. 5.1.3, which was jointly conducted at the Weizmann Institute under Prof. Nirit Dudovich supervision, who published several works on two-color high harmonic and photoelectron interferometry [73, 132, 133, 134, 135, 136, 137]. The goal of this measurement is to extract temporal information on the backscattering photoelectron mechanisms leading to high kinetic energy $2\,U_p < E_k < 10\,U_p$, and illustrated in Fig. 5.1. Another measurement was realized at ICFO to contrast the previous NIR results with MIR laser driving fields. In Sec. 5.1.1, we detail the experimental conditions and intensity calibration of the NIR experiment, while in Sec. 5.1.2, we present the experimental details of the MIR measurement. Then, we contrast these results in Sec. 5.1.3 together with theoretical calculations developed by Vasili Tulsky from the Rostock University and supervised by Prof. Dieter Bauer.

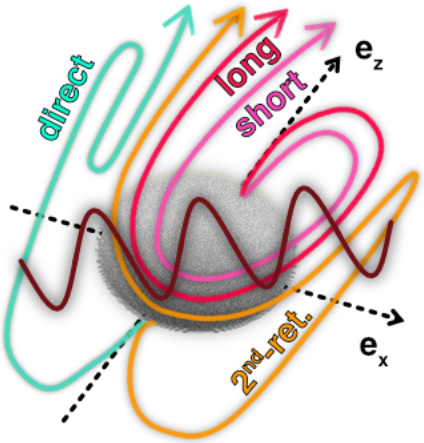

FIGURE 5.1: **Main backscattered orbits contributing to the high energy plateau.** Backscattered orbits can be of two types "long" (red) and "short" (pink). On the other hand, the electrons can oscillate many time around their parent ion before actually scattered by the coulomb potential. For simplification, we only draw the second-order return (orange). Additional trajectories that do not scatter are the "direct" photoelectrons (cyan).

5.1.1 NIR experimental protocol

The NIR measurement was carried out using a 1 kHz Ti:Sapphire amplifier with a 788 nm central wavelength and a pulse duration of approximately 30 fs (FWHM). The second harmonic 2ω field was produced using a BBO crystal with a $\lambda/4$ plate placed right after to adjust the field polarizations. The group velocity walk-off between the 788 nm and 394 nm fields was compensated using a birefringent crystal (calcite) and fused silica glass wedges. Subsequently, we controlled the relative two-color phase $\phi_{\omega/2\omega}$ by translation of the wedges and focused the combined fields with a 37.5 cm focal length on-axis parabolic mirror into a Argon pulsed gas jet (Parker-Hannifin). The emitted photoelectrons were detected in a velocity-map-imaging (VMI) spectrometer. The backing pressure and valve opening times were carefully controlled in gated mode in order to avoid a large plasma defocusing.

We performed two scans with slightly different peak intensity of the fundamental ω fields to characterize the ponderomotive energy U_p and thus the keldysh parameter γ. In Fig. 5.2 we show the two scans calibration. In the multiphoton ionization regime ($\gamma \approx 1$), above threshold ionization (ATI) can be used to calibrate carefully the momentum axes. The ATI leads in successive peaks of energies $E_n + U_p = n\hbar\omega + I_p$ [138], where I_p is the target ionization potential[1]. When extracting the pixels of two consecutive peaks given by the energy difference of $\Delta E = \hbar\omega$ as shown in Fig. 5.2 **a**, one can retrieve the momentum/pixel "a" as follows:

$$\begin{aligned} \hbar\omega &= \frac{p_2^2}{2} - \frac{p_1^2}{2} \\ &= \frac{a^2 X_2^2}{2} - \frac{a^2 X_1^2}{2} \end{aligned} \tag{5.1}$$

$$a = \sqrt{\frac{2\hbar\omega}{(X_2^2 - X_1^2)}} \tag{5.2}$$

where X_1 and X_2 are the pixels of the respective momentum p_1 and p_2 corresponding to two consecutive ATI peaks. In Fig. 5.2 **b**, we retrieve the parameter "a" for each of the two scans measured at different dates and with different VMI extractor voltages. After calibrating the data, we find a ponderomotive energy difference between the two scans of $\delta U_p = 0.98 \pm 0.1eV$ as shown in Fig. 5.2 **c** which leads to a different maximal cutoff energy $10\,U_p$ translated into a maximal momentum as reported in Fig. 5.2 **d**.

The results presented in Sec. 5.1.3 in the NIR are taken from the scan with the highest peak intensity represented by the black line in Fig. 5.2. At this peak intensity we measured a ponderomotive energy of $U_p = 2.9 \pm 0.1$eV leading to a keldysh parameter $\gamma = 1.64 \pm 0.03$, thus far inside the multiphoton regime $\gamma > 1$.

[1] different from the intercycle interferences mentioned in Chap. 4

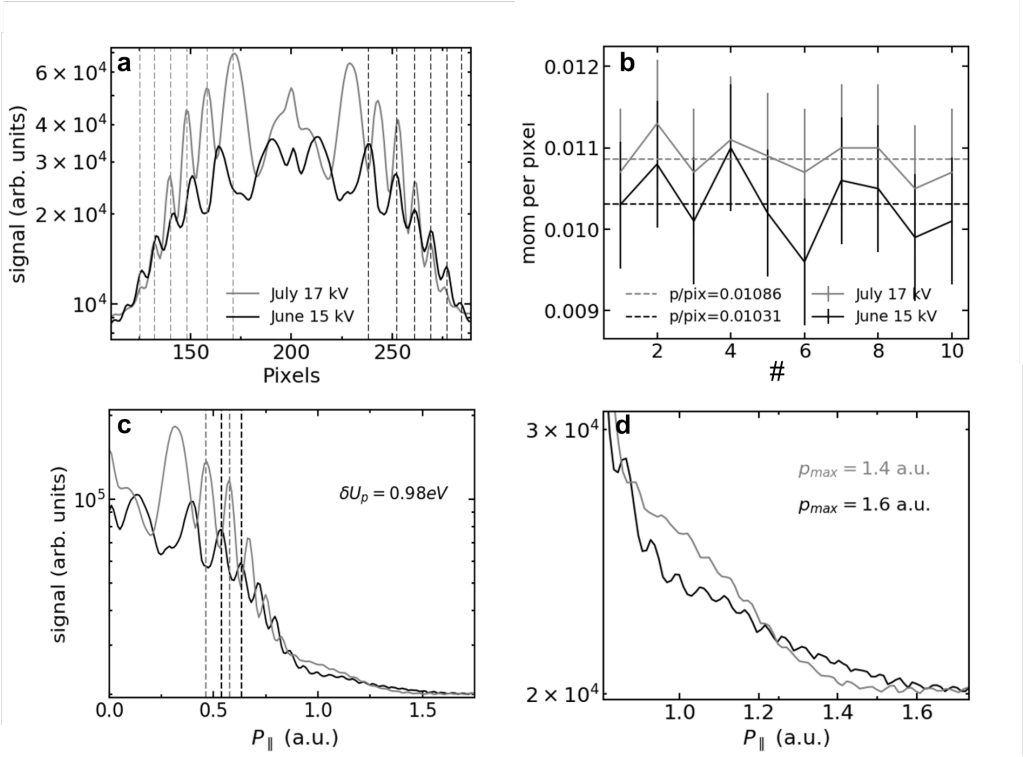

FIGURE 5.2: **Momentum calibration of two scans with slightly different VMI extractor voltages 15kV (black line) and 17kV (grey line). a**. Photoelectron momentum distribution along the laser polarization as function of the VMI Pixels. Dashed lines indicate the presence of ATI peaks. **b**. Calibration of the momentum unit per pixels for each two consecutives ATI peaks found in **c**. Calibrated longitudinal momentum distribution. A difference of $\delta U_p = 0.98$eV is found between the two sets of data. **d**. Zoom in the rescattering plateau. The highest intensity measurement (black line) has a more linear response.

5.1.2 MIR experimental protocol

Similar to the NIR experiment, the combined two-color driving field was produced and controlled using a $AgGaSe_2$ crystal, $\lambda/4$ plate, and CaF_2 wedges. For the measurement, we use our 160 kHz OPCPA [79, 139] to deliver a pulse duration of approximately 50 fs (FWHM) at a central wavelength of 3.2 µm. The fields were focused into a free flowing gas jet with a 5 cm focal length on axis parabolic mirror, and the 3D momentum distribution was detected using our reaction microscope. To guide the electrons towards the detector we use an electric field of 11.1 $V.cm^{-1}$ and a magnetic strength of approximately 6 G.

In order to account for the intensity fluctuations and the time integration recorded in each data set, we normalized the electron yields by fitting the rate of Ar^+ ions with the Perelomov-Popov-Terent'ev (PPT) formula [140] in the tunneling limit (also known as ADK formula, see, *e.g.*, [141]). The normalization procedure is shown in Fig. 5.3 and shall follow: **1.** rebinning the 2D raw data **2.** subtracting the noise level (depending on the choice of the resolution, see **1**). **3.** applying the cylindrical Jacobian that accounts for the 3D detection transformed

to the 2D frame in **1**, and **4.** normalizing by the ion yields. The subtraction of the noise becomes an important step when we squash a lot the transverse momentum resolution. Indeed, when we look at the backscattered raw data with a high resolution and a thin slice along $P_\perp = 0$ we can see that the noise oscillates at very low counts (e.g. 1 to 2 hits). However, when we integrate the backscattered yields along a cut of 0 to 1.25 a.u. in the transverse momentum axis, we see that an average yield over all the phases (see colored lines in Fig. 5.3 **a**) would be sitting somewhere in between 20 to 60 counts. We can explain the behavior of the noise in our experiment since we didn't apply a coincidence gate between the Argon ions and the rescattered electrons due to low-statistics reasons, as well as we did not aim to study a particular system. Moreover, we didn't find other signatures than Argon due to the ultracold and high Ar gas purity. Thus, we set the noise level as the bottom limit of 20 counts (see black dashed-line in Fig. 5.3 **a**). Then, we normalize by the ion yields obtained from the PPT fit (see Fig. 5.3 **c**) and apply the Jacobian $1/P_\perp$ to the raw data subtracted by the noise level (see Fig. 5.3 **c**). The normalized backscattered yields as function of the relative phase $\phi_{\omega/2\omega}$ is displayed in Fig. 5.3 **d**, where one can see the direct electrons energy cutoff delimited by the red color density oscillating as function of $\phi_{\omega/2\omega}$ (see black dashed line in Fig. 5.3 **d**). Finally, one can estimate the amplitude of the second harmonic by extracting the maximum and minimum momentum of the direct electrons cutoff.

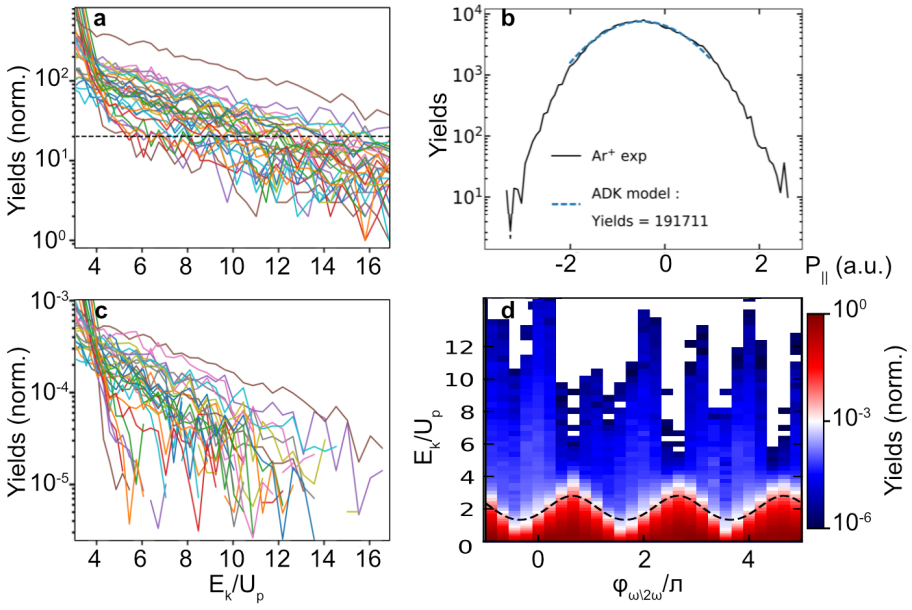

FIGURE 5.3: **Normalization procedure of the photoelectron distribution measured in the MIR fields. a**. Sliced of the 2D raw data within $0 < P_\perp < 1.25$ *a.u.*. The backscattering photoelectron distribution for each relative phase $\phi_{\omega/2\omega}$ (colored lines) is subtracted by an average offset of 20 counts (black dashed-lines). **b**. PPT fit (blue dashed-line) of the backscattered Ar^+ signal (black line) at a given phase-delay. **c**. Backscattered yields after normalization for each relative phase $\phi_{\omega/2\omega}$ as function of the electron kinetic energy. **d**. 2-Dimensional backscattered dependency as function of the electron kinetic energy and the relative phase $\phi_{\omega/2\omega}$.

In both experiments, we find a second harmonic conversion intensity of about 13% the fundamental pulses within a peak intensity of $6 \cdot 10^{13}\,\mathrm{W/cm^2}$ and $5 \cdot 10^{13}\,\mathrm{W/cm^2}$ at central wavelengths of 3.2 µm and 788 nm, respectively.

5.1.3 Emergence and control of quantum dynamics

Figures 5.4 **a** and 5.4 **b** show the measured photoelectron spectra for MIR and NIR along the polarization direction as a function of the kinetic energy and the relative two color phase $\phi_{\omega/2\omega}$. For both wavelengths, the photoelectron yield strongly depends on the relative two color phase, the direct electrons dominate in the low-energy region $E_k \simeq 0 - 4U_\mathrm{p}$ (as shown in Chap. 4), and the highest attainable energy oscillates as a function of $\phi_{\omega/2\omega}$. In comparison with the NIR results where the changes as a function of $\phi_{\omega/2\omega}$ are smoother and less abrupt, the MIR case suffers more from the limited dynamical range in the experiment. Indeed, the relative phase delays in the MIR were limited to 9 points per optical cycles (over 2π). We favored the statistics and the reproducibility of the data by scanning 3 opt. cycles instead of taking more points within one optical cycle. The NIR results match with those observed in [142].

In order to obtain insight into the origin of these abrupt changes in the highest attainable electron energies at MIR wavelength, we compare the experimental results with respective TDSE calculations [72] in Figs. 5.4 **c** and 5.4 **d** . For the MIR case in Fig. 5.4 **c** we confirm the abrupt changes in the highest cut-off energies at $\phi_{\omega/2\omega} \simeq 0.5\pi, 2.5\pi, 4.5\pi, \ldots$. In the NIR case Fig. 5.4 **d** such abrupt changes are absent although a strong modulation of the cut-off energy is also observed. The observed cut-off energies can be explained by considering electrons that scatter on the parent ion during the first or the second return. In the single-color case, these trajectories are known to lead to $10U_\mathrm{p}$ and $7U_\mathrm{p}$ cut-offs, respectively [56, 143]. In the two-color case, these cut-offs are modified, depending on the intensity of the second-harmonic field. The cut-offs, as a function of $\phi_{\omega/2\omega}$, are indicated in Fig. 5.4 **c** around $\phi_{\omega/2\omega} \simeq 0.6\pi$ where rescattering is suppressed altogether and the cut-off jumps from large for $\phi_{\omega/2\omega} \lesssim 0.6\pi$ to small for $\phi_{\omega/2\omega} \gtrsim 0.6\pi$. They match very well with the TDSE result. In next section, we will show how a small change in the relative-phase delay swaps the dominant contribution to the spectrum completely from first-return scattering to second-return scattering electrons.

5.2 Identifying the main rescattering dynamics

A deeper insight into the rescattering dynamics is obtained by calculating time-resolved energy spectra using the time-dependent surface flux approach [52, 144]. In that way one can register when electrons of a certain energy pass the surface of a sufficiently large sphere around the target. With this information one can then calculate the times t_sc of the last scattering at the parent ion by propagating classical electrons backwards in time [121].

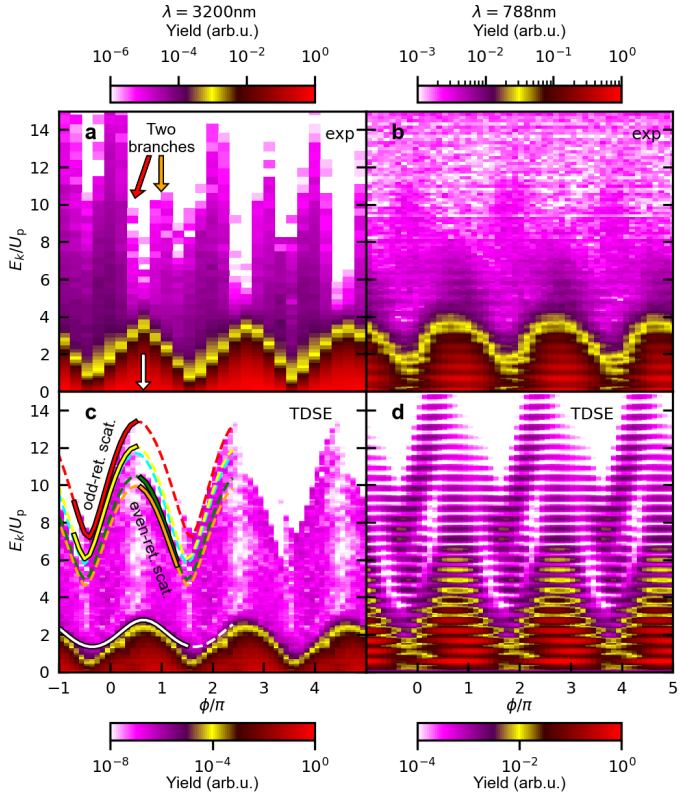

FIGURE 5.4: **Phase-dependent photoelectron yields in the MIR and NIR. a,b**, Measured photoelectron spectra along the laser polarization direction for MIR and NIR, respectively, as a function of the relative phase $\phi_{\omega/2\omega}$. The respective TDSE calculations are shown in **c,d**. The energy axes are scaled in units of the ponderomotive energy U_p of the strong ω component. Laser parameters: (**a,c**) $\lambda = 3.2\,\mu m$ at $I_\omega = 6 \cdot 10^{13}\,W/cm^2$ ($U_p = 57.3\,eV$), (**b,d**) $\lambda = 788\,nm$ at $I_\omega = 5 \cdot 10^{13}\,W/cm^2$ ($U_p = 2.9\,eV$), in all cases $I_{2\omega} = 0.13 I_\omega$. In **a** the two high-energy backscattering branches in the spectra are indicated by colored arrows, and the $\phi_{\omega/2\omega} = 0.65\pi$ phase delay where rescattering is most strongly suppressed is indicated by the white arrow. In **c**, the cut-off energies predicted from classical electron trajectories are plotted as colored lines: first- (red line) and second- (orange line), third- (yellow line) and fourth-return (green line) backscattered at high energies, and direct electrons (white line) at low energies.

5.2.1 Emergence of semi-classical electron trajectories

The resulting time-resolved formation of the photoelectron yield for two values of $\phi_{\omega/2\omega}$ is illustrated in Fig. 5.5. From the distinct temporal jumps in the photoelectron yield for energies $\gtrsim 2U_p$ we infer that the dominating contributions to the final spectrum originate from well defined scattering times. These retrieved scattering times coincide with the classically predicted ones (also shown in Fig. 5.4, which is indicative of the tunneling regime).

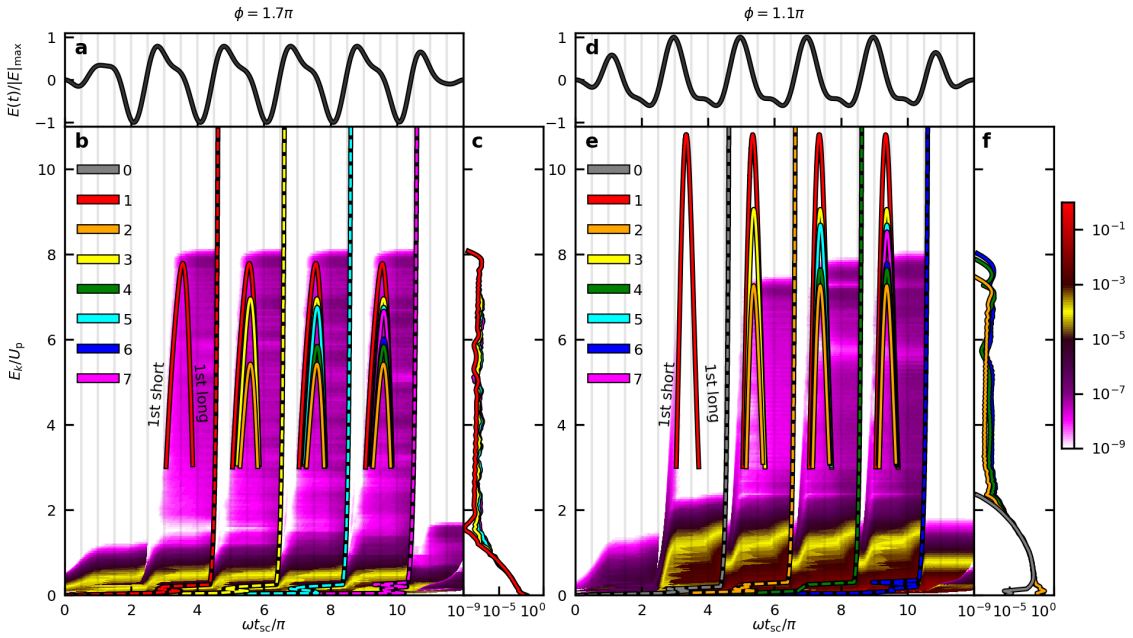

FIGURE 5.5: **Time-resolved formation of the photoelectron yield.** The shape of the laser pulse is shown in **a**. Laser parameters: $\lambda = 3.2\,\mu m$ at $I_\omega = 6 \cdot 10^{13}\,W/cm^2$ (frequency ω), and $I_{2\omega} = 0.13 I_\omega$, $\phi_{\omega/2\omega} = 1.7\pi$. **b** Build-up of the photoelectron spectrum by electrons that rescatter at time t_{sc}. The signal is collected for each optical cycle separately and thus nullified when reaching the times indicated by dashed vertical lines. In **c**, the spectra at these times are shown in the respective color. The classically predicted time instants $t_{sc}(E_k)$ are included in **b** as solid lines with colors indicating the number of returns (see legend, 0 means no scattering, 1 indicates scattering upon first return, 2 upon second return, etc...). In **d–f** the same as in **a–c** is shown but for the relative phase $\phi_{\omega/2\omega} = 1.1\pi$. Odd-order returns are then suppressed and even-order returns dominate the spectrum.

The second-harmonic field serves as a sub-cycle gate that suppresses or enhances the ionization probability and thus the contribution of certain electron trajectories. For the particular values of $\phi_{\omega/2\omega} = 1.1\pi$ and $\phi_{\omega/2\omega} = 1.7\pi$, the respective photoelectron spectra have nearly equal high-energy cut-off (see Figs. 5.4 **c**) while originating from different types of trajectories. For $\phi_{\omega/2\omega} = 1.7\pi$ (Fig. 5.5 **a–c**), the second-harmonic field suppresses the instantaneous field during the second (fundamental) half cycle while enhancing it during the first half cycle. This results in electrons that backscatter upon odd-returns only. For $\phi_{\omega/2\omega} = 1.1\pi$ (Fig. 5.5 **d–f**), even returns dominate, and we note that higher even-returns cause an increase in the cut-off energy from cycle to cycle, as expected [56]. Instead, for odd-order returns the cut-off decreases with increased number of returns. This is why in Fig. 5.5 **b** the yield remains identical above each new cut-off for subsequent returns. Our analysis demonstrates we can select odd or even-return scattering electron pathways by adjusting the relative phase between the two color components. For certain energy intervals close to the highest cut-off only very few electron trajectories contribute because of the decrease or increase of the cut-offs as a function of the number of returns.

Odd or even returns consist of a short- and a long-trajectory branch, as indicated in Figs. 5.5 **b** and **e**. Hence, having restricted the number of dominating trajectories to odd or even-returns, the question arises whether the long or the short trajectories prevail in each of them.

5.2.2 Short vs Long quantum orbits

Electron trajectories are built into semiclassical description using an integral over time, as shown in Chap. 2 and Chap. 4. However, in the quantum perspective, the signal at each energy accumulates within a time interval of finite width. To give an estimation of how much a particular solution contributes to the accumulated yields within an opt. cycle, we show in Fig. 5.6 the SFA predictions with the TDSE-based yields integrated at different phase-delays. The choice of using SFA rather than CQSFA is motivated by the excellent match found in the high-kinetic energy range between the classical and TDSE predictions (see Figs. 5.5 **b** and **e**). To provide a qualitative comparison, we integrate the SFA and TDSE calculations over the same kinetic energy range. That is $7-10\,U_p$ for the first and $4-7\,U_p$ for the second returns multiplied by the modulation of their classical cut-off energy as function of the relative phase $\phi_{\omega/2\omega}$ as presented in Fig. 5.4 **c**. The TDSE-based yields are extracted at their maximum growth when the accumulated signal reaches approximately 50% of the total contribution per laser cycle. A corresponding FHWM gives boundaries defined at 10% and 90% of the total contribution.

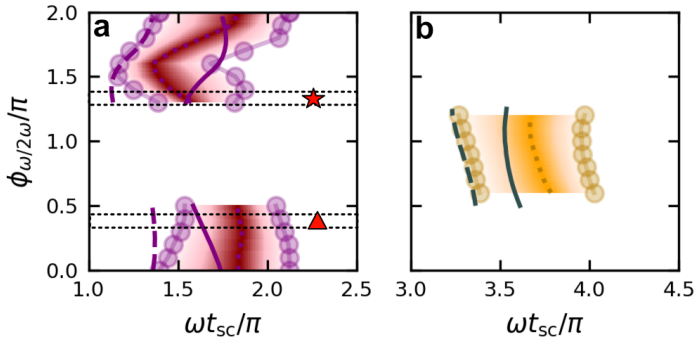

FIGURE 5.6: **Comparison of the semiclassical SFA model and TDSE. a-b**. Dark red and orange regions indicate the scattering times t_{sc} obtained by propagating electrons back in time from intervals when the TDSE yield mainly grows for the first opt. cycle (see **a**) and the second opt. cycle (see **b**). Dotted purple and orange lines are the times of half-maxima of the TDSE-based yields within their respective boundaries shown as the round markers. The rescattering times t_{sc} for the first long (purple solid lines), first short (purple dashed-lines), second long (grey solid lines) and second short (grey dashed-lines) returns predicted from the SFA show a clear dependency on the relative phase $\phi_{\omega/2\omega}$. Particularly, we found the TDSE-based yields start growing from the first long solutions at phases $\phi_{\omega/2\omega} \sim 0.35\pi$ and $\phi_{\omega/2\omega} \sim 1.35\pi$ (see the red triangle and star in **a**).

Starting from Fig. 5.6 **a**, we see that for some relative phases, the yields start rising from the long first-return trajectory, while for others, the short trajectory contributes as well. For example, at relative phases $1.5\pi < \phi_{\omega/2\omega} < 1.7\pi$, the signal mainly builds up from the short solutions and reaches a maximum quickly before the SFA predicted long solutions. On the contrary, at relative phases $\phi_{\omega/2\omega} \sim 0.35\pi$ (red triangle) and $\phi_{\omega/2\omega} \sim 1.35\pi$ (red star), the signal starts growing from the long first-return trajectory. Thus, we can control the nature of the first-return solutions by adjusting the relative phase. For the dynamics investigation of the second opt. cycle when the relative phase maximises the second-return trajectory ($0.6\pi < \phi_{\omega/2\omega} < 1.3\pi$) as shown in Fig. 5.6 **b**, no such clear transition is found rendering the reduction of long/short solutions ambiguous. Nevertheless, we see the main growth of the TDSE-yields area shifted after the "long" second-return solutions. Therefore, we will use on next chapter, classical long solutions to describe main features about second-order rescattering.

5.3 Towards one single type of trajectory

In the previous section, we have shown the ability to isolate one single type of trajectory via sub-cycle control. As odd-order rescattering cut-offs decrease with the increasing returns, we can associate one spectral window $\Delta P_{\parallel}$, where LIED sub-femtoseconds temporal resolution can be restored.

5.3.1 Attosecond control on LIED

In Fig. 5.7 **a**, we show the longitudinal momentum spectral range $\Delta P_{\parallel}$, between the first and third cut-off energy as a function of the relative phase $\phi_{\omega/2\omega}$. In principle, first and third return share similar rescattering solutions, while being delayed by one optical cycle, leading to a small difference in their cut-off energies as indicated by the dashed black line. Varying $\phi_{\omega/2\omega}$ reduce or increase that gap in momentum $\Delta P_{\parallel}$ as indicated in Fig. 5.7 **a** by the red triangle and star, respectively. Following the beige line for $I_{2\omega}/I_{\omega} = 0.13$, a factor of 1.5 times larger is found at $\phi_{\omega/2\omega} \sim 1.35\pi$ compared to the single color case. Interestingly, as we increase the second harmonic intensity to $I_{2\omega}/I_{\omega} = 1.00$, we dramatically increase this factor by 3, as marked by the blue star.

In order to illustrate those changes in the 2D photoelectron momentum distribution, we show the experimental results from a single color and two-color fields with $\phi_{\omega/2\omega} \sim 1.35\pi$, $I_{2\omega}/I_{\omega} = 1.00$ as shown in the top and bottom insets of Fig. 5.7 **b**, respectively. The change in the spectral range is about 9 against 3 bins only from previous single color LIED fields. We should stress that the resolution is definitely upgraded, so one could have more flexibility estimating that window with increasing the voltage and covering a larger detected solid angle, as we usually do in our LIED measurements [91, 128, 145].

Then, we perform a mapping energy to rescattering time for the two ideal conditions found from Fig. 5.7 **a** as illustrated by the red and blue stars. In Figure

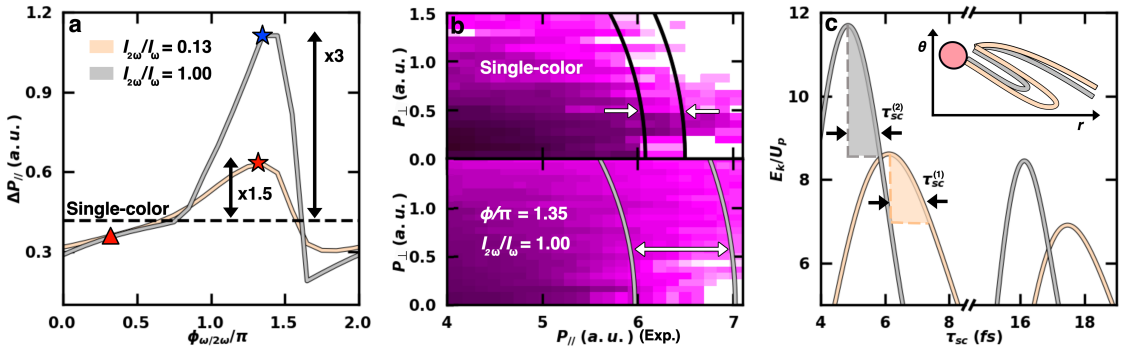

FIGURE 5.7: **Time-resolved LIED application in two-color fields a** Classical predictions of the relative difference between the first and the third maximal return momentum $\Delta P_{\parallel}$ as a function of $\phi_{\omega/2\omega}$. The maximum gap is found at $\phi_{\omega/2\omega} \sim 1.35\pi$ as indicated by the red star for a two-color intensity ratio of $I_{2\omega}/I_\omega = 0.13$ (beige line) and increase up to a factor of 3 greater (see blue star) for $I_{2\omega}/I_\omega = 1.00$ (gray line) with regard to single-color field. **b** Experimental 2D photoelectron momentum for single-color fields (top inset) and two-color fields (bottom inset) with $I_{2\omega}/I_\omega = 1.00$ and $\phi_{\omega/2\omega} \sim 1.35\pi$. The intensity of the fundamental component I_ω is kept constant and the yield is normalized to the same colorbar as in Fig. 1.2a. **c** Classical calculations of the first and third orbits rescattering time τ_{sc} as function of the photoelectron kinetic energy E_k/U_p for $I_{2\omega}/I_\omega = 0.13$ (beige line) and $I_{2\omega}/I_\omega = 1.00$ (gray line). The temporal information and energy range which allows one single trajectory is highlighted by the dashed areas. Varying the second harmonic intensity while keeping the fundamental constant accelerates the recollision process at that particular phase delay $\phi_{\omega/2\omega} \sim 1.35\pi$ as shown by the inset/sketch. It results that $\tau_{sc}^{(1)}$ and $\tau_{sc}^{(2)}$ are well separated broadening together a temporal information of nearly 3 fs.

5.7 **c**, we show the energy range associated with a single trajectory contribution, for each value of intensity ratio as indicated by the respective shaded areas. We found that the corresponding rescattering time windows $\tau_{sc}^{(1)}$ and $\tau_{sc}^{(2)}$, as indicated by the black arrows in Fig. 5.7 **c** span over about 1 fs. As we increase the two colors ratio, while keeping the fundamental constant, we enhance the acceleration of the rescattering electrons (see inset in Fig. 5.7 **c**). Such control enables us to shift the rescattering window within the optical cycle over approximately 3 fs, representing one third of an optical period.

5.3.2 Long-range effects

Finally, we emphasize the role of the long-range potential behavior on the rescattering plateau by contrasting the results obtained from a single-color numerical calculation with a zero-range potential.

The importance of including the long-range potential on the calculations is demonstrated in Fig. 5.8 for a single color fields at a central wavelength of 3.2 µm. More specifically, we show that the first-return short trajectory contributes with a zero-range potential whereas it does not for a long-range Coulomb tail. This has significant implications on LIED since it validates in the case of a single color

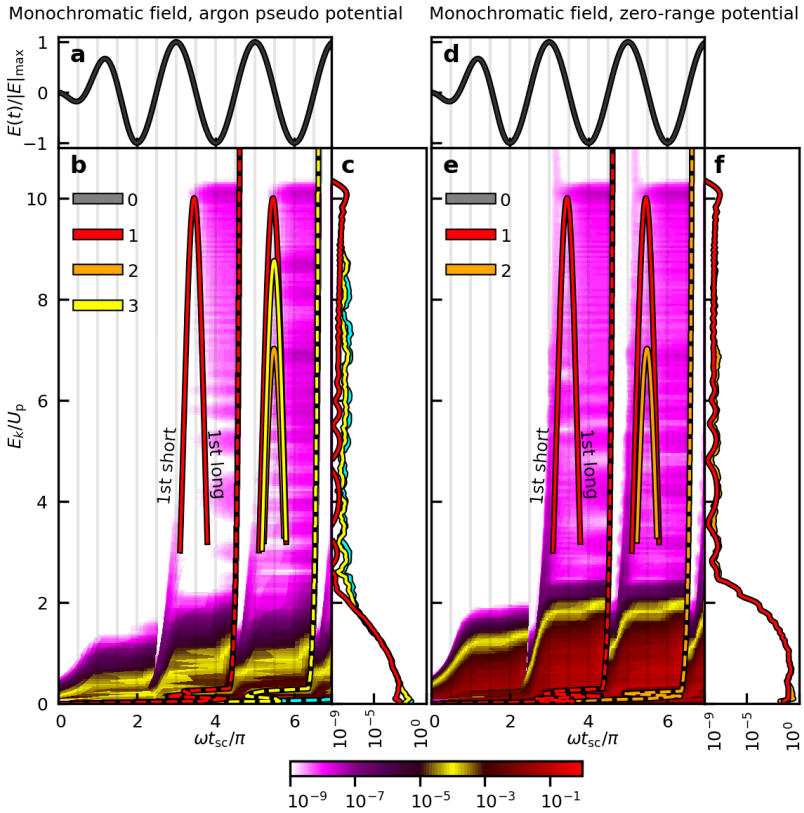

FIGURE 5.8: **Coulomb vs zero-range potential. a–c** Same as in Fig. 5.5 but with the second-harmonic field intensity equal zero. The magnitude of the signal from the first-return short trajectory is negligibly small and the signal is formed by first-return long trajectory and by higher-order returns. **d–f** Same as **a–c** but with the argon pseudo potential additionally replaced by a zero-range one supporting a 1*s* state with the same ionization energy 15.8 eV as of argon atom. The influence of the first-return short trajectory is prominent. Also higher-order returns almost don't contribute.

measurement that the first long return dominates over the first short return trajectory. Additionally, the contribution of higher-order returns can be misreading without proper Coulomb corrections.

5.4 Outlook

By setting two key parameters of the strong two-color laser field – the wavelength, and the relative phase between the two fields – we thereby access and control the electron dynamics on a single-atom level. Quantum interference via the two-color field relative phase $\phi_{\omega/2\omega}$ allows us to manipulate the signals from single- and multiple-return trajectories in both energy and time. In the NIR, due to considerable time and energy overlap, separation of those signals is not possible. In this regard, the use of long-wavelength MIR lasers is essential. We showed that using the MIR (3.2 µm+1.6 µm) laser together with the proper adjustment of the relative phase $\phi_{\omega/2\omega}$ gives us a possibility to eliminate from the total spectrum the contribution of the electrons that undergo scattering on the parent ion upon

the first incident of close return, thereby, leaving the higher even-return-scattered electrons to be dominant. Moreover, the contribution of long/short trajectories can be maximized/minimized for certain relative phases. As the rescattering cut-offs decrease for odd higher-order returns, the number of contributing trajectories around the highest cut-off energy can be reduced to one, which is important for the unambiguous analysis of measured LIED data.

It is worth-mentioning that the rescattering dynamics observed in this Chapter depend on the choice of the combined laser fields parameters and most importantly on the intensity ratio between the fundamental and the second hamonic pulses $I_\omega/I_{2\omega}$. Therefore, we cannot extend these results to explain the responsible mechanisms that will occur in a single-color measurement [131]. Instead, we chose to show in this chapter a different two-color combined field setup that allows us to control the recollision mechanisms and therefore provide a route towards sub-femtoseconds time-resolved LIED measurements. Additionally, we performed TDSE calculations that we show in appendix A for the upper boundary $I_{2\omega}/I_\omega = 1.00$ at $\phi_{\omega/2\omega} = 1.35\pi$ (blue star in Fig. 5.7 **a**) to validate our assumptions from Sec. 5.3, that the short first returns remain turned off while varying $I_{2\omega}/I_\omega$ along the branch at $\phi_{\omega/2\omega} = 1.35\pi$.

Finally, we show that the contributions of certain trajectories to the yield also depends on the long-range behavior of the potential. For example, we show in the single color case that the first-return short trajectory contributes with a zero-range potential whereas it does not for a long-range Coulomb tail. Since a recent volume of work can be explained with models including the magnetic component of the laser fields for laser parameters similar to the ones we use in this thesis [40, 146, 147, 148], thus, it would be interesting to know the effects on certain trajectories including the interplay between the magnetic drift and the coulomb momentum transfer [149, 150, 151, 152].

Chapter 6

Backscattered electrons on molecules

In LIED, the first-long return trajectory is commonly used to discriminate from the complexity dynamics of strong-fields measurement, rendering the method an applicable field free imaging technique [19, 20, 43, 44, 91, 127, 128, 145, 153, 154, 155]. However, we have seen in the previous chapter that first and multiple-order return contribute at equal footing (see Fig. 5.8 **a** for a single color) despite the intuitive picture of first return trajectory that may benefit from a reduced wavepacket spreading. In addition, we saw with the classical trajectory calculations, as shown in Fig. 5.5, that the higher-order returns get similar scattering time along their particular branch "even" or "odd" with increasing order except that they are delayed each time by exactly one opt. cycle. In Sec. 5.2.2, we assigned the second return electrons trajectory to the long classical solution. Hence, this chapter is split in two parts. Sec. 6.1 and Sec. 6.2 use the approximation based on the SFA which states that the first-long trajectories are the dominant ones. We start by a general introduction of LIED, how to extract molecular structure from the two-dimensional momentum distribution before introducing an alternative method "ZCP-LIED" for reading the molecular structure directly from the laboratory frame. In Sec. 6.2, we show that the molecular structure can be retrieved with only the critical crossing points of the molecular interference term (MIT). By investigating only the phases of the interfering terms, the ZCP-LIED method relaxes the limitation of the Born approximation that is at the heart of electron diffraction theory. Then, in Sec. 6.3 we study the orientation dependency of the molecules on backscattering LIED measurement and include in the analysis up to the third return trajectory by choosing the "long" rescattering solution. In this chapter, we should point out that the temporal dynamics are not assigned apart when the results are presented together with a chemistry dynamical calculation for the Renner-Teller candidate, *OCS* (see Sec. 6.2.3). In the end, we give a short summary in Sec. 6.4.

6.1 Conventional LIED analysis: QRS

In order to illustrate the LIED analysis, we are showing in this section previous published results based-on acetylene [20]. In MIR-LIED and in the tunneling regime, an electron is tunnel-ionized close to the peak of the electric field. Quantum mechanically, a range of quantum trajectories re-encounter the molecule where the electron scatters, thus acquiring a momentum shift p, which embeds

structural information. As shown in the previous chapter, scattering trajectories lead to the highest final (measured) electron kinetic energies ($E_k > 2U_p$), in this way allowing us to distinguish them from non-scattering trajectories at low kinetic energies ($E_k < 2U_p$).

6.1.1 Extracting the scattering information in the laboratory frame

The described dynamics in Fig. 6.1 is governed by the laser field, i.e., the dynamics occurs in the laser polarization frame. A closer look at the dynamics shows that the scattered electron (blue) re-encounters the molecule (distance r=0) at time $t_{r,1}$ in the presence of the laser field, thus acquiring an additional momentum $A(t_{r,1})$. The measured momentum consists of two contributions, the momentum which is imparted due to scattering of the molecule k_1 and the momentum imparted by the laser $p(t_{r,1})$. So, knowledge about the vector potential $A(t_{r,1})$ is needed to extract k_1 from measuring p_1 in the laboratory frame as reported in Fig. 6.1 panels **a**,**b** and **c**.

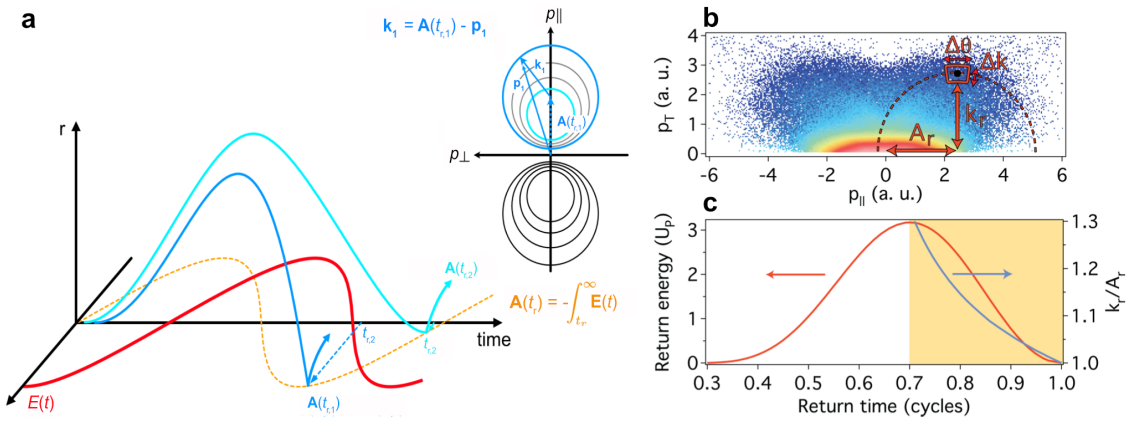

FIGURE 6.1: **Extraction of field-free scattering signal in the presence of a strong laser field from laboratory-frame photoelectron momentum. a**. Figure taken from the supplementary material of [145]. The electric field (red) together with its associated vector potential (yellow dashed) of the laser pulse. An electron tunnel ionizes in the presence of a strong laser field and two possible "long" quantum trajectories are shown in blue and turquoise. The emitted electron is first driven in the direction given by the scalar product $q.E$ before returning and scattering against the target at some time later t_r where it acquires a scattering momentum k plus a momentum kick $A(t_r)$ from the vector potential. The electron is detected with momentum p. **b**. The DCS are extracted by drawing a circle on the 2D cylindrical experimental data centered at a momentum kick A_r with a radius of k_r the scattering momentum. **c**. The values of k_r and A_r can be calculated classically and the ratio of the two is shown for the long trajectories (orange shading).

6.1.2 Molecular bond-length retrieval with the independent atomic model

The total scattering cross-sections (I_T) can be seen as a sum of coherent (I_M) and incoherent (I_A) interferences. For practical visualization, we usually contrast the coherent term (I_M) against the incoherent atomic scattering signal (I_A) and label it the molecular contrast factor MCF.

$$MCF(q) \equiv \frac{I_T(q) - I_A(q)}{I_A(q)} = \frac{I_M(q)}{I_A(q)} = \frac{1}{I_A(q)} \sum_{i \neq j} f_i f_j^* \frac{\sin(qR_{ij})}{qR_{ij}} \tag{6.1}$$

where q is the 1D momentum transfer ($q = 2k_r sin\frac{\theta_r}{2}$), f_i the complex scattering amplitude for the ith atom, and R_{ij} the interatomic separations. In Fig. 6.2, we use Eq. 6.1 and fit the experimental results with a genetic algorithm. The residuals presented in Fig. 6.2 **a** are defined as follows:

$$\chi^2 = \sum_{i=0}^{n} \frac{(MCF_{th} - MCF_{exp})^2}{\sigma_i} \tag{6.2}$$

where σ_i is weighted by a normal distribution ($\sigma_i = 1$) or a poissonian distribution ($\sigma_i = \Delta MCF(q) = \frac{\sqrt{I_T(q)}}{2I_A(q)}$).

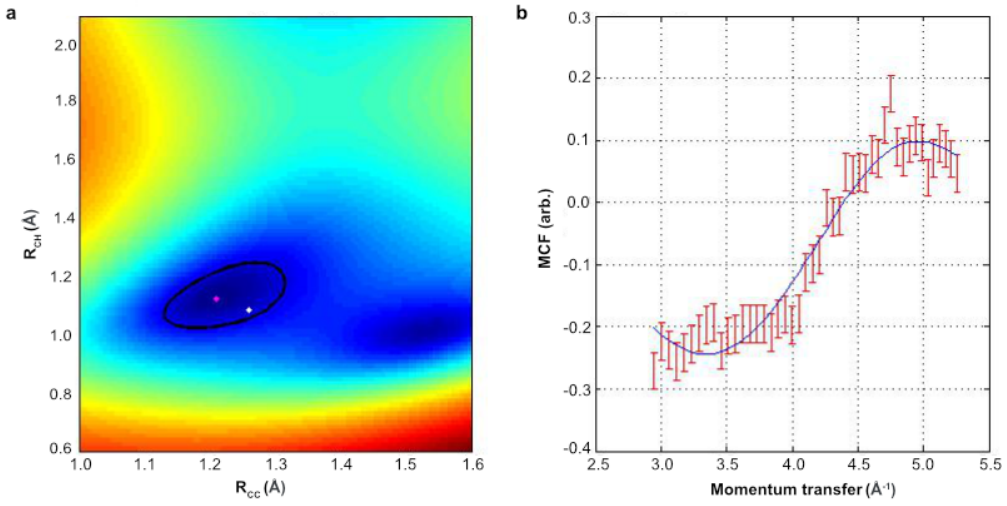

FIGURE 6.2: **Conventional IAM on acetylene molecule. a**. A logarithimcally scaled map of the multiple bond length fitting routine for a particular electron energy. The known bond lengths are indicated by the white dot while the position of best fit (χ^2_{min}) is indicated by the black dot. The black countour plot represents a deviation of 10% the value of χ^2_{min}. **b**. Best theoretical fit vs the experimental MCF as function of the momentum transfer q.

Assuming the first long trajectory to be the dominant process, one can translate the rescattering momentum into an *instant* time t_r being a fraction of a laser period. In the Born-Oppheimer approximation, the different angular cross-sections

extracted at fixed rescattering momentum (see Fig. 6.2 **b**) can be seen as a collection of independent measurements narrowing further down the uncertainty on the retrieved bond-lengths [20].

6.2 ZCP-LIED

In Xu et al. [153] and later [43], a variant of LIED, "FT-LIED", was suggested in which only backscattered electron distributions are analysed. It employs a fourier transform and this way, it lies in a faster data extraction procedure without the need for iterative algorithm. Moreover, it is background-free which means that no theory is needed. Indeed, backscattered interferences result in large amplitude oscillations due to the greater momentum transfer range. For this reason, a simple empirical fit can be used for the subtraction of the molecular interferences [6]. However, such Fourier-transform tools are limited by their bandwith frequency and can lead to broad radial distribution if two internuclear distances are close to each other. In that sense, we introduced an alternative scheme [145] for exploiting the two-dimensional data available. This method directly extracts the molecular structure in the laboratory frame and unlike conventional LIED, it is based on the identification of critical zero crossing points (ZCPs) of the molecular interferences which makes "ZCP-LIED" simpler and most importantly efficient as we will see later on.

6.2.1 FT-LIED

To test our model we use *OCS*, a triatomic molecule. Briefly, a gas mixture of 1% *OCS* seeded in helium was supersonically expanded through a 30 µm aperture, generating a molecular beam with an internal temperature of $< 90^{\circ}$K. The molecular beam was collimated using two skimmer stages and subsequently overlapped with a 96 fs (FWHM) 3.2 µm laser pulse generated by an optical parametric chirped-pulse amplifier (OPCPA) in the interaction region of the reaction microscope. The field strength of the 3.2 µm laser pulse corresponded to a Keldysh parameter of $\gamma \approx 0.3$ and a ponderomotive energy of $U_p = 90\,eV$, which led to photo-ionization of electrons with maximal return and back-rescattered electron kinetic energies of $\mathrm{E}_{ret,max} = 3.17\,U_p \approx 285\,eV$ and $\mathrm{E}_{resc,max} = 10\,U_p \approx 900\,eV$, respectively. To detect the ions and electrons we applied homogeneous electric and magnetic fields of 19.1 $V.\mathrm{cm}^{-1}$ and 10.4 G. The cyclindrical 2-dimensional photoelectron momentum distribution is presented in Fig. 6.3 **c** and is extracted in coincidence from the OCS^{+} ion time-of-flight as indicated in Fig. 6.3 **a**.

The experimental differential cross-sections (DCS) are extracted the same way as shown in Fig. 6.1 except that the angle is fixed at $\theta_r = 180^{\circ}$. Fig. 6.4 **a** shows the backscattering yield with its corresponding error-bars given by the longitudinal detected momentum (red horizontal) and a Poissonian distribution (blue vertical). To show the molecular interferences, we subtract from the DCS the incoherent sum of atomic scattering defined by a linear regression filter (black starred line). The MCF are shown in Fig. 6.4 **b** with their corresponding errors.

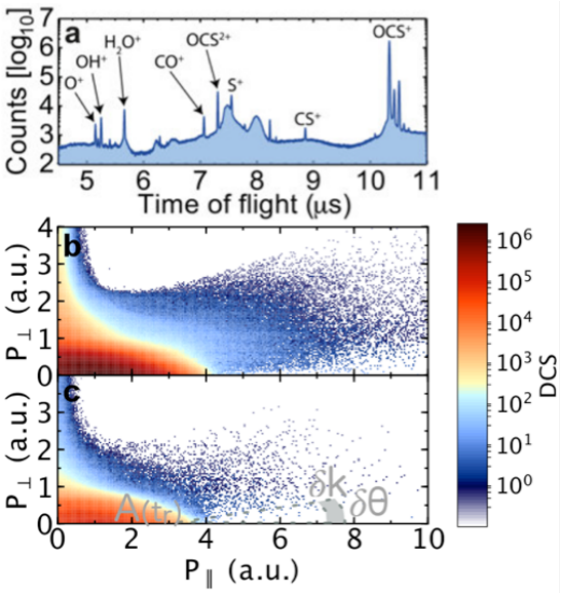

FIGURE 6.3: **FT-LIED extraction method. a**. Measured ion time-of-flight (TOF) spectrum. **b**. Two-dimensional ($P_{\parallel}$,$P_{\perp}$) electron momentum distribution (i.e. electron momenta emitted perpendicular and parallel, respectively to the laser polarization direction) for all electrons. **c**. Same as **b** but for electrons detected in coincidence with OCS^+. The analysis sketch is similar to Fig. 6.1 except that the angle is fixed $\theta_r = 180°$. Backscattering results in hard scattering with small impact paramaters. Thus, the coincidence is an important step of the background reduction.

The resulting radial distribution (black dashed line) displays three distinct peaks, with the area of uncertainty indicated by the shaded regions corresponding to the detected longitudinal error (red horizontal) and the Poissonian statistical error (blue vertical). The black dotted lines represent the minimum and maximum interatomic distance found from these deviations. We measure values of $R_{CO} = 1.06 \pm 0.06$ Å, $R_{CS} = 1.87 \pm 0.13$ Å and $R_{OS} = 2.78 \pm 0.10$ Å. The resulting angle ϕ_{OCS} is derived from a first order Taylor expansion,

$$\delta\phi = \sqrt{(\frac{\delta\phi}{\delta R_{OS}}\delta R_{OS})^2 + (\frac{\delta\phi}{\delta R_{CS}}\delta R_{CS})^2 + (\frac{\delta\phi}{\delta R_{CO}}\delta R_{CO})^2} \tag{6.3}$$

$$\text{where, } \phi = \cos^{-1}(\frac{R_{CO}^2+R_{CS}^2-R_{OS}^2}{2R_{CO}R_{CS}})$$

Such geometry corresponds to an important bending with $\phi_{OCS} = 142 \pm 22°$.

6.2.2 ZCP-LIED retrieval of OCS^+ structure

Now, we turn to the ZCP-LIED procedure in which we extract the signal in the laboratory frame (origins ($P_{\parallel}$, $P_{\perp}$) centered in zero). The analysis was developed by Su-Ju Wang in collaboration with the Kansas University under the supervision of Prof. Chii-Dong Lin. We comment below the procedure steps. The differential scattering cross-sections (DCS) from 17 laboratory-frame angles between 0.0 and

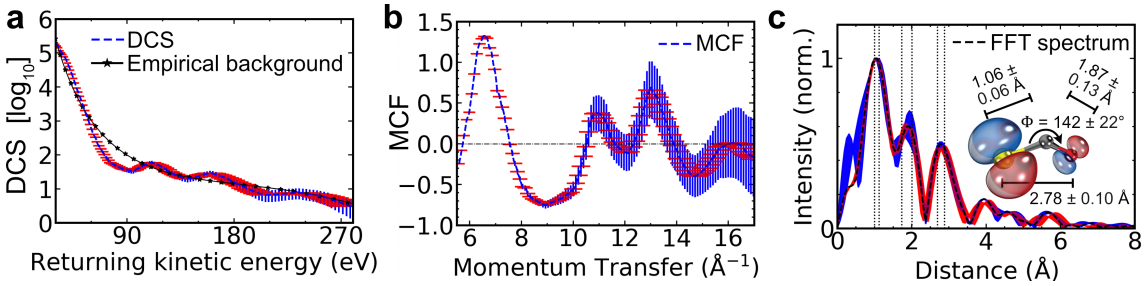

FIGURE 6.4: **FT-LIED retrieval of OCS^+.** Figure taken from [145]. **a**. Differential cross-section (DCS; blue dashed line) as a function of returning kinetic energy corresponding to electrons detected in coincidence with OCS^+. A linear regression filter (black starred line) is applied to the DCS to extract the incoherent sum of atomic scatterings, I_A. The area of uncertainty is given by the longitudinal detected momentum error (red horizontal) and the statistical error based on a Poissonian distribution (blue vertical). **b**. The molecular contrast factor (MCF), defined by I_M/I_A, as a function of momentum transfer. **c**. Radial distribution (black dashed line) obtained by the Fourier transform (FT) of the MCF distribution. The uncertainty in the measured peaks is indicated by the black dotted vertical lines (see text for more details). A schematic of the retrieved asymmetrically stretched and bent OCS^+ structure is shown in the inset.

4.0° were extracted in steps of $\Delta\theta = 0.25°$ across the scattering momentum, p, range of 4.72–7.16 a.u. Since the signal begins to rise quickly due to contributions from "direct" electrons and because IAM cannot be applied at small scattering energies, we did not include momenta lower than $p = 4.72$. Similarly, at momenta above $p = 7.16$, the contrast in the modulated signal becomes very small due to an insufficient signal-to-noise ratio.

To identify the zero-crossing points (ZCP), as indicated in Fig. 6.5 **a** by the dashed magenta lines, we apply a linear regression fit on the DCS. The ZCPs are the roots of the molecular interferences signal. In Fig. 6.5 **b** we show the positive and negative values of the interferences signal I_M (Fig. 6.5 **a**). We extract 4 ZCPs with their corresponding variance as illustrated in Fig. 6.5 **c**. Those experimental ZCPs are compared to theoretical ZCPs for a variety of different molecular structure using IAM.

The reconstructed ZCPs generated with an optimization process for all four momentum points (5.21, 5.82, 6.37, 6.97 a.u.) is shown in Fig. 6.6 **a**. The optimal internuclear distances found are $R_{CO} = 1.18$ Å, $R_{CS} = 1.70$ Å and $R_{OS} = 2.74$ Å as shown in the inset of Fig. 6.6 **b**. Since the DCS were integrated over a bandwidth of Δp=0.1 a.u. to further extract the molecular interferences, Fig. 6.5 **c** shows the number of angles where the ZCPs fall within $\frac{\Delta p}{2}$. As one can see, half of the ZCPs fall above or below the magenta dashed line within 0.1 a.u.. Therefore, we can estimate the error of each ZCP, and, in turn, calculate the error of the retrieved bond lengths. We report values of $R_{CO} = 1.18 \pm 0.02$ Å, $R_{CS} = 1.70 \pm 0.02$ Å and $R_{OS} = 2.74 \pm 0.03$ Å resulting in an O–C–S bond angle of $\phi_{OCS} = 144 \pm 5°$.

The theoretical molecular interference signal (black dotted line Fig. 6.6 **b**) that

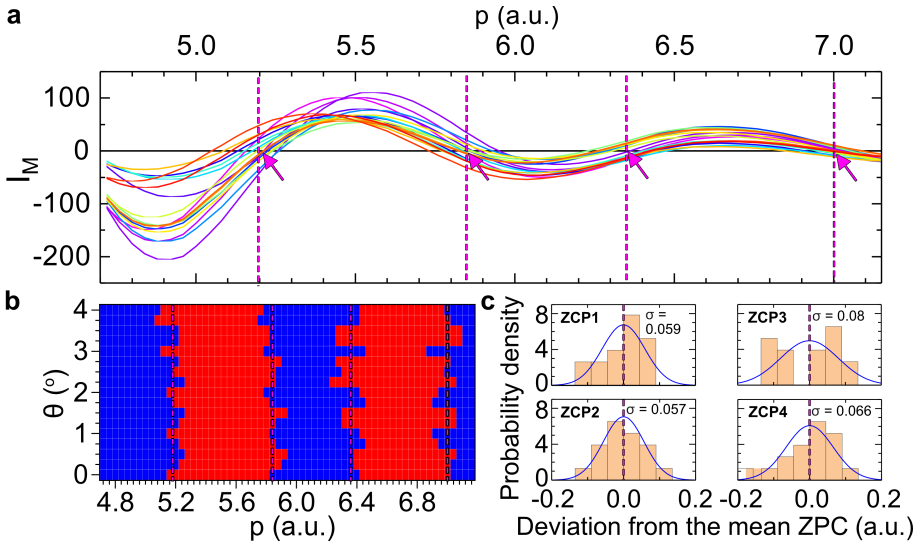

FIGURE 6.5: **Retrieval of molecular interference signal in the laboratory frame.** Figure taken from [145]. **a**. Molecular interferences I_M in the laboratory frame for 17 different angles between 0.0 and 4.0° in steps of $\Delta\theta = 0.25°$. The roots mean position of the molecular interferences (ZCPs) are indicated by the magenta dashed lines. **b**. Two-dimensional map of the negative (blue squares) and positive (red squares) parts of the molecular interference signal as a function of the laboratory angle and momentum. **c**. Frequency of occurrences of finite-width distributions of each experimental ZCP obtained from **b**.

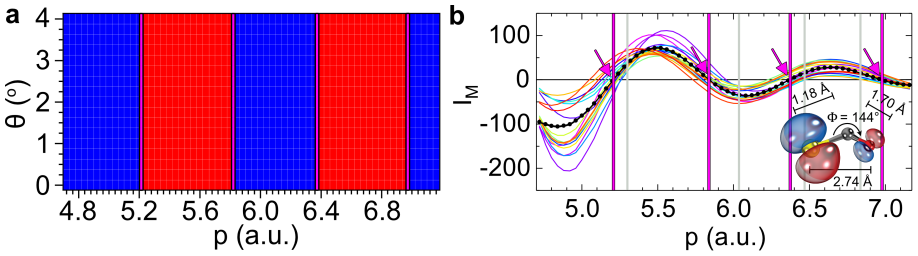

FIGURE 6.6: **ZCP retrieval structure of OCS^+.**Figure taken from [145]. **a**. Reconstructed 2D map calculated using the IAM model from the experimental results shown in Fig. 6.4 **b**. **b**. Molecular interference signal, I_M, for the experimental data (coloured lines) and the corresponding theoretically calculated distribution (black dotted line) that fits the measured data best. A schematic of the reconstructed molecular structure matching the 4 ZCPs (magenta vertical lines) is shown. The equilibrium neutral ground-state OCS (grey vertical lines) is presented for comparison.

best reproduces the measured data (coloured lines Fig. 6.6 **b**), corresponds to a significantly bent and asymmetrically stretched OCS^+ structure. Finally we compare our retrieved structure in Fig. 6.6 **b** with the equilibrium neutral ground state of OCS as indicated by the grey lines. We see that the ZCPs for the equilibrium neutral ground state of OCS are in poor agreement with our exprimental results.

6.2.3 Quantum-classical calculations

In order to explain the retrieved bent molecular structure we found from FT-LIED and later confirmed from the ZCP-LIED method, we involve theoretical calculations performed by Martin Ritcher from our collaboration with Prof. Stefanie Gräffe (University of Jena). To describe the dynamics of OCS in the presence of the 3.2 µm laser pulse, we used quantum chemical calculations on the CASSCF/aug-cc-pVTZ level of theory in combination with the classical surface hopping method. In the absence of a field, neutral OCS in its ground electronic state is linear. The $1^1\Delta \leftarrow 1^1\Sigma^+$ transition is dipole forbidden due to symmetry. However, field-dressing OCS on the rising edge of the 3.2 µm laser field results in a significantly bent molecule (see Fig. 6.7 **c**) due to the Renner–Teller effect [91, 156, 157]. Previous work shows the same mechanism with CS_2 molecules and similar laser pulse parameters [91]. As the ionization potential of the excited state $2^1A'$ is much lower than the $1^1\Sigma^+$ ground state (5.2 eV lower), our LIED signal is dominated by the bent and asymmetrically stretched OCS^+ even if the population transfer is rather low ($\approx$ 3%).

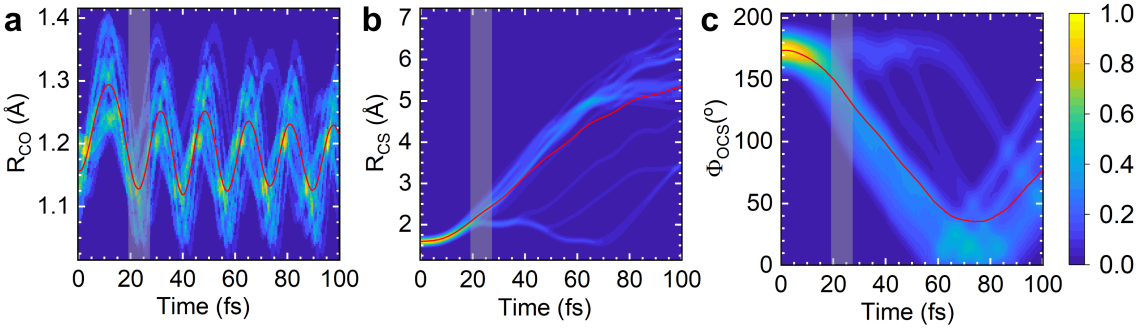

FIGURE 6.7: **Dynamical calculations of field-free neutral OCS.** Figure taken from [145]. **a-c** Mixed quantum-classical nuclear dynamics calculations of neutral field-free OCS that is slightly bent as a function of time after excitation of the neutral molecule, t. Dynamical results are shown along the C-O **a** and C-S **b** internuclear distance coordinates, R_{CO} and R_{CS}, respectively, and the O-C-S bond angle ϕ_{OCS} **c**. The average value of over 20 trajectories is shown as a red line. The dynamical calculations best reproduce our measured LIED structure at a time window of t=19.5-27.0 fs (shaded grey regions) corresponding to $R_{CO} = 1.13$Å, $R_{CS} = 2.29$Å and $\phi_{OCS} = 141^\circ$

The neutral molecule undergoes significant nuclear deformation on the rising edge of the 96 fs (FWHM) 3.2 µm laser pulse. In previous study of CS_2 [91], it was shown that the time window for the population of the excited state is about 50 fs which coincides with the maximum peak of the laser fields. For the linear OCS^+ structure retrieved at 2.0 µm by Karamatskos et al.[155], the reported pulse duration of 38 fs (FWHM) was probably too short to cause structural deformation on the neutral OCS molecules. Finally, we show additional results in the (O^++$C^{32}S^+$) dissociative pathway (see Appendix B) that lead to good agreement with the quantum classical calculations (Fig. 6.7) and the ZCP retrieval (Fig. 6.6).

6.3 Discriminating molecular orientation from double-slit backscattered interferences

In the first FT-LIED study by Xu et al. [153], the backscattering cross-section was shown to be prominent for molecules that are parallel to the electric field vector of the probe pulse. They successfully reported N_2 bond-lengths but failed in imaging O_2. Hence, they came to the conclusion that the difference observed in the total molecular interference signal is caused by the specific O_2 anti-bonding HOMO orbital. Later on, Pullen et al. [43] used a reaction microscope´s coincidence detection capability to show that molecular coherent interferences from O_2, in particular, were increased by a factor of 3 when filtering out the electrons of interest from all detected electrons, concluding on the possibility to image O_2 and C_2H_2 molecules regardless of the shape of the HOMO orbital.

In this section, we try to give an understanding about FT-LIED. The first question we would like to raise is why the method becomes a valid tool in resolving molecular structure for a various number of target [127, 128, 145, 158] after Pullen et al. [43] first success? For this, we go back to Pullen et al. data analysis to study the original molecular interferences obtained without further data processing. Then, we bring an update on the LIED analysis including additional returning trajectory in the calculation of the vector potential A_r and rescattered momentum k_r as mentioned in the beginning of this chapter. Finally, we see that in the backscattered interferences is encoded a deeper property about wave diffraction in molecules rendering FT-LIED applicable to any target system under the condition that a coincidence scheme is applied to prevail from the low signal-to-noise.

6.3.1 Surprisingly high contrast factor in Pullen et al. data

In the Nature communication of Pullen et al. [43], the interference signal was referred as logarithmic difference $\rho = log_{10}(\frac{I_T}{I_A})$ (see supplementary materials). So, in order to compare with other LIED measurements, we need to rescale the interference signal in the conventional MCF unit first:

$$MCF = I_T/I_A - 1 = 10^{\rho} - 1 \tag{6.4}$$

The conversion is shown in Fig. 6.8. For example, a unit defined as in [43] $\rho = 0.2$ (see Fig. 6.8 **a**) will correspond to a MCF value of $10^{0.2} - 1 = 0.58$ (see Fig. 6.8 **b**). Then, to reduce spectral leakage a windowing function (gray dashed line in Fig. 6.8 **b**) was applied in the extraction step right after obtaining the molecular interference from the total signal (see supplementary materials for more details). This leads to a suppression of the signal at the edges to make the signal continuous.

Interestingly, the contrast factor found for the electrons detected in coincidence is not a factor of three compared to all electron signal as mentioned in [43], but more a factor of 4 to 5 greater which is tremendous (see Fig. 6.8 **b**). Indeed, the maximum of the interference signal is found at MCF$\approx$ 0.8 which translates to, before applying the windowing function, MCF$\approx$ 1 (factor of 1.25 greater). In

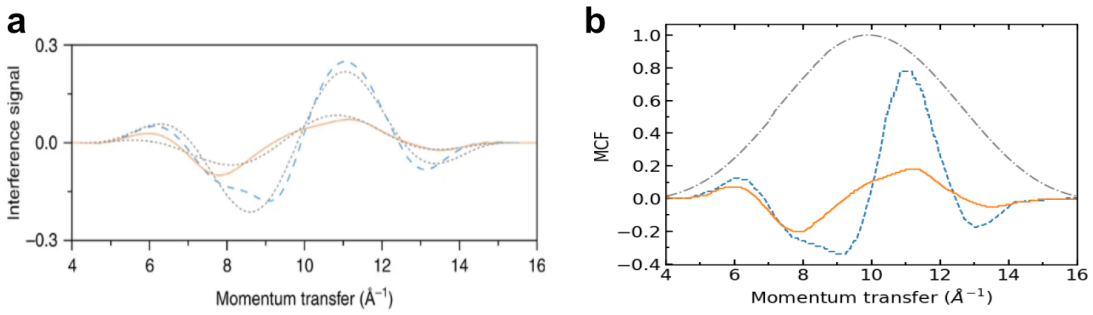

FIGURE 6.8: **O_2 backscattered interferences.** **a**. Fig. 3**c** in Pullen et al. [43] **b**. interference signal taken from **a** and adapted to the conventional Molecular Contrast Factor (MCF) unit for all electrons (orange line) and electrons in coincidence with O_2^+ ions (dashed blue line). A windowing function (gray dashed line) is applied to the interference signal for reducing spectral leakage (see supplementary materials [43])

principle, such modulations are only accessible for pre-oriented molecules as we will show through a development of theoretical calculations.

6.3.2 Update on the LIED analysis

To account for the multiple returning trajectory in the calculation of the vector potential A_r and rescattered momentum k_r, we derive the classical calculations for the first long, second long and third long solutions as shown in Fig. 6.9.

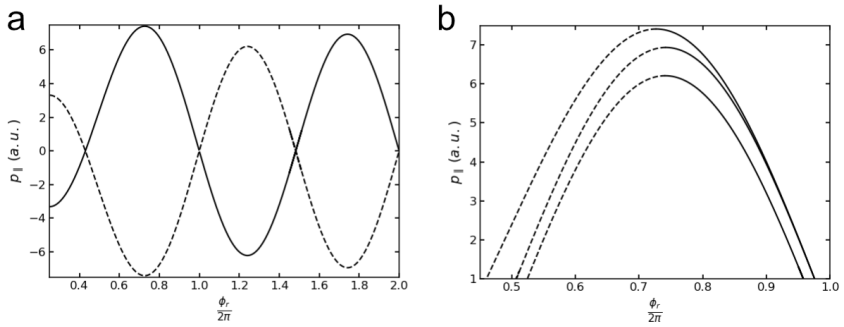

FIGURE 6.9: **Multiple return trajectory solutions.** **a**. Classical predictions of the rescattering phase $\frac{\phi_r}{2\pi}$ as function of the longitudinal momentum $P_\parallel$ for the first, second and third returns. The solid and dashed lines differ in ionization time from two adjacent half-cycles **b**. The three solutions are ionized in different half-cycle overlapping towards the same final momentum direction $P_\parallel$. Long and short solutions are shown by the solid and dashed lines, respectively.

With one single trajectory we find the unique solutions k_{tr} and A_{tr} that meet the detected electron momentum $P_\parallel$ defined as follows:

$$k_{tr} + A_{tr} = P_\parallel \tag{6.5}$$

While for three tajectories, Eq. 6.5 becomes a linear combination of the three solutions:

$$\frac{k^1_{tr} + A^1_{tr} + k^2_{tr} + A^2_{tr} + k^3_{tr} + A^3_{tr}}{3} = P_{\parallel} \tag{6.6}$$

where indexes 1, 2 and 3 correspond to the first, second and third long trajectory.

To show the differences, we plot the data presented in Pullen et al. [43] with and without including the multiple returning orders as presented in Fig. 6.10. We find a difference in the momentum transfer shifted by a maximum of 0.6 Å^{-1} and an overall offset of 0.4 Å^{-1} (see Fig. 6.10 **b**). No differences are found in the values of the retrieved Fourier peaks (see Fig. 6.10 **c**) which is not surprising because both signal look similar apart from the fact that they differ from a maximal offset of 0.6 Å^{-1} being within the bandwith limit $\frac{2\pi}{\Delta q(\text{Å}^{-1})}$. However, we note a small deviation $R_{OO} \approx 1.25$Å with the results reported in [43] after processing the interference signal (see Fig. 6.8) and without post-processing (see Fig. 6.10).

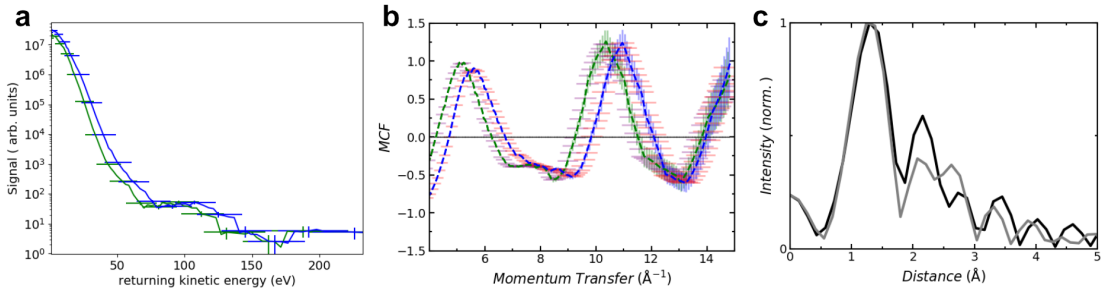

FIGURE 6.10: **Comparison single vs multiple trajectory. a**. O_2^+ differential cross section (DCS) presented in [43] and extracted using the first long trajectory (blue line) Same data but extracted with a model including the first, second and third long trajectories (green line). The errors bars are given by the momentum detector (see Chap. 2 for more details). **b**. The two MCFs extracted from **a** result in a small shift of approximately 0.4 Å^{-1}. **c**. The two Fourier-Transforms overlap significantly indicating both an internuclear distance $R_{OO} \approx 1.25$Å

In order to tell which method to trust to rely on the O-O bond-length reported values, we will compare the experimental unprocessed data with semi-classical calculations on the next section.

6.3.3 O_2 and C_2H_2 backscattered LIED interferences

Since we focus on the amplitude of the retrieved interferences, the ZCP method cannot help us understand the features shown in Sec. 6.3.1. So, we use in below calculations the conventional IAM model as presented in Sec. 6.1.2.

In order to investigate the molecular orientation dependency on the experimental backscattered interferences, we calculate IAM cross section for different alignment distributions $\rho(\Omega_L)$ as shown and illustrated in Fig. 6.11. As one can

see from Fig. 6.11 **b**, the isotropically-oriented molecules (case A) and the one-dimensional averaged theoretical calculations (case B) do not have similar amplitude as the experimental distribution (red and blue dashed for O_2 and C_2H_2 respectively). In order to appreciate same modulations as those observed in Pullen et al. experimental data, one has to fix the molecule in space with a certain narrowed degree of alignment (as shown by case C in Fig. 6.11 **c**).

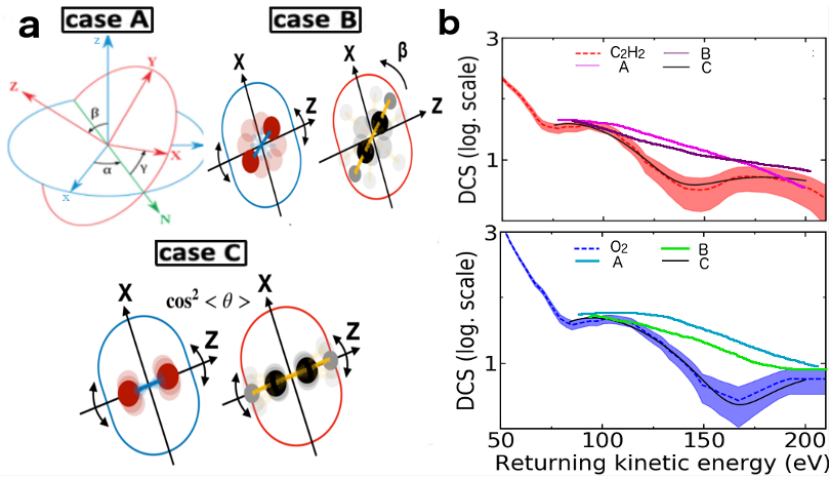

FIGURE 6.11: **Backscattered electrons investigated with IAM. a**. Three cases of molecular alignment distribution $\rho(\Omega_L)$ for O_2 and C_2H_2 molecules. Case A shows Euler averaging angles for randomly-oriented molecules. Case B shows an uniform one-dimensional average distribution while Case C illustrates one-dimensional alignment along the respective O_2 and C_2H_2 bond-lengths. **b**. Experimental backscattered interferences (red: C_2H_2, blue: O_2) with the corresponding theoretical IAM prediction for the three cases of molecular alignment distribution illustrated in **a**

To get a deeper understanding of the molecular alignment distribution embedded in the electron backscattering yield, we run a 3D fitting routine on O_2 with the following parameters:

- R_{OO}, the internuclear distance.
- Θ_0, the alignment angle with respect to the laser polarization axis.
- σ^2, the degree of alignment.

where, the alignement distribution is given by the Gaussian form $\rho(\Theta) = e^{\frac{-sin^2(\Theta-\Theta_0)}{2\sigma^2}}$.

The results are striking. In all three projections, we see a global minimum indicating a best fit for a molecule oriented in the direction of the backscattered electrons at $\theta_0 = 0$ and $\sigma^2 \approx 0.04$. Additionally, we see that the retrieved bond-length is shifted towards larger values $R_{OO} \approx 1.24$Å as compared to the previous study of Suarez et al. [159], $R_{OO} = 1.17$Å with the molecular SFA. However, we notice the same bond-length with the FFT result as shown in Fig. 6.10

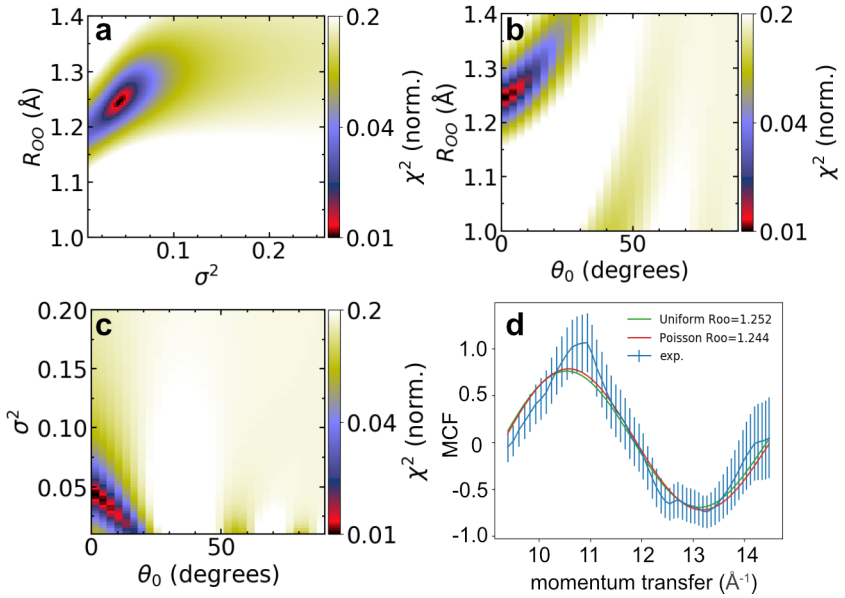

FIGURE 6.12: **3D conventional IAM fitting routine.** O_2 conventional IAM fitting routine **a**. χ^2 residuals sliced through the best Θ_0 parameter as function of σ^2 and R_{OO}. **b**. χ^2 residuals sliced through the best σ^2 parameter as function of Θ_0 and R_{OO}. **c**. χ^2 residuals sliced through the best R_{OO} parameter as function of Θ_0 and σ^2. **d**. experimental MCF (blue line) and corresponding theoretical predictions for χ^2_{min} found from an uniform (red line) and poisson (green) distribution.

Repeating the procedure with acetylene data (see red dashed line Fig. 6.11 **b** and cutting a slice through the 4D (R_{CC}, R_{CH},σ^2,Θ_0) IAM solutions, we find that both target display the same narrowed distribution (σ^2=0.042) along the polarization axis, as shown in Fig. 6.13. Then, in order to quantify the degree of alignment imprinted in O_2 and C_2H_2 molecular backscattered interferences, we contrast our results with the previous reported 1D impulsive alignment measurement of C_2H_2 molecules [20, 44]. The experimental molecular alignment retrieval presented in [20, 44] was found to match an alignment distribution with $\sigma^2 = 0.3$ (see black solid line in Fig. 6.13 **b**). At this point, we should specify that the experimental molecular alignment retrieval of [20, 44] was extracted from the direct electron and ion signal. Moreover, the laser field polarization in [20, 44] was chosen perpendicular to the time-of-flight spectrometer axis to capture most of the forward scattered electrons. The electric and magnetic fields to drive the electrons in the MCPs were kept low to reach a high electron momentum detection resolution. Thus, there was no information available on the backscattering photoelectron distribution. Instead, the measurement in [43] and analyzed further here used laser field polarization colinear to the time-of-flight spectrometer axis.

6.3.4 Multi-center atom backscattered LIED interferences

Finally, we show that the same results apply to the asymmetric and bent structure reported in Sec. 6.2, revealing a more general concept about LIED backscattered

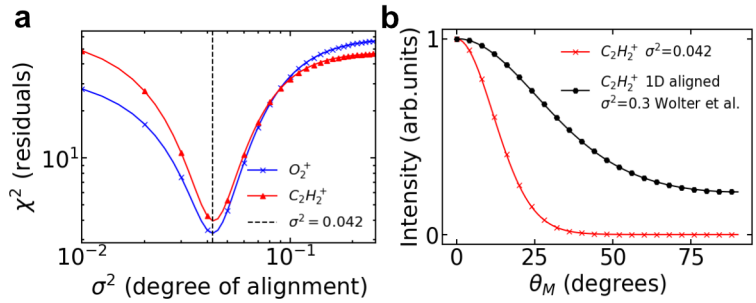

FIGURE 6.13: **Extracting the degree of alignment imprinted in the molecular backscattered interferences. a**. O_2 and C_2H_2 residuals as function of σ^2 for the best parameters Θ_0 and internuclear distance reported in Fig. 6.12. **b**. Alignment distribution corresponding to the best fit χ^2_{min} (red) compared to the 1D impulsive alignment distribution reported in [20, 44] (black).

interferences from multi-center atoms.

For OCS, particularly because we reported in Sec. 6.2 a bent structure, the molecular alignment distribution looks a bit more complex than the linear O_2 and C_2H_2 molecules to apply the same fitting routine as in the previous section. For example, one could define the molecular alignment distribution by referring a center of mass and its respective molecular frame angle. Or, as IAM is based on the independent atomic model, one can define the OCS molecular alignment distribution as a superposition of independent bond-length alignment distribution:

$$\rho(\beta) = \rho_{OC}(\beta) + \rho_{CS}(\beta) + \rho_{OS}(\beta) \tag{6.7}$$

where,

$$\rho_{OC}(\beta) = e^{\frac{-sin^2(\beta-\beta_{OC})}{2\sigma^2}}, \quad \rho_{CS}(\beta) = e^{\frac{-sin^2(\beta-\beta_{CS})}{2\sigma^2}}, \quad \rho_{OS}(\beta) = e^{\frac{-sin^2(\beta-\beta_{OS})}{2\sigma^2}} \tag{6.8}$$

In the appendix C, we explain how to overlap the different bond-length with the laser fields for an arbitrary geometry to show their contribution in the final calculated scattering cross section. For all cases illustrated in Fig. 6.14 **a**, we have used a 3D fitting routine with ranges defined as $R_{OC} = 0.9 - 1.4$ Å, $R_{CS} = 1.5 - 2.5$ Å and $\phi_{OCS} = 105 - 180\,^\circ$ with steps of 0.025 Å and 1.25°. The theoretical calculations that fit best the experimental results according to the four alignment distribution cases are plotted in Fig. 6.14 **b**.

Similar to C_2H_2 and O_2 (see Fig. 6.13), the isotropically-oriented molecules (case A, black solid line) and the one-dimensional averaged theoretical calculations (case B, red solid line) don´t really fit the experimental interferences (dashed blue). If we take into account a narrowed alignment distribution along with the two OC and CS bond axes (case C), the experimental MCF is well reproduced in the range q = 10-14 $Å^{-1}$. To have an understanding of the entire momentum transfer range (9-16.5 $Å^{-1}$), we had to include a third distribution along the unbound OS axis. Interestingly, we notice that the minima and maxima of these

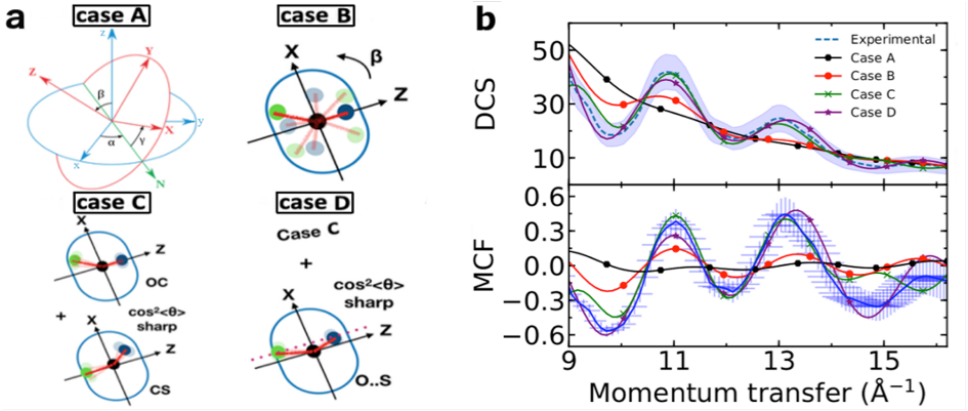

FIGURE 6.14: **Molecular orientation selectivity in OCS^+ LIED interferences.** **a**. Four cases of triatomic molecular alignment distributions $\rho(\Omega_L)$. Case A shows Euler averaging angles for randomly-oriented OCS. Case B shows a one-dimensional averaged distribution. Case C illustrates a one-dimensional alignment along two bond-lengths OC and CS. Case D represents case C plus another alignment distribution along the unbound O..S bond-length. For the two latter cases the degree of alignment is treated and weighted equally for the OC, CS and O..S bond-lengths. **b**. The four alignment cases which fit best the experimental OCS^+ DCS (see legend). **c**. The same four alignment cases which fit best the experimental OCS^+ MCF. The error-bars are defined by a poissonian distribution (vertical) and a momentum transfer error given by the detected momentum (horizontal).

four calculated distributions coincide with each other. For case D that fits best the experimental observations, we retrieve that same bent and assymetric structure (see appendix D) that we reported earlier in Sec. 6.2 when calculations were done for isotropic molecules without considering the amplitude factor.

6.4 Summary

As shown in Chap. 5, it is difficult to assign the temporal dynamics of LIED when using the full kinetic energy range from $2U_p$ and above. Yet, we can compare our LIED results with a chemistry dynamical calculation as shown in Sec. 6.2. A good agreement is found between theory and experiment revealing an asymmetric and bent OCS structure. Moreover, we present an alternative scheme "ZCP-LIED" which relies in a simpler and more accurate algorithm than the FT-LIED method limited by the bandwith and post-processing knowledge which highly depend on the number of bond-length to solve.

Another project conducted in parallel with the ZCP development was to revisit FABLES [153] or FT-LIED [43] and investigate aspects of the method that remained unexplained [127, 128, 145, 158]. For this, we re-analyzed the results found here [43] and here [145] using the conventional IAM model from gas-phase electron diffraction (GED) applications [6]. First, we show that including additional multiple returns in the calculations of the vector potential and rescattered

momentum lead to very similar results in the extraction of the DCS with the approximated single first long trajectory. Then, we analyzed three different targets O_2, C_2H_2, OCS and noticed that they all lead to the same conclusion: a selective oriented geometry is responsible for the oscillations found in the backscattered photoelectrons yield. Curiously, these findings seem to confirm a more general feature about wave diffraction since same results were found at PETRA III [160] flashing light [161] instead of electrons. Here is a quote from [161]:

"...When the de Broglie wavelength of the outgoing electron resolves the internuclear distance, i.e. the incoming photon and outgoing electron can 'see' the molecular structure, the random oscillation turns into the oriented curve...".

Therefore, it should be interesting to investigate backscattered LIED scattering cross-sections with impulsive molecular alignment techniques similar to the experimental results reported in [162], but deep inside the Mid-IR regime to have the required ponderomotive energy and deBroglie wavelength.

Chapter 7

Conclusions and Outlook

Strong fields Mid-IR (MIR) laser sources produced by OPCPA and delivering passive CEP-phase stability are shown to be promising tools for the investigation of ultrafast atomic and molecular spectroscopy. Furthermore, the high laser ponderomotive energy combined together with a high-repetition rate ($\approx$ 160 kHz) allows us to detect a large photoelectron kinetic energy range at a moderately low measurement acquisition time. A direct application of strong fields ionization is the elastic scattering of the returning electron wavepacket that provides information on the atomic and molecular properties. The main advantages of this table-top method are the coherent emission of photoelectrons and the ultrafast scale at which the electrons further drive back towards their own targets within low impact parameters $b \approx 0$. Additionally, the diffraction pattern can be measured in a full $4 - \pi$ solid angle and at a variety of different kinetic energies allowing for example the detection of backscattered electrons carrying high momentum transfer ($q \approx 14\,\text{Å}^{-1}$).

On the one hand, strong field dynamics offer a wide variety of exciting interference patterns that can be used to reveal information about the target structure, as demonstrated in Chap. 4. Due to the wavelength-scaling [32], "direct" photoelectrons are produced in a majority, several orders of difference compared to the scattered ones. Therefore, we have found a utility to those highly generated photoelectrons previously unexplored in the deep Mid-IR wavelength regime. Moreover, we introduced an empirical method that accurately retrieved a phase difference between two targets having the same binding energy but a different orbital parity. Similarly to [122], one could go beyond in the investigation of the fan-like structure, including non-adiabatic couplings. Then, it would be interesting to apply those similar measurements together with pump-probe techniques [163] to see if the phase would switch radically, or progressively, from one orbital parity to another in the vicinity of a conical intersection (degenerate states).

On the other hand, those strong field dynamics add more complexity in defining the rescattering time, showing an ambiguity in using models for characterizing LIED. To eliminate that ambiguity, we proposed in Chap. 5 a simple implementation to gate on the rescattering pathways, and hence, restored the subfemtoseconds intra-cycle temporal dynamics. The use of long-wavelength MIR laser fields is essential for clearly separating the different quantum pathways. As a future outlook, it may be interesting to add ellipticity in the two-color laser

waveform to create electrons with particular helicity left/right for the investigation of chiral objects [164, 165].

Alternatively, for molecular dynamics that arise at a larger time than one optical cycle (quasi Born-approximation), LIED has shown to be a robust tool capable of retrieving acetylene equilibrium bond-lengths within sub-angstroms resolution [20]. However, the method previously relied on the QRS model such that the diffraction patterns were investigated at different scattering angles but fixed scattering energy. Initially, the investigation of backscattered electrons providing high momentum transfer has been studied via the empirical FT-LIED method [43]. In Chap. 6, we provide a novel method based on the identification of critical points from the molecular interference terms that allows us to directly retrieve the OCS molecular structure from the two-dimensional photoelectron distribution and overcomes the challenges imposed by the Fourier LIED analysis. Moreover, we find that only a few zero-crossing points (ZCPs) are required to retrieve the molecular structure accurately. Using ZCP-LIED avoids complex retrieval algorithms, semi-classical analyses and ab initio calculations to retrieve structural information as is typically used in electron and X-ray diffraction. Our LIED results are compared with a chemistry dynamical calculation, and a good agreement is found between theory and experiment, revealing an asymmetric and bent OCS structure. Non-adiabatic dynamics take place due to the long enough pulse duration ($\approx$ 98 fs FWHM), enabling the linear-to-bent transition via the Renner-Teller effects [91]. Even though a small population is transferred to the excited state, our signal is dominated by the bent excited state for the ionization potential difference being 5.2 eV lower between the excited $2^1A'$ and $1^1\Sigma^+$ ground state.

Finally, in Sec. 6.3 we saw that the conventional IAM theoretical scattering cross-sections from the randomly-oriented target could not qualitatively reproduce the experimental backscatter LIED results. The same observations were mentioned in [166] using three different scattering models. In Sec. 6.3.3, we show that an agreement with conventional IAM calculations can be found considering a narrowed degree of alignment along the bond-length axes. Interestingly, in Sec. 6.3.4 when considering only one fixed geometry, we retrieve the same molecular structure (see appendix D for more details) than the one previously reported with the zero-crossing points method from isotropically distributed molecules. Moreover, we find that all four theoretical distributions presented in Fig. 6.14 have the same oscillation period as a function of the transfer momentum, which may explain why we retrieve the same molecular geometry within the different LIED analyses shown in this thesis.

However, we shall emphasize that the high molecular contrast factor embedded in backscattered LIED interferences allowed us to successfully retrieve the molecular structure within picometers accuracies given the low signal-to-noise ratio of those low impact parameter rescattering trajectories. Without the ReMi coincidence detection capabilities, backscatter LIED retrievals from gas-phase would probably fail. As a future outlook, it will be interesting to investigate the

backscatter LIED signal as a function of molecular alignment angle using impulsive alignment techniques in order to unravel the randomly to oriented transition observed in Sec. 6.3.3 and in [161] with Cohen-Fano interferences.

Appendix A

Ar two-color TDSE calculations, $I_{2\omega}/I_{\omega} = 1.00$, $\phi_{\omega/2\omega} = 1.35\pi$

Complementary time-of-flight TDSE analysis for Chap. 5.
Calculations were realized following the same grid parameters as in Chap.5 and with the two-color waveform linearly polarized shown in Fig. A.1 **a** for $I_{2\omega}/I_{\omega} = 1.00$ at $\phi_{\omega/2\omega} = 1.35\pi$. The photoelectron spectra (see panels **b-c**) can be split in two kinetic energy ranges made of even-order (middle-low-energy region) and odd-order returns (high-energy region). Classical trajectories are plotted on top of the TDSE-based yield which is integrated until it reaches a multiple of an opt. cyc., in the same representation as shown as in Fig. 5.5. In the kinetic energy range between the third and first return cut-off (see yellow and red lines in panel **b**), the signal starts rising after the long first returns, rendering the high-energy range $8.3 < E_k/U_p < 12$ suitable for LIED (as there is only one type of trajectoy).

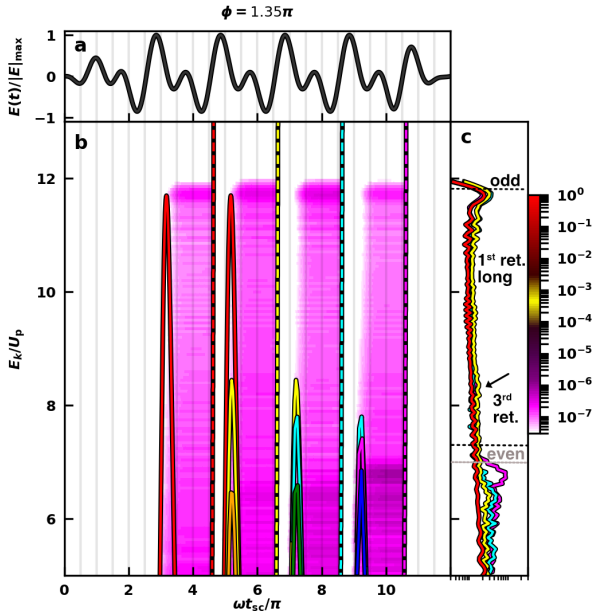

FIGURE A.1: **Single trajectory LIED information in two-color fields.** The shape of the laser pulse is shown in **a**. Laser parameters: $\lambda = 3.2\,\mu$m at $I_{\omega} = 6 \cdot 10^{13}\,\mathrm{W/cm^2}$, and $I_{2\omega} = 1.00 I_{\omega}$, $\phi_{\omega/2\omega} = 1.35\pi$. **b-c** Same captions and legends as in Fig. 5.5. The kinetic energy range is split within odd and even returns. The first and third return cut-off are separated well apart, rendering LIED applicable with those conditions.

Appendix B

OCS dissociative pathway

The photon-ion photon-ion coincidence (PiPiCo) as shown in Fig. B.1 **a** indicates that OCS^{2+} more likely decays to $OC^{+}+{}^{32}S^{+}$ **(1)** and its corresponding isotope $OC^{+}+{}^{34}S^{+}$ **(2)**. Another possible two-body breakup $O^{+}+C{}^{32}S^{+}$ **(3)** appears in the PiPiCo with lower intensity because C-O bond is much harder to break than C-S bond. In Fig. B.1 **b**, we extract the Micro-Channel-Plate (MCP) hit position of the correlated Time-of-Flight (ToF) indicating by channel **(1)** ($OC^{+}+{}^{32}S^{+}$). We also report a three-body breakup as shown by the correlated fragment O^{+} and ${}^{32}S^{+}$ **(4)**. Since we do not detect C^{+} fragments and/or OCS^{3+}, we attributed this decay to be the incomplete three-body breakup involving neutral C. After applying momentum sum conservation in between O^{+} and S^{+} detected fragment we could reconstruct the third particle 3D momentum and extract the corresponding Newton diagram as presented in Fig. B.1 **c**. In this plot, we study the vector correlation among fragments. The momenta are represented in molecular frame and S^{+} is chosen such that its momentum is defined by the x-axis as illustrated by the black arrow, while C and O^{+} particles momentum are located respectively by the lower and upper halves of the plot. The diagram is scaled and normalized by the S^{+} momentum length. As compared to previous triatomic molecules three-body breakup newton diagrams[167, 168, 169, 170], Fig. B.1 **c** clearly displays a molecular bending dissociation. A measurement of the bond angle ϕ_{OCS} can be read directly by integrating the distribution of O^{+} fragment with respect to S^{+} fragment. The angular distribution detected from the coulomb exploded channel **(4)** is plotted in Fig. B.1 **d**. Two tails are observed. One with a central angle of 145^{o} confirming similar bending to the results presented in Sec. 6.2 for OCS^{+}. While a broader distribution is also observed around 111^{o} and could be the consequence of a sequential fragmentation [167, 169, 170] (the molecule fragments in two steps, with S^{+} first and O^{+} and C latter). This second tail manifests a stronger binding along the O-C bond than the C-S bond supporting the two orders of magnitude found between channels **(1)** and **(3)**.

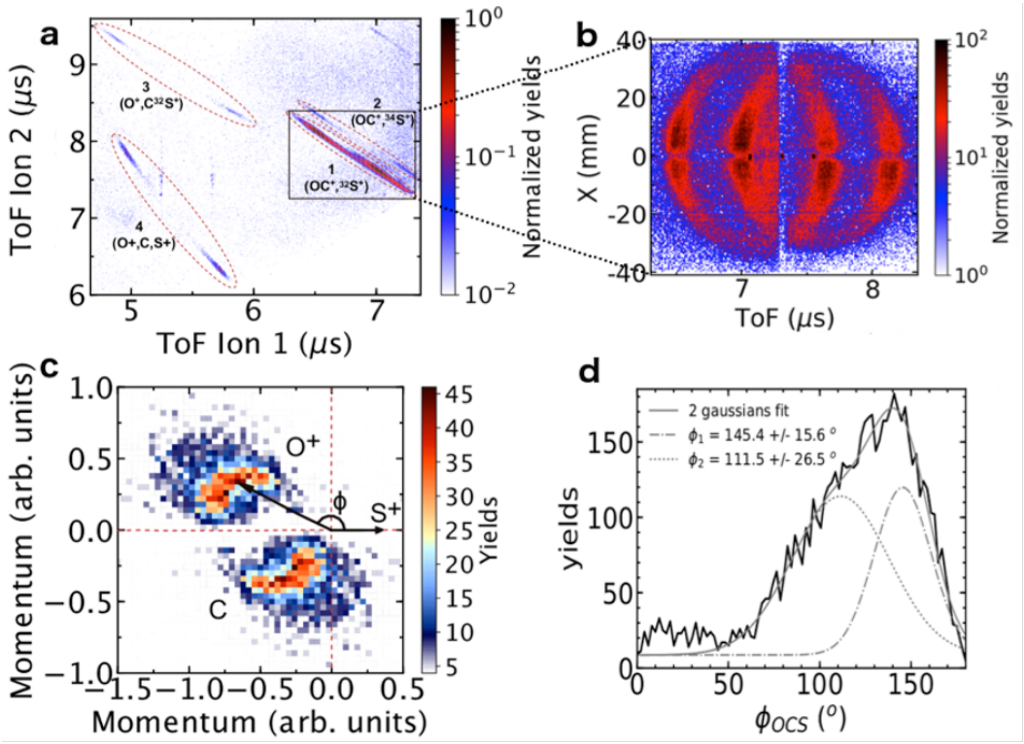

FIGURE B.1: **a**. Photon-ion photon-ion coincidence (PiPiCo) revealing different fragmentation pathways labelled as **(1)** for (OC^++$^{32}S^+$), **(2)** for (OC^++$^{34}S^+$), **(3)** for (O^++$C^{32}S^+$), **(4)** for (O^++C+$^{32}S^+$).**b**. Micro-Channel-Plate (MCP) hit position corresponding to the correlated Time-of-Flight (ToF) of channel **(1)**. **c**. Normalised S^+ Newton diagram for three-body fragmentation of OCS^{2+} corresponding to channel **(4)** from the possible pathways illustrated in **a**. S^+ is the momentum vector reference defined by the lower axis, positive left axis shows O^+ fragment direction while negative left axis represents neutral C direction. The momentum distribution is represented in the molecular frame where ϕ is the angle defined by the fragment distribution with respect to S^+. **d**. Angular distribution ϕ extracted from **c** in the dissociative pathway **(4)**.

Appendix C

Molecular bond axes projected into E-fields

In our calculations, we initially referred OC bond as being projected into Z-axis (laser pol. axis) before applying an active rotation and integrating over $\delta\beta$. Considering the alignment distribution presented in eq. 6.7, we have to defined in the calculations β_{OC}, β_{CS} and β_{OS} such that each of the molecular bonds overlap with the laser polarization during the integration over β. The weight of each molecular bond is equally treated in case D (see Fig. 6.14).

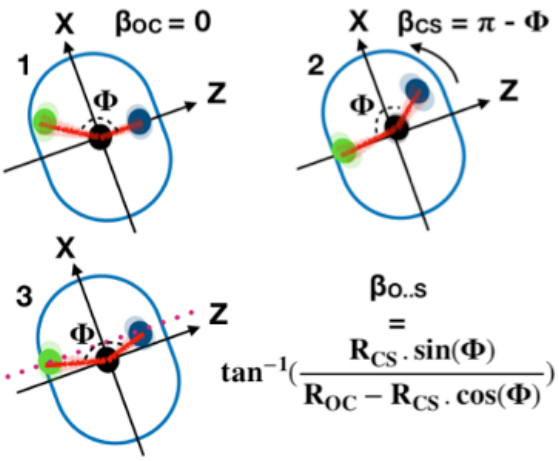

FIGURE C.1: Molecular bond-axes projected into E-fields. Sketch of the corresponding β_{OC}, β_{CS} and β_{OS} to set for an arbitrary OCS geometry.

Appendix D

OCS LIED results using conventional IAM calculations

In this retrieval of LIED, we use case scenario **D** as shown in Fig. 6.14 because they lead to better agreement with the experimental results. The MCFs are presented in Fig. D.1 **a** for the theoretical calculations which best fit the experiment (purple), for the left deviation MCF(q-δq) (orange), and the right deviation MCF(q+δq) (green), with $\delta q = 2 * \delta k_r$ δk_r being the detected momentum error. The results on the measured bond lengths and bond angle are displayed in Fig. D.1 **b**, by showing an ellipsoid representing a 100% deviation from χ^2_{min} found for MCF(q) (purple), MCF(q-δq) (orange) and MCF(q+δq) (green). We estimated the bond lengths and bond angle errors by taking the maximum overlap between those 3 ellipsoids which represents the measurment zone of confidence. We retrieve an OCS^+ structure within the experimental errors similar to those shown in Sec. 6.2: $R_{CO} = 1.06 \pm 0.05$Å, $R_{CS} = 1.66 \pm 0.07$Å and $\phi_{OCS^+} = 143 \pm 4^o$.

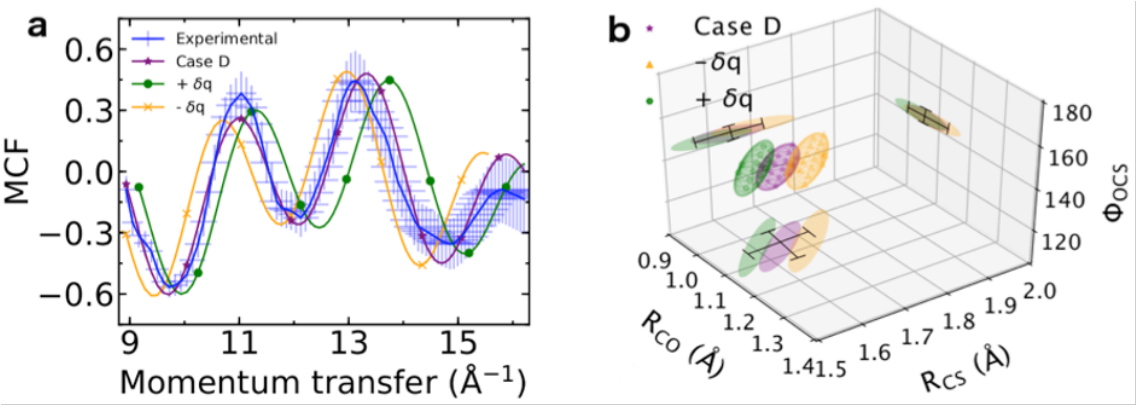

FIGURE D.1: **a**. Theoretical MCF which best fits the experimental MCF(q) (purple), MCF(q-δq) (orange) and MCF(q+δq) (green). **b**. Ellipsoids representing the 3D solutions with a 100% deviation from χ^2_{min} in MCF(q) (purple), MCF(q-δq) (orange) and MCF(q+δq) (green).

References

[1] W. Heisenberg, "Über den anschaulichen inhalt der quantentheoretischen kinematik und mechanik," *Z. Physik*, vol. 43, p. 172–198, Mar. 1927.

[2] J. Šponer, G. Bussi, M. Krepl, P. Banáš, S. Bottaro, R. A. Cunha, A. Gil-Ley, G. Pinamonti, S. Poblete, P. Jurečka, N. G. Walter, and M. Otyepka, "Rna structural dynamics as captured by molecular simulations: A comprehensive overview," *Chemical Reviews*, vol. 118, no. 8, pp. 4177–4338, 2018.

[3] Barty A., Boutet S., Bogan M. J., Hau-Riege S., Marchesini S., Sokolowski-Tinten K., Stojanovic N., Tobey R., Ehrke H., Cavalleri A., Düsterer S., Frank M., Bajt S., Woods B. W., Seibert M. M., Hajdu J., Treusch R., Chapman H. N., "Ultrafast singleshot diffraction imaging of nanoscale dynamics," *Nature Photonics*, vol. 2, no. 9, p. 578, 2008.

[4] P. Thibault, "X-ray diffraction microscopy," *Annual Review of Condensed Matter Physics*, vol. 1, pp. 237–255, 2010.

[5] P. van Cittert, "Die wahrscheinliche schwingungsverteilung in einer von einer lichtquelle direkt oder mittels einer linse beleuchteten ebene," *Physica*, vol. 1, no. 1, pp. 201–210, 1934.

[6] I. Hargittai and M. Hargittai, *Stereochemical Applications of Gas-Phase Electron Diffraction*. VCH, 1998.

[7] S. Manz, A. Casandruc, D. Zhang, Y. Zhong, R. Loch, A. Marx, T. Hasegawa, L. Liu, S. Bayesteh, H. Delsim-Hashemi, M. Hoffmann, M. Felber, M. Hachmann, F. Mayet, J. Hirscht, S. Keskin, M. Hada, S. Epp, K. Flöttmann, and R. Miller, "Mapping atomic motions with ultrabright electrons: towards fundamental limits in space-time resolution," *Faraday Discussion*, vol. 177, no. 467, 2015.

[8] S. Lahme, C. Kealhofer, F. Krausz, and P. Baum, "Femtosecond single-electron diffraction," *Struct. Dyn.*, vol. 1, no. 034303, 2014.

[9] G. Sciaini and R. J. D. Miller, "Femtosecond electron diffraction: heralding the era of atomically resolved dynamics," *Rep. Prog. Phys.*, vol. 74, no. 096101, 2011.

[10] Smirnova O., Mairesse Y., Patchkovskii S. et al., "High harmonic interferometry of multi-electron dynamics in molecules," *Nature*, vol. 460, pp. 972–977, 2009.

[11] Goulielmakis E., Loh ZH., Wirth A. et al., "Real-time observation of valence electron motion," *Nature*, vol. 466, pp. 739–743, 2010.

[12] S. Teichmann, F. Silva, S. Cousin, M. Hemmer, and J. Biegert, "0.5-kev soft x-ray attosecond continua," *Nature Communications*, vol. 7, no. 11493, 2015.

[13] Uiberacker M., Uphues T., Schultze M. et al., "Attosecond real-time observation of electron tunnelling in atoms," *Nature*, vol. 446, pp. 627–632, 2007.

[14] Sansone G., Kelkensberg F., Pérez-Torres J. et al., "Electron localization following attosecond molecular photoionization," *Nature*, vol. 465, pp. 763–766, 2010.

[15] S. Skruszewicz, J. Tiggesbäumker, K.-H. Meiwes-Broer, M. Arbeiter, Th. Fennel, and D. Bauer, "Two-color strong-field photoelectron spectroscopy and the phase of the phase," *Phys. Rev. Lett*, vol. 115, p. 043001, 2015.

[16] T. Zuo, A. D. Bandrauk, and P. B. Corkum, "Laser-induced electron diffraction: a new tool for probing ultrafast molecular dynamics," *Chem. Phys. Lett.*, no. 259, pp. 313–320, 1996.

[17] M. Lein, J. P. Marangos, and P. L. Knight, "Electron diffraction in above-threshold ionization of molecules," *Physical Review A*, vol. 66, no. 051404, 2002.

[18] M. Meckel, D. Comtois, D. Zeidler, a. Staudte, D. Pavicic, H. C. Bandulet, H. Pépin, J. C. Kieffer, R. Dörner, D. M. Villeneuve, and P. B. Corkum, "Laser-induced electron tunneling and diffraction.," *Science (New York, N.Y.)*, vol. 320, no. 5882, pp. 1478–82, 2008.

[19] C. I. Blaga, J. Xu, A. D. DiChiara, E. Sistrunk, K. Zhang, P. Agostini, T. a. Miller, L. F. DiMauro, and C. D. Lin, "Imaging ultrafast molecular dynamics with laser-induced electron diffraction.," *Nature*, vol. 483, no. 7388, pp. 194–7, 2012.

[20] M. Pullen, B. Wolter, A.-T. Le, M. Baudisch, M. Hemmer, A. Senftleben, C. Schroter, J. Ullrich, R. Moshammer, C. Lin, and J. Biegert, "Imaging an aligned polyatomic molecule with laser-induced electron diffraction," *Nature Communications*, vol. 6, p. 7262, 2015.

[21] H. Reiss, "Theoretical methods in quantum optics: S-matrix and keldysh techniques for strong-field processes," *Progress in Quantum Electronics*, vol. 16, no. 1, pp. 1–71, 1992.

[22] D. Bauer, *Computational Strong-field Quantum Dynamics: Intense Light-matter Interactions*. De Gruyter Textbook Series, Walter de Gruyter GmbH, 2017.

[23] K. Schafer, B. Yang, L. DiMauro, and K. Kulander, "Above threshold ionization beyond the high harmonic cutoff.," *Physical review letters*, vol. 70, no. 11, pp. 1599–1602, 1993.

[24] P. B. Corkum, "Plasma perspective on strong field multiphoton ionization," *Phys. Rev. Lett.*, vol. 71, pp. 1994–1997, Sep 1993.

[25] M. Lewenstein, P. Balcou, M. Y. Ivanov, A. L. Huillier, and P. Corkum, "Theory of high-harmonic generation by low-frequency laser fields," *Physical Review A*, vol. 49, no. 3, pp. 2117–2132, 1994.

[26] G. M. A. L'Huillier, L. A. Lompre and C. Manus, "Multiply charged ions formed by multiphoton absorption processes in the continuum," *Phys. Rev. Lett.*, vol. 48, no. 1814, 1982.

[27] G. M. A. L'Huillier, L. A. Lompre and C. Manus, "Multiply charged ions induced by multiphoton absorption in rare gases at 0.53 μm," *Phys. Rev. A*, vol. 27, no. 2503, 1983.

[28] D. N. Fittinghoff, P. R. Bolton, B. Chang, and K. C. Kulander, "Observation of nonsequential double ionization of helium with optical tunneling," *Phys. Rev. Lett.*, vol. 69, no. 2642, 1992.

[29] A. T. S Larochelle and S. L. Chin, "Non-sequential multiple ionization of rare gas atoms in a ti:sapphire laser field," *J. Phys. B: At. Mol. Opt. Phys.*, vol. 31, p. 1201–1214, 1998.

[30] C. Cornaggia and P. Hering, "Nonsequential double ionization of small molecules induced by a femtosecond laser field," *Phys. Rev. A*, vol. 62, no. 023403, 2000.

[31] M. Pullen, B. Wolter, X. Wang, X.-M. Tong, M. Sclafani, M. Baudisch, H. Pires, C. Schroter, J. Ullrich, T. Pfeifer, R. Moshammer, J. Eberly, and J. Biegert, "Transition from nonsequential to sequential double ionization in many-electron systems," *Physical Review A Review*, vol. 96, p. 33401, 2017.

[32] P. Colosimo, G. Doumy, C. I. Blaga, J. Wheeler, C. Hauri, F. Catoire, J. Tate, R. Chirla, a. M. March, G. G. Paulus, H. G. Muller, P. Agostini, and L. F. DiMauro, "Scaling strong-field interactions towards the classical limit," *Nature Physics*, vol. 4, pp. 386–389, 2008.

[33] D. Austin and J. Biegert, "Strong-field approximation for the wavelength scaling of high-harmonic generation," *Physical Review A*, vol. 86, pp. 1–7, 2012.

[34] J. Biegert, P. K. Bates, and O. Chalus, "New Mid-Infrared Light Sources," *IEEE Journal of Selected Topics in Quantum Electronics*, vol. 18, pp. 531–540, 2012.

[35] M. Hemmer, M. Baudisch, A. Thai, A. Couairon, and J. Biegert, "Self-compression to sub-3-cycle duration of mid-infrared optical pulses in dielectrics," *Optics Express*, vol. 21, p. 28095, 2013.

[36] R. Moshammer, M. Unverzagt, W. Schmitt, J. Ullrich, and H. Schmidt-Böcking, "A 4π recoil-ion electron momentum analyzer: A high-resolution "microscope" for the investigation of the dynamics of atomic, molecular and nuclear reactions," *Nuclear Instruments and Methods in Physics Research Section B: Beam Interactions with Materials and Atoms*, vol. 108, no. 4, pp. 425–445, 1996.

[37] J. Ullrich, R. Moshammer, and A. Dorn, "Recoil-ion and electron momentum spectroscopy : reaction-microscopes," *Reports on Progress in Physics*, vol. 66, pp. 1463–1545, 2003.

[38] B. Wolter, M. G. Pullen, M. Baudisch, M. Sclafani, M. Hemmer, A. Senftleben, C. D. Schröter, J. Ullrich, R. Moshammer, and J. Biegert, "Strong-field physics with mid-ir fields," *Physical Review X*, vol. 5, no. 021034, 2015.

[39] M. Göppert-Mayer *Ann. Phys., Lpz.*, vol. 9, no. 273-94, 1931.

[40] A. Ludwig,J. Maurer,B. W. Mayer,C. R. Phillips, L. Gallmann, and U. Keller, "Breakdown of the dipole approximation in strong-field ionization," *Phys. Rev. Lett.*, vol. 113, no. 243001, 2014.

[41] H. Reiss, "The tunnelling model of laser-induced ionization and its failure at low frequencies," *J. Phys. B: At. Mol. Opt. Phys.*, vol. 47, no. 204006, 2014.

[42] C. D. Lin, A.-T. Le, Z. Chen, T. Morishita, and R. Lucchese, "Strong-field rescattering physics—self-imaging of a molecule by its own electrons," vol. 43, p. 122001, jun 2010.

[43] M. Pullen, B. Wolter, A.-T. Le, M. Baudisch, M. Sclafani, H. Pires, C. Schroter, J. Ullrich, R. Moshammer, T. Pfeifer, C. Lin, and J. Biegert, "Influence of orbital symmetry on diffraction imaging with rescattering electron wave packets," *Nature Communications*, vol. 7, p. 11922, 2016.

[44] B. Wolter, M. G. Pullen, A.-T. Le, M. Baudisch, K. Doblhoff-Dier, A. Senftleben, M. Hemmer, C. D. Schröter, J. Ullrich, T. Pfeifer, R. Moshammer, S. Gräfe, O. Vendrell, C. D. Lin, and J. Biegert, "Ultrafast electron diffraction imaging of bond breaking in di-ionized acetylene," *Science*, vol. 354, p. 6310, 2017.

[45] R. Wiehle, B. Witzel, V. Schyja, H. Helm, and E. Cormier, "Strong-field photoionization of argon: A comparison between experiment and the sae approximation," *Journal of Modern Optics*, vol. 50, no. 3-4, pp. 451–459, 2003.

[46] T.-M. Yan, S. V. Popruzhenko, M. J. J. Vrakking, and D. Bauer, "Low-energy structures in strong field ionization revealed by quantum orbits," *Phys. Rev. Lett.*, vol. 105, p. 253002, Dec 2010.

[47] Y. Huismans, A. Rouzée, A. Gijsbertsen, J. H. Jungmann, A. S. Smolkowska, P. S. W. M. Logman, F. Lépine, C. Cauchy, S. Zamith, T. Marchenko, J. M. Bakker, G. Berden, B. Redlich, A. F. G. van der Meer, H. G. Muller, W. Vermin, K. J. Schafer, M. Spanner, M. Y. Ivanov, O. Smirnova, D. Bauer, S. V. Popruzhenko, and M. J. J. Vrakking, "Time-resolved holography with photoelectrons," *Science*, vol. 331, no. 6013, pp. 61–64, 2011.

[48] C. Hofmann, A. S. Landsman, A. Zielinski, C. Cirelli, T. Zimmermann, A. Scrinzi, and U. Keller, "Interpreting electron-momentum distributions and nonadiabaticity in strong-field ionization," *Phys. Rev. A*, vol. 90, p. 043406, Oct 2014.

[49] M. Lucchini, A. Ludwig, T. Zimmermann, L. Kasmi, J. Herrmann, A. Scrinzi, A. S. Landsman, L. Gallmann, and U. Keller, "Anisotropic emission in quantum-beat spectroscopy of helium excited states," *Phys. Rev. A*, vol. 91, p. 063406, Jun 2015.

[50] S.-F. Zhao, A.-T. Le, C. Jin, X. Wang, and C. D. Lin, "Analytical model for calibrating laser intensity in strong-field-ionization experiments," *Phys. Rev. A*, vol. 93, p. 023413, Feb 2016.

[51] R. Reiff, T. Joyce, A. Jaroń-Becker, and A. Becker, "Single-active electron calculations of high-order harmonic generation from valence shells in atoms for quantitative comparison with TDDFT calculations," vol. 4, p. 065011, jun 2020.

[52] L. Tao and A. Scrinzi, "Photo-electron momentum spectra from minimal volumes: the time-dependent surface flux method," *New Journal of Physics*, vol. 14, p. 013021, Jan. 2012.

[53] L. V. Keldysh, "Ionization in the field of a strong electromagnetic wave," *Zh. Eksperim. i Teor. Fiz.*, vol. 47, 11 1964.

[54] F. H. M. Faisal, "Multiple absorption of laser photons by atoms," vol. 6, pp. L89–L92, apr 1973.

[55] H. R. Reiss, "Effect of an intense electromagnetic field on a weakly bound system," *Phys. Rev. A*, vol. 22, pp. 1786–1813, Nov 1980.

[56] W. Becker and F. Grasbon and R. Kopold and D.B. Milošević and G.G. Paulus and H. Walther, "Above-threshold ionization: From classical features to quantum effects," in *Advances In Atomic, Molecular, and Optical Physics*, pp. 35–98, Elsevier, 2002.

[57] D. B. Milošević, G. G. Paulus, D. Bauer, and W. Becker, "Above-threshold ionization by few-cycle pulses," vol. 39, pp. R203–R262, jul 2006.

[58] T. Kjeldsen, *Wave packet dynamics studied by ab initio methods*. PhD thesis, Department of Physics and Astronomy, University of Arhus, 2007.

[59] V. Mosert and D. Bauer, "Photoelectron spectra with qprop and t-surff," *Computer Physics Communications*, vol. 207, pp. 452–463, 2016.

[60] A. D. Bandrauk, F. Fillion-Gourdeau, and E. Lorin, "Atoms and molecules in intense laser fields: gauge invariance of theory and models," *Journal of Physics B: Atomic, Molecular and Optical Physics*, vol. 46, p. 153001, jul 2013.

[61] J. Sakurai, *Modern Quantum Mechanics*. Addison-Wesley Pub. Co, 1968.

[62] R. Kopold, *Atomare Ionisationsdynamik in starken Laserfeldern*. PhD thesis, Technische Universitat Munchen, 2001.

[63] H. Kleinert, *Path Integrals in Quantum Mechanics, Statistics, Polymer Physics, and Financial Markets*. WORLD SCIENTIFIC, 5th ed., 2009.

[64] A. Nayak, M. Dumergue, S. Kühn, S. Mondal, T. Csizmadia, N. Harshitha, M. Füle, M. Upadhyay Kahaly, B. Farkas, B. Major, V. Szaszkó-Bogár, P. Földi, S. Majorosi, N. Tsatrafyllis, E. Skantzakis, L. Neoričić, M. Shirozhan, G. Vampa, K. Varjú, P. Tzallas, G. Sansone, D. Charalambidis, and S. Kahaly, "Saddle point approaches in strong field physics and generation of attosecond pulses," *Physics Reports*, vol. 833, pp. 1–52, 2019. Saddle point approaches in strong field physics and generation of attosecond pulses.

[65] O. Smirnova and M. Ivanov, *Multielectron High Harmonic Generation: Simple Man on a Complex Plane*, ch. 7, pp. 201–256. John Wiley and Sons, Ltd, 2014.

[66] B. Wolter, C. Lemell, M. Baudisch, M. G. Pullen, X.-M. Tong, M. Hemmer, A. Senftleben, C. D. Schröter, J. Ullrich, R. Moshammer, J. Biegert, and J. Burgdörfer, "Formation of very-low-energy states crossing the ionization threshold of argon atoms in strong mid-infrared fields," *Phys. Rev. A*, vol. 90, p. 063424, Dec 2014.

[67] J. Daněk, M. Klaiber, K. Z. Hatsagortsyan, C. H. Keitel, B. Willenberg, J. Maurer, B. W. Mayer, C. R. Phillips, L. Gallmann, and U. Keller, "Interplay between coulomb-focusing and non-dipole effects in strong-field ionization with elliptical polarization," vol. 51, p. 114001, may 2018.

[68] X. Hao, Y. Bai, X. Zhao, C. Li, J. Zhang, J. Wang, W. Li, C. Wang, W. Quan, X. Liu, Z. Shu, M. Liu, and J. Chen, "Effect of coulomb field on laser-induced ultrafast imaging methods," *Phys. Rev. A*, vol. 101, p. 051401, May 2020.

[69] M. Li, J.-W. Geng, H. Liu, Y. Deng, C. Wu, L.-Y. Peng, Q. Gong, and Y. Liu, "Classical-quantum correspondence for above-threshold ionization," *Phys. Rev. Lett.*, vol. 112, p. 113002, Mar 2014.

[70] N. I. Shvetsov-Shilovski, M. Lein, L. B. Madsen, E. Räsänen, C. Lemell, J. Burgdörfer, D. G. Arbó, and K. Tőkési, "Semiclassical two-step model for strong-field ionization," *Phys. Rev. A*, vol. 94, p. 013415, Jul 2016.

[71] C. D. Lin, A.-T. Le, C. Jin, and H. Wei, *Attosecond and Strong-Field Physics: Principles and Applications*. Cambridge University Press, 2018.

[72] V. Tulsky and D. Bauer, "Qprop with faster calculation of photoelectron spectra," *Computer Physics Communications*, vol. 251, p. 107098, June 2020.

[73] Porat, G., Alon, G., Rozen, S. et al., "Attosecond time-resolved photoelectron holography," *Nat Commun*, vol. 9, p. 2805, 2018.

[74] F. Rotermund, V. Petrov, F. Noack, M. Wittmann, and G. Korn, "Laser-diode-seeded operation of a femtosecond optical parametric amplifier with mgo:linbo3 and generation of 5-cycle pulses near 3 µm," *J. Opt. Soc. Am. B*, vol. 16, pp. 1539–1545, Sep 1999.

[75] O. Chalus, P. Bates, and J. Biegert, "Design and simulation of few-cycle optical parametric chirped pulse amplification at mid-ir wavelengths," *Opt. Express*, vol. 16, pp. 21297–21304, Dec 2008.

[76] R. W. Boyd, *Nonlinear Optics, 3rd ed.* 2008.

[77] D. Strickland and G. Mourou, "Compression of amplified chirped optical pulses," *Optics Communications*, vol. 56, no. 3, pp. 219–221, 1985.

[78] O. Chalus, P. K. Bates, M. Smolarski, and J. Biegert, "Mid-ir short-pulse opcpa with micro-joule energy at 100khz," *Opt. Express*, vol. 17, pp. 3587–3594, Mar 2009.

[79] U. Elu, M. Baudisch, H. Pires, F. Tani, M. H. Frosz, F. Köttig, A. Ermolov, P. S. J. Russell, and J. Biegert, "High average power and single-cycle pulses from a mid-IR optical parametric chirped pulse amplifier," *Optica*, vol. 4, no. 9, pp. 1024–1029, 2017.

[80] A. Dubietis, G. Jonušauskas, and A. Piskarskas, "Powerful femtosecond pulse generation by chirped and stretched pulse parametric amplification in bbo crystal," *Optics Communications*, vol. 88, no. 4, pp. 437–440, 1992.

[81] I. Ross, P. Matousek, M. Towrie, A. Langley, and J. Collier, "The prospects for ultrashort pulse duration and ultrahigh intensity using optical parametric chirped pulse amplifiers," *Optics Communications*, vol. 144, no. 1, pp. 125–133, 1997.

[82] T. Fuji, N. Ishii, C. Y. Teisset, X. Gu, T. Metzger, A. Baltuska, N. Forget, D. Kaplan, A. Galvanauskas, and F. Krausz, "Parametric amplification of few-cycle carrier-envelope phase-stable pulses at 2.1 μm," *Opt. Lett.*, vol. 31, pp. 1103–1105, Apr 2006.

[83] N. Thiré, R. Maksimenka, B. Kiss, C. Ferchaud, G. Gitzinger, T. Pinoteau, H. Jousselin, S. Jarosch, P. Bizouard, V. D. Pietro, E. Cormier, K. Osvay, and N. Forget, "Highly stable, 15 w, few-cycle, 65 mrad cep-noise mid-ir opcpa for statistical physics," *Opt. Express*, vol. 26, pp. 26907–26915, Oct 2018.

[84] P. Uebel, M. C. Günendi, M. H. Frosz, G. Ahmed, N. N. Edavalath, J.-M. Ménard, and P. S. Russell, "Broadband robustly single-mode hollow-core pcf by resonant filtering of higher-order modes," *Opt. Lett.*, vol. 41, pp. 1961–1964, May 2016.

[85] R. Dörner, V. Mergel, O. Jagutzki, L. Spielberger, J. Ullrich, R. Moshammer, and H. Schmidt-Böcking, "Cold target recoil ion momentum spectroscopy: a 'momentum microscope' to view atomic collision dynamics," *Physics Reports*, vol. 330, no. 2-3, pp. 95–192, 2000.

[86] N. Camus, *Non-sequential double ionization of atoms with phase-controlled ultrashort laser pulses*. PhD thesis, Ruperto-Carola-University of Heidelberg, Germany, 2013.

[87] A. Fischer, *Dissociative Photoionization of Molecular Hydrogen*. PhD thesis, Ruperto-Carola-University of Heidelberg, Germanyen, 2015.

[88] B. Wolter, *Electron re-collision dynamics in strong mid-IR fields for diffraction imaging of molecular structure and its fragmentation*. PhD thesis, ICFO - Institut de Ciències Fotòniques - UPC - Universitat Politècnica de Catalunya, 2017.

[89] D. R. Miller, *"Free Jet Sources," in Atomic and Molecular Beam Methods*. G. Scoles eds., vol. 14-82, chap. 2, (Oxford University Press, 1988).

[90] A. Senftleben, *Kinematically complete study on electron impact ionisation of aligned hydrogen molecules*. PhD thesis, Ruperto-Carola-University of Heidelberg, Germanyen, 2009.

[91] K. Amini, M. Sclafani, T. Steinle, A.-T. Le, A. Sanchez, C. Müller, J. Steinmetzer, L. Yue, J.-R. Martínez Saavedra, M. Hemmer, M. Lewenstein, R. Moshammer, T. Pfeifer, M. G. Pullen, J. Ullrich, B. Wolter, R. Moszynski, F. J. García de Abajo, C. D. Lin, S. Gräfe, and J. Biegert, "Imaging the renner–teller effect using laser-induced electron diffraction," *Proceedings of the National Academy of Sciences*, vol. 116, no. 17, pp. 8173–8177, 2019.

[92] J. Adamczewski, M. Al-Turany, D. Bertini, H. Essel, M. Hemberger, N. Kurz, and M. Richter, "Go4 multitasking class library with root," *IEEE Transactions on Nuclear Science*, vol. 49, no. 2, pp. 521–524, 2002.

[93] L. Fechner, *High resolution experiments on strong-field ionization of atoms and molecules: test of tunneling theory, the role of doubly excited states, and channel-selective electron spectra*. PhD thesis, Ruperto-Carola-University of Heidelberg, Germanyen, 2014.

[94] T. Brabec, M. Y. Ivanov, and P. B. Corkum, "Coulomb focusing in intense field atomic processes," *Phys. Rev. A*, vol. 54, pp. R2551–R2554, Oct 1996.

[95] Blaga, C., Catoire, F., Colosimo, P. et al, "Strong-field photoionization revisited," *Nature Phys.*, vol. 5, pp. 335–338, 2009.

[96] W. Quan, Z. Lin, M. Wu, H. Kang, H. Liu, X. Liu, J. Chen, J. Liu, X. T. He, S. G. Chen, H. Xiong, L. Guo, H. Xu, Y. Fu, Y. Cheng, and Z. Z. Xu, "Classical aspects in above-threshold ionization with a midinfrared strong laser field," *Phys. Rev. Lett.*, vol. 103, p. 093001, Aug 2009.

[97] Lemell, C., Dimitriou, K. I., Arbó, D. G., Tong, X.-M., Kartashov, D., Burgdörfer, J., and Gräfe, S., "Low-energy peak structure in strong-field ionization by mid-infrared laser pulses," *EPJ Web of Conferences*, vol. 41, p. 02016, 2013.

[98] L. Guo, S. S. Han, X. Liu, Y. Cheng, Z. Z. Xu, J. Fan, J. Chen, S. G. Chen, W. Becker, C. I. Blaga, A. D. DiChiara, E. Sistrunk, P. Agostini, and L. F. DiMauro, "Scaling of the low-energy structure in above-threshold ionization in the tunneling regime: Theory and experiment," *Phys. Rev. Lett.*, vol. 110, p. 013001, Jan 2013.

[99] S. A. Kelvich, W. Becker, and S. P. Goreslavski, "Coulomb focusing and defocusing in above-threshold-ionization spectra produced by strong mid-ir laser pulses," *Phys. Rev. A*, vol. 93, p. 033411, Mar 2016.

[100] G. G. Paulus, F. Grasbon, A. Dreischuh, H. Walther, R. Kopold, and W. Becker, "Above-threshold ionization by an elliptically polarized field: Interplay between electronic quantum trajectories," *Phys. Rev. Lett.*, vol. 84, pp. 3791–3794, Apr 2000.

[101] M. Spanner, O. Smirnova, P. B. Corkum, and M. Y. Ivanov, "Reading diffraction images in strong field ionization of diatomic molecules," vol. 37, pp. L243–L250, may 2004.

[102] R. Gopal, K. Simeonidis, R. Moshammer, T. Ergler, M. Dürr, M. Kurka, K.-U. Kühnel, S. Tschuch, C.-D. Schröter, D. Bauer, J. Ullrich, A. Rudenko, O. Herrwerth, T. Uphues, M. Schultze, E. Goulielmakis, M. Uiberacker, M. Lezius, and M. F. Kling, "Three-dimensional momentum imaging of electron wave packet interference in few-cycle laser pulses," *Phys. Rev. Lett.*, vol. 103, p. 053001, Jul 2009.

[103] X.-B. Bian, Y. Huismans, O. Smirnova, K.-J. Yuan, M. J. J. Vrakking, and A. D. Bandrauk, "Subcycle interference dynamics of time-resolved photoelectron holography with midinfrared laser pulses," *Phys. Rev. A*, vol. 84, p. 043420, Oct 2011.

[104] S. Popruzhenko and D. Bauer, "Strong field approximation for systems with coulomb interaction," *Journal of Modern Optics*, vol. 55, no. 16, pp. 2573–2589, 2008.

[105] T.-M. Yan and D. Bauer, "Sub-barrier coulomb effects on the interference pattern in tunneling-ionization photoelectron spectra," *Phys. Rev. A*, vol. 86, p. 053403, Nov 2012.

[106] J. Kaushal and O. Smirnova, "Nonadiabatic coulomb effects in strong-field ionization in circularly polarized laser fields," *Phys. Rev. A*, vol. 88, p. 013421, Jul 2013.

[107] E. Pisanty and M. Ivanov, "Slalom in complex time: Emergence of low-energy structures in tunnel ionization via complex-time contours," *Phys. Rev. A*, vol. 93, p. 043408, Apr 2016.

[108] X.-Y. Lai, C. Poli, H. Schomerus, and C. F. d. M. Faria, "Influence of the coulomb potential on above-threshold ionization: A quantum-orbit analysis beyond the strong-field approximation," *Phys. Rev. A*, vol. 92, p. 043407, Oct 2015.

[109] A. S. Maxwell and C. F. de Morisson Faria, "Coulomb-free and coulomb-distorted recolliding quantum orbits in photoelectron holography," *Journal of Physics B: Atomic, Molecular and Optical Physics*, vol. 51, p. 124001, may 2018.

[110] A. S. Maxwell, S. V. Popruzhenko, and C. F. d. M. Faria, "Treating branch cuts in quantum trajectory models for photoelectron holography," *Phys. Rev. A*, vol. 98, p. 063423, Dec 2018.

[111] N. Werby, A. S. Maxwell, R. Forbes, P. H. Bucksbaum, and C. F. d. M. Faria, "Dissecting subcycle interference in photoelectron holography," *Phys. Rev. A*, vol. 104, p. 013109, Jul 2021.

[112] L. Yue and L. B. Madsen, "Inter- and intracycle interference effects in strong-field dissociative ionization," *Phys. Rev. A*, vol. 93, p. 031401, Mar 2016.

[113] S. D. López and D. G. Arbó, "Holographic interference in atomic photoionization from a semiclassical standpoint," *Phys. Rev. A*, vol. 100, p. 023419, Aug 2019.

[114] A. S. Maxwell, A. Al-Jawahiry, T. Das, and C. F. d. M. Faria, "Coulomb-corrected quantum interference in above-threshold ionization: Working towards multitrajectory electron holography," *Phys. Rev. A*, vol. 96, p. 023420, Aug 2017.

[115] D. Bauer, D. B. Milošević, and W. Becker, "Strong-field approximation for intense-laser–atom processes: The choice of gauge," *Phys. Rev. A*, vol. 72, p. 023415, Aug 2005.

[116] S. Brennecke, N. Eicke, and M. Lein, "Gouy's phase anomaly in electron waves produced by strong-field ionization," *Phys. Rev. Lett.*, vol. 124, p. 153202, Apr 2020.

[117] M. Klaiber, E. Yakaboylu, and K. Z. Hatsagortsyan, "Above-threshold ionization with highly charged ions in superstrong laser fields. i. coulomb-corrected strong-field approximation," *Phys. Rev. A*, vol. 87, p. 023417, Feb 2013.

[118] A. Rudenko, K. Zrost, C. D. Schröter, V. L. B. de Jesus, B. Feuerstein, R. Moshammer, and J. Ullrich, "Resonant structures in the low-energy electron continuum for single ionization of atoms in the tunnelling regime," *Journal of Physics B: Atomic, Molecular and Optical Physics*, vol. 37, pp. L407–L413, dec 2004.

[119] D. G. Arbó, S. Yoshida, E. Persson, K. I. Dimitriou, and J. Burgdörfer, "Interference oscillations in the angular distribution of laser-ionized electrons near ionization threshold," *Phys. Rev. Lett.*, vol. 96, p. 143003, Apr 2006.

[120] H. Kang, A. S. Maxwell, D. Trabert, X. Lai, S. Eckart, M. Kunitski, M. Schöffler, T. Jahnke, X. Bian, R. Dörner, and C. F. d. M. Faria, "Holographic detection of parity in atomic and molecular orbitals," *Phys. Rev. A*, vol. 102, p. 013109, Jul 2020.

[121] V. A. Tulsky and D. Bauer, "Numerical time-of-flight analysis of the strong-field photoeffect," *Physical Review Research*, vol. 2, no. 4, p. 043083, 2020.

[122] X. Xie, S. Roither, D. Kartashov, E. Persson, D. G. Arbó, L. Zhang, S. Gräfe, M. S. Schöffler, J. Burgdörfer, A. Baltuška, and M. Kitzler, "Attosecond probe of valence-electron wave packets by subcycle sculpted laser fields," *Phys. Rev. Lett.*, vol. 108, p. 193004, May 2012.

[123] M. G. Pullen, J. Dura, B. Wolter, M. Baudisch, M. Hemmer, N. Camus, A. Senftleben, C. D. Schroeter, R. Moshammer, J. Ullrich, and J. Biegert, "Kinematically complete measurements of strong field ionization with mid-IR pulses," *Journal of Physics B: Atomic, Molecular and Optical Physics*, vol. 47, p. 204010, oct 2014.

[124] A. Ferré, A. E. Boguslavskiy, M. Dagan, V. Blanchet, B. D. Bruner, F. Burgy, A. Camper, D. Descamps, B. Fabre, N. Fedorov, J. Gaudin, G. Geoffroy, J. Mikosch, S. Patchkovskii, S. Petit, T. Ruchon, H. Soifer, D. Staedter, I. Wilkinson, A. Stolow, N. Dudovich, and Y. Mairesse, "Multi-channel electronic and vibrational dynamics in polyatomic resonant high-order harmonic generation," *Nature Communications*, vol. 6, p. 5952, Jan 2015.

[125] A. S. Maxwell, C. F. d. M. Faria, X. Lai, R. Sun, and X. Liu, "Spiral-like holographic structures: Unwinding interference carpets of coulomb-distorted orbits in strong-field ionization," *Phys. Rev. A*, vol. 102, p. 033111, Sep 2020.

[126] J.-L. Bégin, M. Alsaawy, and R. Bhardwaj, "Chiral discrimination by recollision enhanced femtosecond laser mass spectrometry," *Scientific Reports*, vol. 10, p. 14074, Aug 2020.

[127] X. Liu, K. Amini, T. Steinle, A. Sanchez, M. Shaikh, B. Belsa, J. Steinmetzer, A.-T. Le, R. Moshammer, T. Pfeifer, J. Ullrich, R. Moszynski, C. D. Lin, S. Gräfe, and J. Biegert, "Imaging an isolated water molecule using a single electron wave packet," *The Journal of Chemical Physics*, vol. 151, no. 2, p. 024306, 2019.

[128] B. Belsa, K. Amini, X. Liu, A. Sanchez, T. Steinle, J. Steinmetzer, A. T. Le, R. Moshammer, T. Pfeifer, J. Ullrich, R. Moszynski, C. D. Lin, S. Gräfe, and J. Biegert, "Laser-induced electron diffraction of the ultrafast umbrella motion in ammonia," *Structural Dynamics*, vol. 8, no. 1, p. 014301, 2021.

[129] Z. Chen, A.-T. Le, T. Morishita, and C. D. Lin, "Quantitative rescattering theory for laser-induced high-energy plateau photoelectron spectra," *Phys. Rev. A*, vol. 79, p. 033409, Mar 2009.

[130] D. W. Schumacher, F. Weihe, H. G. Muller, and P. H. Bucksbaum, "Phase dependence of intense field ionization: A study using two colors," *Phys. Rev. Lett.*, vol. 73, pp. 1344–1347, Sep 1994.

[131] D. Würzler, S. Skruszewicz, A. M. Sayler, D. Zille, M. Möller, P. Wustelt, Y. Zhang, J. Tiggesbäumker, and G. G. Paulus, "Accurate retrieval of ionization times by means of the phase-of-the-phase spectroscopy, and its limits," *Phys. Rev. A*, vol. 101, p. 033416, Mar 2020.

[132] O. G. S. V. e. a. Pedatzur, O., "Attosecond tunnelling interferometry," *Nature Phys.*, vol. 11, pp. 815–819.

[133] B. D. Bruner, Z. Mašín, M. Negro, F. Morales, D. Brambila, M. Devetta, D. Faccialà, A. G. Harvey, M. Ivanov, Y. Mairesse, S. Patchkovskii, V. Serbinenko, H. Soifer, S. Stagira, C. Vozzi, N. Dudovich, and O. Smirnova, "Multidimensional high harmonic spectroscopy of polyatomic molecules: detecting sub-cycle laser-driven hole dynamics upon ionization in strong mid-ir laser fields," *Faraday Discuss.*, vol. 194, pp. 369–405, 2016.

[134] G. Orenstein, O. Pedatzur, A. J. Uzan, B. D. Bruner, Y. Mairesse, and N. Dudovich, "Isolating strong-field dynamics in molecular systems," *Phys. Rev. A*, vol. 95, p. 051401, May 2017.

[135] Gal Orenstein and Ayelet Julie Uzan and Sagie Gadasi and Talya Arusi-Parpar and Michael Krüger and Raluca Cireasa and Barry D. Bruner and Nirit Dudovich, "Shaping electron-hole trajectories for solid-state high harmonic generation control," *Opt. Express*, vol. 27, pp. 37835–37845, Dec 2019.

[136] Uzan, A.J., Soifer, H., Pedatzur, O. et al., "Spatial molecular interferometry via multidimensional high-harmonic spectroscopy.," *Nature Photonics*, vol. 14, pp. 188–194.

[137] Uzan, A.J., Orenstein, G., Jiménez-Galán, Á. et al., "Attosecond spectral singularities in solid-state high-harmonic generation," *Nature Photonics*, vol. 14, pp. 183–187.

[138] L. F. D. Mauro and P. Agostini, *Ionization Dynamics in Strong Laser Fields*, vol. 35. Advances in Atomic, Molecular and Optical Physics, 1995.

[139] M. Baudisch, B. Wolter, M. Pullen, M. Hemmer, and J. Biegert, "High power multi-color OPCPA source with simultaneous femtosecond deep-UV to mid-IR outputs," *Optics letters*, vol. 41, no. 15, pp. 3583–3586, 2016.

[140] A. M. Perelomov, V. S. Popov, and M. V. Terentev, "Ionization of atoms in an alternating electric field," *Sov. Phys. JETP*, vol. 23, no. 5, p. 924, 1966.

[141] N. B. Delone and V. P. Krainov, "Tunneling and barrier-suppression ionization of atoms and ions in a laser radiation field," *Physics - Uspekhi*, vol. 41, pp. 469–485, 1998.

[142] D. Ray, Z. Chen, S. De, W. Cao, I. V. Litvinyuk, A. T. Le, C. D. Lin, M. F. Kling, and C. L. Cocke, "Momentum spectra of electrons rescattered from rare-gas targets following their extraction by one- and two-color femtosecond laser pulses," *Physical Review A*, vol. 83, Jan. 2011.

[143] G. G. Paulus, W. Becker, W. Nicklich, and H. Walther, "Rescattering effects in above-threshold ionization: a classical model," *Journal of Physics B: Atomic, Molecular and Optical Physics*, vol. 27, pp. L703–L708, Nov. 1994.

[144] A. M. Ermolaev, I. V. Puzynin, A. V. Selin, and S. I. Vinitsky, "Integral boundary conditions for the time-dependent Schrödinger equation: Atom in a laser field," *Physical Review A*, vol. 60, pp. 4831–4845, Dec. 1999.

[145] A. Sanchez, K. Amini, S.-J. Wang, T. Steinle, B. Blanca, J. Danek, A.-T. Le, X. Liu, R. Moshammer, T. Pfeifer, M. Ritcher, J. Ullrich, S. Gräfe, C. D. Lin, and J. Biegert, "Molecular structure retrieval directly from laboratory-frame photoelectron spectra in laser-induced electron diffraction," *Nat Commun*, vol. 12, no. 1520, 2021.

[146] J. Maurer, B. Willenberg, J. Daněk, B. W. Mayer, C. R. Phillips, L. Gallmann, M. Klaiber, K. Z. Hatsagortsyan, C. H. Keitel, and U. Keller, "Probing the ionization wave packet and recollision dynamics with an elliptically polarized strong laser field in the nondipole regime," *Phys. Rev. A*, vol. 97, p. 013404, Jan 2018.

[147] Hartung, A., Eckart, S., Brennecke, S. et al., "Magnetic fields alter strong-field ionization.," *Nature Phys.*, vol. 15, 2019.

[148] B. Willenberg, J. Maurer, U. Keller, J. Daněk, M. Klaiber, N. Teeny, K. Z. Hatsagortsyan, and C. H. Keitel, "Holographic interferences in strong-field ionization beyond the dipole approximation: The influence of the peak and focal-volume-averaged laser intensities," *Phys. Rev. A*, vol. 100, p. 033417, Sep 2019.

[149] S. Chelkowski, A. D. Bandrauk, and P. B. Corkum, "Photon-momentum transfer in multiphoton ionization and in time-resolved holography with photoelectrons," *Phys. Rev. A*, vol. 92, p. 051401, Nov 2015.

[150] T. Keil and D. Bauer vol. 50, p. 194002, sep 2017.

[151] S. Brennecke and M. Lein, "High-order above-threshold ionization beyond the electric dipole approximation: Dependence on the atomic and molecular structure," *Phys. Rev. A*, vol. 98, p. 063414, Dec 2018.

[152] J. Daněk, *Coulomb effects in the dipole and nondipole regimes of strong-field ionization*. PhD thesis, Ruprecht-Karls-Universität, Heidelberg, 2018.

[153] J. Xu, C. Blaga, K. Zhang, Y. Lai, C. Lin, T. A. Miller, P. Agostini, and L. DiMauro, "Diffraction using laser-driven broadband electron wave packets," *Nature Communications*, vol. 5, p. 4635, 2014.

[154] Y. Ito, C. Wang, A.-T. Le, M. Okunishi, D. Ding, C. D. Lin, and K. Ueda, "Extracting conformational structure information of benzene molecules via laser-induced electron diffraction," *Structural Dynamics*, vol. 3, no. 3, p. 034303, 2016.

[155] E. T. Karamatskos, G. Goldsztejn, S. Raabe, P. Stammer, T. Mullins, A. Trabattoni, R. R. Johansen, H. Stapelfeldt, S. Trippel, M. J. J. Vrakking, J. Küpper, and A. Rouzée, "Atomic-resolution imaging of carbonyl sulfide by laser-induced electron diffraction," *The Journal of Chemical Physics*, vol. 150, no. 24, p. 244301, 2019.

[156] R. Renner, "Zur theorie der wechselwirkung zwischen elektronen- und kernbewegung bei dreiatomigen, stabförmigen molekülen.," *Z. Physik*, vol. 92, p. 172–193, 1934.

[157] G. Herzberg, *Molecular Spectra and Molecular Structure. III. Electronic Spectra and Electronic Structure of Polyatomic Molecules*. D. Van Nostrand, Prinston 1966, 1968.

[158] H. Fuest, Y. H. Lai, C. I. Blaga, K. Suzuki, J. Xu, P. Rupp, H. Li, P. Wnuk, P. Agostini, K. Yamazaki, M. Kanno, H. Kono, M. F. Kling, and L. F. DiMauro, "Diffractive imaging of c_{60} structural deformations induced by intense femtosecond midinfrared laser fields," *Phys. Rev. Lett.*, vol. 122, p. 053002, Feb 2019.

[159] N. Suárez, A. Chacón, M. F. Ciappina, B. Wolter, J. Biegert, and M. Lewenstein, "Above-threshold ionization and laser-induced electron diffraction in diatomic molecules," *Phys. Rev. A*, vol. 94, p. 043423, Oct 2016.

[160] J. Viefhaus, F. Scholz, S. Deinert, L. Glaser, M. Ilchen, J. Seltmann, P. Walter, and F. Siewert, "The variable polarization xuv beamline p04 at petra iii: Optics, mechanics and their performance," *Nuclear Instruments and Methods in Physics Research Section A: Accelerators, Spectrometers, Detectors and Associated Equipment*, vol. 710, pp. 151–154, 2013. The 4th international workshop on Metrology for X-ray Optics, Mirror Design, and Fabrication.

[161] G. Hartmann, *Coherence effects of diatomic homonuclear molecules and sequential two-photon processes of noble gases in the photoionization*. PhD thesis, Universität Berlin, 2014.

[162] R. Sun, X. Lai, S. Yu, Y. Wang, S. Xu, W. Quan, and X. Liu, "Tomographic extraction of the internuclear separation based on two-center interference with aligned diatomic molecules," *Phys. Rev. Lett.*, vol. 122, p. 193202, May 2019.

[163] H. J. Wörner, J. B. Bertrand, B. Fabre, J. Higuet, H. Ruf, A. Dubrouil, S. Patchkovskii, M. Spanner, Y. Mairesse, V. Blanchet, E. Mével, E. Constant, P. B. Corkum, and D. M. Villeneuve, "Conical intersection dynamics in no₂ probed by homodyne high-harmonic spectroscopy," *Science*, vol. 334, no. 6053, pp. 208–212, 2011.

[164] S. Beaulieu, A. Ferré, R. Géneaux, R. Canonge, D. Descamps, B. Fabre, N. Fedorov, F. Légaré, S. Petit, T. Ruchon, V. Blanchet, Y. Mairesse, and B. Pons, "Universality of photoelectron circular dichroism in the photoionization of chiral molecules," *New J. Phys.*, vol. 18, p. 102002, oct 2016.

[165] S. Rozen, S. Larroque, N. Dudovich, Y. Mairesse, and B. Pons, "Enhanced chiral-sensitivity of coulomb-focused electrons in strong field ionization," *J. Phys. B: At. Mol. Opt. Phys.*, vol. 54, p. 184002, sep 2021.

[166] M. Okunishi, Y. Ito, V. Sharma, S. Aktar, K. Ueda, R. R. Lucchese, A. I. Dnestryan, O. I. Tolstikhin, S. Inoue, H. Matsui, and T. Morishita, "Rescattering photoelectron spectroscopy of the co_2 molecule: Progress towards experimental discrimination between theoretical target-structure models," *Phys. Rev. A*, vol. 100, p. 053404, Nov 2019.

[167] C. Wu, C. Wu, D. Song, H. Su, Y. Yang, Z. Wu, X. Liu, H. Liu, M. Li, Y. Deng, Y. Liu, L.-Y. Peng, H. Jiang, and Q. Gong, "Nonsequential and sequential fragmentation of ${CO_2}^{3+}$ in intense laser fields," *Phys. Rev. Lett.*, vol. 110, p. 103601, Mar 2013.

[168] E. Wang, X. Shan, Z. Shen, M. Gong, Y. Tang, Y. Pan, K.-C. Lau, and X. Chen, "Pathways for nonsequential and sequential fragmentation of ${CO_2}^{3+}$ investigated by electron collision," *Phys. Rev. A*, vol. 91, p. 052711, May 2015.

[169] Guillemin, R., Decleva, P., Stener, M. et al., "Selecting core-hole localization or delocalization in cs_2 by photofragmentation dynamics.," *Nat Commun*, vol. 6, 2015.

[170] Z. Shen, E. Wang, M. Gong, X. Shan, and X. Chen, "Fragmentation dynamics of carbonyl sulfide in collision with 500 ev electron," *The Journal of Chemical Physics*, vol. 145, no. 23, p. 234303, 2016.